Experimental and numerical characterization of mechanical behavior and wear pattern of vitreous bonding grinding wheels

Tyrone Cristóbal Pazmiño Franco

université de BORDEAUX

THÈSE EN COTUTELLE PRÉSENTÉE POUR OBTENIR LE GRADE DE

DOCTEUR DE

L'UNIVERSITÉ DE BORDEAUX

ET DE L'UNIVERSITE DEL PAIS VASCO

ÉCOLE DOCTORALE SCIENCES PHYSIQUES ET DE L'INGÉNIEUR

ÉCOLE DOCTORALE DU PARTENAIRE INGENIERÍA MECÁNICA

SPÉCIALITÉ MÉCANIQUE

Tyrone Cristóbal PAZMIÑO FRANCO

CARACTÉRISATION EXPÉRIMENTALE ET NUMÉRIQUE DU COMPORTEMENT MÉCANIQUE ET DU PROFIL D'USURE DES MEULES À LIANT VITREUX

EXPERIMENTAL AND NUMERICAL CHARACTERIZATION OF MECHANICAL BEHAVIOR AND WEAR PATTERN OF VITREOUS BONDING GRINDING WHEELS

Sous la direction de : Prof. Dr. Olivier CAHUC
(Co-directeur : Dr. Iñigo POMBO)

Soutenue le 15/12/2023

Membres du jury :

M. Franck GIROT, Professeur, UPV/EHU, Examinateur
M. Raynald LAHEURTE, Professeur, Université Bordeaux, Examinateur
M. Martin CARPOFORO, Professeur, Universidad de Sevilla, Examinateur
Mme. Madalina CALAMAZ, Maîtresse de conférences, ENSAM, Examinatrice
M. Jorge ALVAREZ, Chargé de recherche, IDEKO, Examinateur

Membres invités :
M. José Antonio SANCHEZ, Professeur, UPV/EHU, invité
Mme. Leire GODINO, Docteure, UPV/EHU, invité

Titre : CARACTÉRISATION EXPÉRIMENTALE ET NUMÉRIQUE DU COMPORTEMENT MÉCANIQUE ET DU PROFIL D'USURE DES MEULES À LIANT VITREUX

Résumé :

Le meulage est crucial dans la fabrication, garantissant la précision, la durabilité et la qualité de la surface. La meule, responsable de l'enlèvement de matière de la pièce, joue un rôle essentiel dans ce processus. Les progrès récents améliorent la durée de vie des outils, mais l'usure, en particulier la rupture des liaisons, a un impact sur les performances. Comprendre l'usure volumétrique est essentiel pour optimiser la rectification.

Pour aborder la problématique de la rupture de liaison dans les meules en alumine vitrifiée et considérant l'influence de la résistance du liant lors du contact entre les grains et la pièce, cette recherche vise à caractériser l'évolution de l'usure volumétrique dans des conditions de contact de meulage. L'étude combine des approches expérimentales et numériques pour examiner le phénomène de rupture des liaisons.

Des tests de meulage réels sont effectués pour isoler la rupture de liaison et étudier son apparition à l'aide de paramètres réels. Ce travail met l'accent sur l'importance des forces agissant sur la zone de contact et l'influence de la résistance du liant dans la génération de la rupture du lien. De plus, le test expérimental permet de contrôler les conditions de contact et d'étudier plus en détail le phénomène.

De plus, une analyse numérique est réalisée, utilisant une nouvelle approche de simulation multi-échelle pour suivre l'évolution de la rupture des liaisons. L'approche multi-échelle intègre un modèle micro-échelle DEM (µSM) et la randomisation du modèle micro-échelle (RµSM) de la roue. Le µSM simule le champ de contrainte lors du contact, tandis que le RµSM tient compte de la localisation aléatoire des grains. Cette approche réduit le temps de calcul et détermine le nombre de grains perdus dans un ensemble de conditions de broyage données. Deux hypothèses basées sur les propriétés du liant présent dans chaque grain sont considérées. Il s'agit du premier modèle permettant de prédire l'usure volumétrique des meules.

D'une part, l'hypothèse 1 de l'approche multi-échelle met à jour le comportement mécanique du liant au fur et à mesure de l'usure de la meule. Les résultats

démontrent un bon accord entre les résultats expérimentaux et les résultats de simulation, avec un facteur de forme du grain de 6%. Cela met en évidence l'alignement entre le modèle numérique et le test expérimental. En revanche, l'hypothèse 2 de l'approche multi-échelle introduit un facteur d'endommagement dans le liant pour tenir compte de l'écart en pourcentage de pénétration critique dans chaque grain après chaque rotation de la roue. Les résultats des analyses expérimentales et numériques de l'usure radiale et du taux de meulage présentent un bon accord, le meilleur ajustement correspondant à une valeur de dommage de 0,7 %. Cependant, la recherche ne trouve aucune preuve que les températures élevées affectent le liant. Par conséquent, un modèle thermique est développé pour mettre en évidence l'influence de la température au sein du liant.

Il a été supposé que les températures élevées atteintes au cours du processus pourraient potentiellement affecter la structure du liant. Cependant, les résultats du modèle thermique contredisent cette notion, démontrant que le liant subit des températures plus basses lors du broyage. Ainsi, la nature du processus rend très probable que des situations puissent survenir dans lesquelles le contact entre l'épaisseur des copeaux et le liant affecte les propriétés du liant par transfert de chaleur par conduction.

En conclusion, cette thèse aborde le problème de la rupture de liaison dans les meules en alumine vitrifiée, en considérant l'influence de la résistance du liant lors du contact entre les grains et la pièce. Les recherches impliquent des tests expérimentaux et des simulations numériques pour caractériser l'usure volumétrique. Les résultats contribuent à l'optimisation du processus et mettent en lumière les facteurs affectant la longévité des roues.

Mots clés : Simulation numérique, usure volumétrique, rapport de rectification, meule, liaison vitreuse, comportement mécanique.

Title : EXPERIMENTAL AND NUMERICAL CHARACTERIZATION OF MECHANICAL BEHAVIOR AND WEAR PATTERN OF VITREOUS BONDING GRINDING WHEELS

Abstract :

Grinding is crucial in manufacturing, ensuring precision, durability, and surface quality. The grinding wheel, responsible for material removal from the workpiece, plays a critical role in this process. Recent advancements enhance tool life, but wear, particularly bond fracture, impacts performance. Understanding volumetric wear is essential for optimizing grinding.

To address the issue of bond fracture in vitrified alumina grinding wheels and considering the influence of the strength of the binder during the contact between grains and workpiece, this research aims to characterize the evolution of volumetric wear under grinding contact conditions. The study combines experimental and numerical approaches to examine phenomenon of bond fracture. Real grinding tests are conducted to isolate bond fracture and investigate its occurrence using actual grinding parameters. This work emphasizes the significance of forces acting on the contact area and the influence of the strength of binder in generating bond fracture. Additionally, the experimental test allows to control contact conditions and further investigate the phenomenon.

Furthermore, a numerical analysis of vitrified alumina grinding wheels is carried out, employing a novel multiscale simulation approach to track the evolution of bond fracture. The multiscale model integrates a DEM microscale model (μSM) and randomization of the microscale model (RμSM) of the wheel. The μSM simulates the stress field in the region of the wheel in contact with the workpiece, while RμSM accounts for the actual and random location of the grits. This approach drastically reduces computational time and effectively determines the actual number of grains lost under a set of given grinding conditions. Two hypotheses based on the properties of the binder in each grain are considered in this analysis. This is the first model to predict the volumetric wear of grinding wheels.

On the one hand, hypothesis 1 of the multiscale approach updates the mechanical behavior of the binder as the grinding wheel wears. The results demonstrate a good agreement between the experimental findings and the results obtained from the multiscale simulation, with a shape factor of the grain of 6%. This highlights the strong alignment between the numerical model and experimental test. On the other

hand, hypothesis 2 of the multiscale approach introduces a damage factor in the binder to account for the percentage deviation of critical penetration in each grain after each rotation of the wheel. The results obtained from both experimental and numerical analyses of radial wear and grinding ratio exhibit a favorable agreement, with the best fit corresponding to a damage value of 0.7%. However, the research does not find evidence that high temperatures affect the binder. Consequently, a thermal model is developed to showcase the distribution and influence of the temperature within the binder.

It has been speculated that the elevated temperatures reached during the grinding process may potentially affect the structure of the binder in the alumina grinding wheel. However, the results obtained from the thermal model contradict this notion, demonstrating that the binder experiences lower temperatures during the grinding. Thus, the inherent nature of the grinding process makes it highly likely that situations may arise where the contact between chip thickness and binder potentially affect the properties of the binder through heat transfer by conduction.

In conclusion, this thesis addresses the problem of bond fracture in vitrified alumina grinding wheels, considering the influence of the strength of binder during the contact between grains and workpiece. The research involves real grinding experimental tests and numerical simulations to characterize and understand volumetric wear. The findings contribute to the optimization of the grinding process and shed light on the factors affecting the performance and longevity of grinding wheels.

Keywords : Numerical simulation, volumetric wear, grinding ratio, grinding wheel, vitreous bond, mechanical behavior.

ÉCOLE NATIONALE SUPÉRIEURE D´ARTS ET MÉTIERS (ENSAM)

[Laboratoire d'etude des microstructures et de mécanique des matériaux, UMR 7939, 8 Av. de l'Université, 33400 Talence, France]

Table of Contents

1. INTRODUCTION 1

1.1 Introduction 1

1.2 Objectives and contributions 3

1.3 Content 4

2. REVIEW OF THE STATE OF THE ART 7

2.1 Introduction 7

2.2 Introduction to the grinding process 8

2.2.1 Fundamentals 8

2.2.2 Recent developments in grinding 11

2.3 Grinding with complex profile grinding wheels 16

2.3.1 Characteristics of the profile grinding wheels 16

2.3.2 Vitreous bond wheels 23

2.3.3 Kinematics 25

2.3.4 Contact mechanics 29

2.4 Wear phenomenon of the grinding wheels 33

2.4.1 General description 33

2.4.2 Wear mechanism 34

2.4.3 Wear characteristic 36

2.4.4 Bond fracture 38

2.4.5 Monitoring and analysis of grinding wheel wear. 41

2.5 Mechanical and thermal properties of the grinding wheel 45

2.6 Simulation and modelling of the grinding wheels performance 55

2.6.1 Grinding wheels surface modelling *56*

2.6.2 Grinding forces modelling *60*

2.6.3 Grinding wheels mechanical behavior modelling *61*

2.6.4 Grinding wheels wear modelling *62*

2.7 Preliminary conclusions 63

3. EXPERIMENTAL ANALYSIS OF VOLUMETRIC WEAR OF VITRIFIED ALUMINA GRINDING WHEELS. 67

3.1 Introduction 67

3.2 Equipment 68

3.3 Monitoring devices 70

3.3.1 Power measurement *70*

3.3.2 Force measurement *72*

3.3.3 Volumetric wear measurement *72*

3.3.4 Attritious wear measurement *73*

3.4 Methodology 74

3.4.1 Test condition *74*

3.4.2 Testing Procedure *78*

3.5 Discussion of results 79

3.5.1 Power and specific energy *80*

3.5.2 Grinding forces *81*

3.5.3 Volumetric wear *82*

3.5.4 Profile wear of the grinding wheel *83*

3.5.5 Attritious wear quantification *84*

3.6 Preliminary conclusions 84

4. MULTISCALE SIMULATION OF THE VOLUMETRIC WEAR OF VITRIFIED ALUMINA GRINDING WHEELS 87

4.1 Introduction 87

4.2 Description of the multiscale simulation 88

4.3 DEM microscale simulation model (μSM) 90

4.3.1 Fundamentals of the DEM microscale model (μSM) 90

4.3.2 Modelling wheel structure 92

4.3.3 Boundary conditions (μSM) 97

4.3.4 Model set-up 98

4.3.5 Failure criteria and calibration of the μSM 101

4.3.6 Active grain density in μSM 104

4.3.7 Simulation of the μSM 106

4.4 Randomization of the μSM (RμSM) 107

4.4.1 Develop of the RμSM 107

4.4.2 Active grain density 108

4.4.3 Algorithm for estimating of the volumetric wear. 109

4.5 Multiscale simulations and discussion of results 112

4.5.1 Actual contact length, contact stiffness, and friction coefficient. 112

4.5.2 Variability of critical penetration and number of DE´s removed in different μSM. 113

4.5.3 Statistical treatment of the mechanical strength of bonding bridges in each grain 115

4.5.4 Validation of the system of forces acting on the μSM. 116

4.5.5 Estimation of radial wear and G ratio 120

4.6 Preliminary conclusions 125

5. SIMULATION OF THERMAL LOADING ON VITREOUS BONDING BRIDGES OF VITRIFIED GRIDING WHEEL 129

5.1 Introduction 129

5.2 Basis of the thermal model 130

5.3 Discussion on numerical simulation of temperature fields 134

5.4 Preliminary conclusions 141

6. CONCLUSIONS AND FUTURE WORKS 143

6.1 Conclusions 143

6.2 Future works 148

7. NOMENCLATURE 151

8. REFERENCES 155

List of Figures

Figure 1. Schematic illustration of chip formation by an abrasive grit removing material from the workpiece during the surface grinding process. 9
Figure 2. Grinding application [8]–[10]. 10
Figure 3. Structural composition of the grinding wheel. 11
Figure 4. Schematic diagram of electrochemical grinding [13]. 12
Figure 5. Schematic diagram of MQL system [12]. 13
Figure 6. High-speed measurement for full contact grinding [19]. 14
Figure 7. Simulation of centerless grinding geometric stability [23]. 15
Figure 8. Schematic drawing for grinding helicoidal gear with profile grinding wheel. .. 16
Figure 9. Turbine blade from a Turbo-Union jet engine [28]. 17
Figure 10. International Standard Shapes for Conventional Wheels [3] 20
Figure 11. Sharp Cutting Edges of a CBN Grit seen in SEM. [32] 20
Figure 12. Dressing with rotatory diamond dressers [35]. 21
Figure 13. Profile grinding wheel and gear in grinding setup [7] 23
Figure 14. Vitreous bond between two abrasive grains [42] 24
Figure 15. Grinding wheel combining the effects of depth of cut a_e and the deflection. . 27
Figure 16. The displacement of two consecutive grains during the grinding process. 28
Figure 17. Grinding wheel wear mechanism 34
Figure 18. Bond fracture phenomenon. (a) Electroplated CBN wheel [62], (b) Vitrified alumina grinding wheel [42]. 35
Figure 19. Wear pattern of grinding wheel [65] 36
Figure 20. Wear of the bond of the CBN grinding wheel (a) with conventional glass bond (b) with glass crystalline bond [47]. 39
Figure 21. Fracture of the vitreous bond in the grinding wheel [42]. 40
Figure 22. Set up of experiment test for the measurement of the grinding wheel (a) Monitoring of the grinding wheel wear [77] (b) Machine vision measurement of profile grinding wheel [81] 43
Figure 23. Wear patterns on the surface of profile grinding wheel [5]. 44
Figure 24. Stress vs strain in brittle material 45

Figure 25. Effect of the variation of the volume of the three components on the structure grinding wheel [91]. 48
Figure 26. Equilateral triangle of the composition of the grinding wheels [92]. 48
Figure 27. Schematic and experiment setup for compressive, Brazilian and three-point bending test [96]. 50
Figure 28. The bending strength curve of vitrified bond CBN composites with varying sintering temperatures [104] 52
Figure 29. Three-points bending test [113] 53
Figure 30. Force vs displacement during Brazilian experimental test [115]. 54
Figure 31. Models and their applications areas for simulation [121]. 55
Figure 32. Normal distribution of the grain size [122] 57
Figure 33. Schematic of active contact grains, active cutting grains and the penetration into the workpiece [130] 59
Figure 34. Configuration of the grinding simulation [96] 61
Figure 35. Schematic representation of the grinding wheel model [143] 62
Figure 36. Vitrified alumina grinding wheel 100% monocrystalline 69
Figure 37. Surface grinding machine Blohm orbit 36 69
Figure 38. Geometry of the workpiece. 70
Figure 39. Power measurement during the grinding operation 71
Figure 40. Amplitude vs. frequency analysis of the power signal for determining the cutoff frequency 71
Figure 41. Force measurement during the grinding operation. 72
Figure 42. Volumetric wear measurement in the center of the grinding wheel 73
Figure 43. Topographic profile wear measurement in the graphite piece. 73
Figure 44. Attritious wear measurement with the optical microscope Dino-Lite with the light direction oriented perpendicular to the wheel surface. 74
Figure 45. Working zone positioned in the middle of the grinding wheel. 75
Figure 46. Setting up of the experimental system 76
Figure 47. Attritious wear quantification processing. (a) raw 2D images, (b) flat areas detection 79
Figure 48. Specific power (P') and specific grinding energy (e_c) vs. specific volume of part material removed (V'_w) 80
Figure 49. Specific normal (F'_n) and tangential (F'_t) grinding force vs. specific volume of part material removed (V'_w) 81

Figure 50. Loss of geometry as measured on the graphite workpiece at the center of the wheel (V'_w=900.12 mm^3/mm) 82
Figure 51. Specific volumetric wear V'_s versus specific metal removed V'_w. 82
Figure 52. Evolution of the topographic profile wear of the grinding wheel after each grinding test block observed in the graphite replica. 83
Figure 53. Average percentage of attritious wear in each experimental test block. 84
Figure 54. Representation of DEs and beam: (a) DEs and beams representing abrasive grains and vitreous bonds, respectively; (b) System of forces and torques acting between two DEs. 92
Figure 55. Results for the wheel (MA46EF12V) used in the experimental test. 93
Figure 56. FEM model of wheel deformation under the effect of grinding and centrifugal forces. 95
Figure 57. Size of the grinding wheel section 95
Figure 58. Discretization of μSM. 97
Figure 59. Boundary conditions of the μSM. 97
Figure 60. Schematic diagram for calculation of δ_{av}. 99
Figure 61. Contact detection on contact length segment A - B between DEs and workpiece 100
Figure 62. Stress vs strain of three samples from 3 bending test. 101
Figure 63. DE removal from the μSM following Rankine criterium. 102
Figure 64. Results of the initial tensile test showing the calibration process for obtaining a stable value of macro Poisson ratio (ν_s). 103
Figure 65. Results of the second tensile test showing the calibration process for obtaining a stable value of macro Young modulus (E_s) and reach the macro failure stress (σ_f). 103
Figure 66. Surface grain density in *μSM*. Effect of element pile-up from numerical sintering. 105
Figure 67. Flow chart showing the algorithm of the μSM. 106
Figure 68. Macroscale geometry (RμSM) sintered in the complete domain of the grinding wheel. 107
Figure 69. Surface grain density in *μSM* and *RμSM*. Boundary-induced lower density in the *RμSM* 108
Figure 70. Flow chart showing the algorithm of the RμSM in Hypothesis 1. 110

Figure 71. Flow chart showing the algorithm of the RμSM in Hypothesis 2. 111
Figure 72. Critical penetration vs DE´s removed..... 114
Figure 73. Multivariate Random Normal Function from critical penetration and DE´s removed..... 116
Figure 74. Measurement of specific forces and grain losses according to workpiece position in μSM. 117
Figure 75. Voids left on the surface by the volumetric wear seen in the cut plane B-B' of μSM. (a) Workpiece position 0.2 mm (b) Workpiece position 0.25 mm..... 118
Figure 76. Comparison between extracted peaks of the specific normal force from the simulation..... 118
Figure 77. Beam Stress Analysis in the Cut Plane B-B' of μSM at different workpiece positions. (a) Workpiece position 0.36 mm. (b) Workpiece position 1.05 mm. 119
Figure 78. Comparison of wear between multiscale simulations and experiments. 121
Figure 79. Experimentally measured and simulated radial wear for a shape factor value of S_f=6%. 122
Figure 80. Evolution of the graphite replica profile (XP, experimental) and simulated RμSM profile at three different values of V'_w..... 123
Figure 81. Comparison of wear between multiscale simulations and experiments. 124
Figure 82. Experimentally measured and simulated radial wear for a value of damage D=0.7%. 125
Figure 83. Ideal representation of a portion of the grinding wheel..... 132
Figure 84. Instantaneous highest temperature field in the model (alumina grains). 135
Figure 85. Instantaneous highest temperature field in the model (CBN grains). 136
Figure 86. SEM micrograph (x250): Presence of part material (chip) in contact with abrasive grains and bonding material..... 138
Figure 87. Temperature field in the bonding bridge during the contact time with chip length 0.108 mm. Upper panel: alumina grits; Lower panel: CBN grits. 139
Figure 88. Temperature field in the bonding bridge during the contact time with chip length 0.108 mm. Upper panel: alumina grits; Lower panel: CBN grits. 140

List of Tables

Table 1. Test conditions 77
Table 2. Physic characteristics of the vitrified alumina grinding wheel 93
Table 3. Dimensional data of μSM 96
Table 4. Structural comparison of μSM and the actual grinding wheel 96
Table 5. Macro and micro properties of the grinding wheel model 104
Table 6. Structural comparison of μSM and the actual grinding wheel 105
Table 7. Structural comparison between RμSM and the actual grinding wheel 109
Table 8. Actual contact length, contact stiffness and friction coefficient 113
Table 9. Thermal Properties of Alumina Grits, CBN Grits, and Vitrified Bond in Simulations. 134

Chapter 1

Introduction

1.1 Introduction

Grinding is an ancient process that still plays a vital role in modern industry. It is an abrasive machining technique employed in the final stages of manufacturing high-precision components with excellent surface finishes. Grinding represents a value-added operation in mechanical component production, as it enables the attainment of dimensional tolerances and surface finishes unachievable by other manufacturing processes. This operation contributes to the fatigue life of the component, making it crucial in high-tech sectors such as aerospace, automotive, optics, robotics, and micro-manufacturing. The grinding process uses a high-speed rotating abrasive wheel to remove material, consisting of abrasive grains, bonding material, and pores, with shapes tailored to specific grinding requirements. These abrasive tools possess non-defined cutting edges, allowing thousands of abrasive particles with higher hardness than the workpiece material to collectively remove material. By combining cutting edges with appropriate grinding conditions, high-quality workpieces made from hard materials can be produced.

The bonding material are known as those that holds the grains together. The four types of the bonding systems are resinous, metallic, electro-plated and vitreous bond. Common bonding materials for conventional abrasive wheels include resinoid (including reinforced), vitrified, rubber (including reinforced), silicate, oxiclaurate, and shellac. Vitrified bonding is the most prevalent, accounting for almost 50% of all manufactured abrasive wheels. Vitrified bonds consist of glass formed by consolidating ceramic components such as clay, feldspar, and borax at high temperatures. Vitrified bonds exhibit stability at high temperatures, fragility, rigidity, and the ability to withstand high levels of porosity within the abrasive wheel structure. Among their other important characteristics, vitrified grinding wheels are dressing easier and simultaneously exhibit high wear resistance. Furthermore, the controllable elements in vitrified grinding wheels are the porosity and structure, as they enable the adjustment of the grinding wheel's strength. They also play a vital role in defining the topography of the abrasive wheel, allowing for a diverse range of metal removal rates and surface finishes to be achieved.

One crucial aspect of the grinding process is the contact zone, where material removal and heat generation occur. This contact involves high pressures (1-2 GPa) and high relative velocities (>30 m/s) between the workpiece and the abrasive wheel. During this interaction, the abrasive wheel undergoes wear, leading to progressive degradation and a loss of cutting capability. This wear negatively affects the final quality of the parts, causing the deterioration of dimensional tolerances and the modification of process parameters, which has repercussions on the viability of the operation. The wear also results in a loss of dimensional tolerances and surface finish, ultimately affecting the viability of the grinding process and potentially compromising the fatigue behavior of the components. The grinding wheels can experience three main wear mechanisms: attritious wear, grain fracture, and bond fracture.

Among the various wear mechanisms, bond fracture occurrence has a significant impact on performance degradation. This is because when the grinding wheel experiences extensive wear, it diminishes its ability to accurately grind materials. Furthermore, other types of wear can also coexist. However, the generation of bond fractures can solely happen, depending on grinding parameters and wheel conditioning.

This research work addresses the issue of volumetric wear in grinding wheels from a scientific point of view, applying fundamental studies to address the practical problem of grinding wheel life in industrial applications. The study primarily focuses on characterizing the occurrence of bond fracture under grinding contact conditions. To achieve this, carefully designed experimental tests are conducted to analyze the influence of the strength of binder on volumetric wear. To mitigate the randomness of the grinding process, the experimental tests are meticulously designed to control wear of the grinding wheel and replicate the real volumetric wear. To quantify and to gain a comprehensive understanding of volumetric wear throughout the entire grinding process, rather than solely comparing the initial and final states of the grinding wheel, a multiscale simulation approach using the DEM is developed. Both the experimental tests and the numerical model serve as valuable tools for grinding wheel manufacturers, enabling them to characterize the behavior of the vitrified bond under specific grinding conditions. Additionally, a thermal model of the grinding wheel is developed to assess the effect of temperature within the vitrified bond.

1.2 Objectives and contributions

The objectives of this thesis can be summarized as follows:

- To study the nature of volumetric wear, predict the value of the grinding ratio G and analyze the influence of the strength of binder during the contact between abrasive grains and the workpiece. The generation of bond fracture is influenced by the strength of binder, which can vary depending on the location of abrasive grains. This analysis not only considers the number of abrasive grains removed but also examines the critical values of grain penetration during the contact.
- To determine the influence of the bond fracture occurrence in vitrified alumina grinding wheels during real grinding operations. By isolating bond fracture from other types of wear, a comprehensive characterization of the evolution of volumetric wear can be conducted, considering the grinding parameters and the hardness of the grinding wheel.

- To perform experimental tests on a surface grinding machine. The main characteristic of these tests is their ability to reproduce the volumetric wear that occurs during the

contact between abrasive grains and the workpiece in the grinding wheel. Furthermore, the topographic profile of the grinding wheel is reproduced, exhaustively controlled, and quantified during the wear process.

- To precisely predict the radial wear and real volumetric wear experienced of a vitrified alumina grinding wheel. To achieve this, a methodology is established to measure surface topography wear using a graphite piece. This methodology allows for accurate assessment of the radial wear, providing valuable insights into the wear patterns and changes in the grinding wheel's topography.
- To propose a multiscale simulation approach for analyzing the influence of bond fracture generation on the wear during the contact between alumina and steel under grinding conditions. On the one hand, a discrete element wear microscale model (μSM) is developed to accurately replicate the impact of force reactions in the vitrified bond during the contact. This model aims to capture the intricate dynamics involved in the grinding process. On the other hand, randominization of μSM (RμSM) is developed in order to take into account the actual and random positions of the alumina grits. The objective of this macrogeometry approach is to precisely quantify the exact number of grains that are eliminated during the wear process, while concurrently reducing computational costs. Furthermore, it is essential to validate the proposed numerical model experimentally.
- To determine the impact of temperature on the vitrified bond under real grinding conditions. The main focus is to analyze the influence of high temperatures reached within the vitrified bond during grinding operations. To achieve this, a thermal model is developed.
- To create a practical and beneficial tool for the industrial design of grinding wheels that are specifically suited for particular applications. This tool will allow for the thorough characterization of the volumetric wear experienced by vitrified alumina grinding wheels even before the manufacturing process of the required grinding wheel begins.

1.3 Content

The thesis consists of six chapters, with the first chapter serving as the introduction to the work. In this chapter, the purpose and scope of the thesis are established.

The second chapter is dedicated to a comprehensive literature review on the current state of the art in grinding process. Specifically, it focuses on the various aspects of grinding wheel wear that have been crucial in shaping the direction of the present research work. The types of wear exhibited by grinding wheels and abrasive grains are analyzed, with particular emphasis on volumetric wear. The review encompasses the most significant works that form the foundation for the development of the numerical multiscale simulation and thermal model of the grinding wheel. Notably, considerable attention is given to the study of vitrified bond. In order to gain a deeper understanding of the grinding process, in this chapter also delves into the analysis of grinding models, with a specific focus on wear models. By examining these models, the aim is to enhance comprehension of the grinding process itself.

The third chapter focuses on the methodology follow to develop the experimental grinding tests, with the primary objective of characterizing the occurrence of bond fracture in vitrified alumina grinding wheels. The chapter specifically examines the evolution of bond fracture during real grinding processes. The obtained results serve as crucial inputs for the numerical model. Furthermore, the grinding wheel surface is thoroughly analyzed to verify that the bond fracture phenomenon is indeed responsible for the interactions that occur between abrasive grains and the workpiece.

The fourth chapter introduces an innovative multiscale approach that combines the mechanical behavior of vitrified bonds with the stochastic characteristics of grain location. The newly developed multiscale approach incorporates a microscale Discrete Element Method (DEM) model, referred to as μSM, and incorporates randomization of the μSM (RμSM) within the grinding wheel. The μSM simulates the stress distribution within the wheel's contact region with the workpiece, while the RμSM takes into account the actual and random positions of the alumina grits. This approach significantly reduces computational time and accurately determines the actual number of grains lost under specific grinding conditions. The model effectively predicts the detachment of entire clusters of abrasive grains from the bonds, showing a high level of agreement with experimental observations for two hypotheses. On the one hand, the first hypotheses consider the updating the mechanical behavior of the binder as the grinding wheel wears.

On the other hand, the second hypotheses consider the cumulative damage produced in the binder.

In the fifth chapter of the thesis, a thermal model of the vitrified alumina grinding wheel is developed with the objective of determining if the properties of the vitrified bond are influenced by temperature. The model aims to establish the zones within the bond that are affected by changes in temperature during the grinding process.

The sixth and final chapter of the thesis serves as a compilation of the primary contributions and conclusions derived from the research conducted throughout the thesis. It summarizes the key findings and insights obtained during the study. Additionally, this chapter outlines future research directions that can be pursued in the analysis and characterization of wear in grinding wheels. By proposing future avenues of investigation, the chapter aims to inspire further advancements in the field and build upon the knowledge gained through the thesis.

Chapter 2

Review of the state of the art

2.1 Introduction

The initial phase of this research focuses on exploring the fundamental aspects of the grinding process along with the latest technological advancements in the field. Among the various grinding processes, profile grinding stands out as a widely employed technique in the high-value parts industry. However, achieving precise control in profile grinding is challenging due to the inherent variability of the process parameters, which are influenced by numerous factors, including wear. Wear plays a fundamental role in the profile grinding process as it directly impacts the quality, cutting and overall productivity. Of the various types of wear, bond fracture specifically affects volumetric wear, leading to the degradation of the grinding wheel's geometry and, consequently, compromising the quality of the finished parts.

A comprehensive understanding of the mechanical properties of the grinding wheel is carried out. This analysis will conduct a thorough mechanical characterization of the grinding wheel, taking into account its composite structure. Furthermore, it will encompass

an assessment of the wheel's key mechanical and thermal properties, including hardness, strength, fracture toughness and thermal conductivity.

Finally, the simulation and modeling techniques of the grinding processes are presented. These tools predict and optimize grinding wheel performance by simulating the process and analyzing influential factors, including abrasive particles, bond material, wheel geometry, structure, thermal damage, surface topography, and grinding parameters.

This reviewed introduction provides a clearer and more comprehensive overview of the research topic, emphasizing the importance of volumetric wear in profile grinding. In addition, to ensure the proper execution of an experimental test and the accurate creation of a grinding wheel model, it is essential to control the boundary and contact conditions. Additionally, these controlled conditions enable the measurement of important parameters such as radial wear and the G ratio of the grinding wheel.

2.2 Introduction to the grinding process

2.2.1 Fundamentals

The grinding process is key technology to produce high added-value parts [1]. It constitutes 20-25% of the total cost in machining operations [2]. The grinding belongs to the group precision machining with process such as lapping and honing. The important characteristic is the high machining accuracy and good surface finish in hard or fragile materials. Nowadays, the typical level of Ra achieved in grinding operations ranges from about 0.15 to 1.5 μm, and the dimensional tolerances produced are usually 10 to 50 times larger than Ra [2]. This accuracy cannot be obtained with other manufacturing processes [3]. In addition, the grinding process is generally the last stage in the production chain [2], so a small mistake in the process could cause great economic losses. This implies, that latest technology machines with high accuracy are required. With the above mentioned, the importance of grinding in high-technology manufacturing sectors is recognized.

One of the most relevant aspects for a successful grinding process is the grinding wheel (Figure 1). It is composed by a series of compacted hard grains with irregular shapes embedded in a bond. The function of the bond is to hold the abrasive grains in place, and

this is achieved when the material is strong or if there is a sufficiently large cross-sectional area. The bond possesses the capability to endure elevated temperatures, significant forces, and grinding forces without undergoing disintegration. The varied combination of these components allows the wheel to be adaptable to different applications. The grains are harder than the workpiece material. Microscopically, when a grain is shearing material, the grain could be assimilated to a cutting tool with a negative the rake angle, around -60° to -70° [4], as shown in Figure 1.

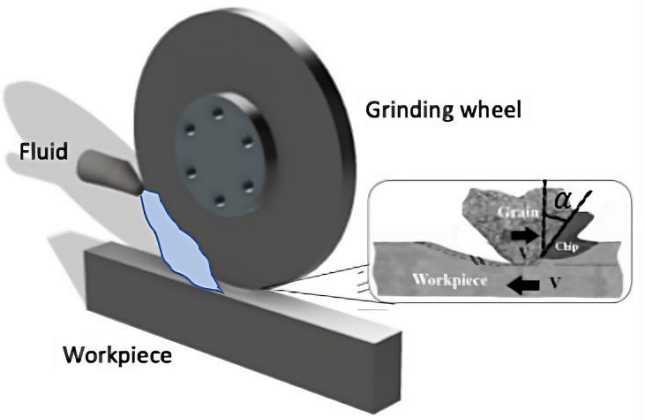

Figure 1. Schematic illustration of chip formation by an abrasive grit removing material from the workpiece during the surface grinding process.

Typical applications of grinding process can be found in many industrial sectors such as aeronautics, automotive industry or biomedical industry. In Figure 2 typical parts of aeronautic industry can be found (turbine blade roots, nozzle guide vane (NGV) or landing gears). In this case the parts are made of nickel alloy and very accurate tolerances are required (dimensional tolerances ±0.15 mm and Ra < 0.5 μm) [5]. In automotive industry, typical materials use to be high alloy steels including high amounts of Cr, Ni, Mn and Mo. The low machinability of the ground parts together with the tight dimensional tolerances (±0.2 mm and Ra < 0.7 μm) [6], makes very difficult a successful grinding process. The gears in machine-tool or marine industry are usually made of Cr and Ni material and reach Sa < 0.8 μm [7]. The increasing demand for precise dimensions and superior surface finish is leading to the use of advanced grinding techniques for these materials.

Figure 2. Grinding application [8]–[10].

The most used abrasive materials in abrasive grinding wheels are alumina Al_2O_3 and silicon carbide SiC. Figure 3 shows the structural composition for a vitrified alumina grinding wheel. These abrasive grains can be seen on the periphery of the grinding wheel as microphylls. The properties and performance of the vitrified alumina grinding wheel depend on the type, size and quantity of the grits, the hardness and the structure of the bonding. The manufactures of the grinding wheel identify the vitrified alumina grinding wheel with limited information keeping in secret the know-how, components and additives. However, the most demanding tasks, superabrasives such as CBN or diamond are often preferred. On the one hand, for the case from CBN grinding wheel, the material such as hardened bearing steel, silicon nitride ceramics and nickel-based superalloys are ground. On the other hand, for the case from diamond grinding wheel, the material of high hardness such as polycrystalline cubic boron nitride (PcBN), the polycrystalline diamond and bioceramic material are ground. These advanced abrasive materials have the unique ability to maintain their sharpness and cutting edge over a longer period of time compared to conventional abrasive materials. It offers exceptional efficiency and cutting capacity for the applications mentioned, making it a highly suitable choice [11]. In spite of this fact, the high cost of this type of wheels, the difficulties to conditioning them and necessity of very rigid and high-power machines to carry out the grinding process in a correct way, fragility and complicated dressing process, together with the recent advances in conventional abrasives, are making are making the vitrified alumina grinding wheels make it a preferred choice for certain situations.

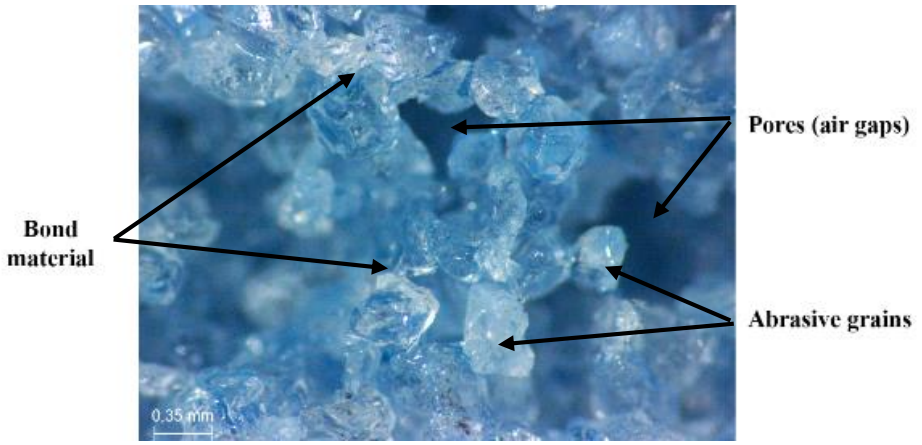

Figure 3. Structural composition of the grinding wheel.

In recent times, grinding parts with complex profiles has emerged as a key application in industries such as aerospace, transportation, and energy. In this context, the use of alumina wheels for profiling and grinding has become increasingly popular due to their ease of use, as well as the latest advances in abrasive materials and their cost. Therefore, the use of these wheels is highly suitable for this type of application.

2.2.2 Recent developments in grinding

All Industrial sectors are undergoing rapid transformations that require advancements in production technology to enhance performance and productivity. In response to these evolving demands, ongoing research efforts are dedicated to this field. Consequently, cutting-edge machines incorporating the latest technologies have been developed to machine intricate geometric components with unparalleled precision and improved quality.

One such technology making significant advance is ultrasonic-assisted grinding (UAG), which facilitates the removal of substantial material volumes using reduced grinding force and generating lower levels of heat [12]. UAG has proven highly effective in achieving superior surface quality and extending the lifespan of grinding wheels. Another notable advancement is electrochemical grinding (ECG), a technique that simultaneously employs electrochemical reactions and abrasive grinding to efficiently eliminate large amounts of material. ECG offers the advantage of low induced stress and further enhances the longevity of grinding wheels [13]. Figure 4 provides a schematic diagram illustrating the principles of electromechanical grinding.

Moreover, modern machines can be tailored to meet specific requirements imposed by diverse components. For instance, external machining may employ a large corundum grinding wheel, while groove machining can use a smaller CBN grinding wheel, each with separate dressing systems. By incorporating these updates, machines can successfully execute cylindrical grinding operations on crankshafts and camshafts, resulting in increased productivity [14].

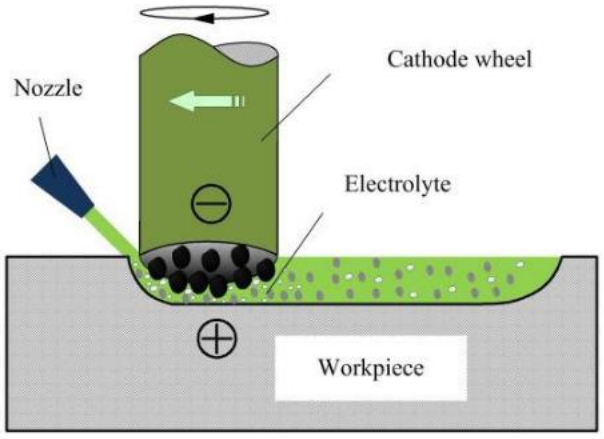

Figure 4. Schematic diagram of electrochemical grinding [13].

In today's competitive market, numerous industrial sectors are actively striving to adopt sustainable practices and establish a strong market presence. However, the grinding process, which is widely employed, poses significant environmental challenges due to the utilization of grinding fluids and the resultant tool wear. To address these concerns, cutting-edge machines equipped with advanced auxiliary devices have been developed to minimize the environmental impact.

One of the recent auxiliary technologies making significant strides in this direction is minimum quantity lubrication (MQL), also known as dry machining. This technique involves the application of a small amount of lubricant in the form of micro-droplets mixed with air directly at the grinding contact area. By adopting MQL, surface quality is improved, coolant usage is minimized, and tool wear is reduced [15]. The components of the MQL system are depicted in Figure 2.4, showcasing its functionality and effectiveness.

Another notable auxiliary technology that has emerged is cryogenic grinding, which utilizes an inert gas, such as nitrogen, as a cooling medium. The application of cryogenic

grinding aims to minimize thermal stress on the workpiece, thereby improving surface quality, reducing tool wear, and minimizing grinding forces [16].

However, it is important to note that in the case of the latter auxiliary technology, the researcher has observed some detrimental effects on the tools. Further investigation and development are required to mitigate these issues and fully harness the potential benefits of cryogenic grinding.

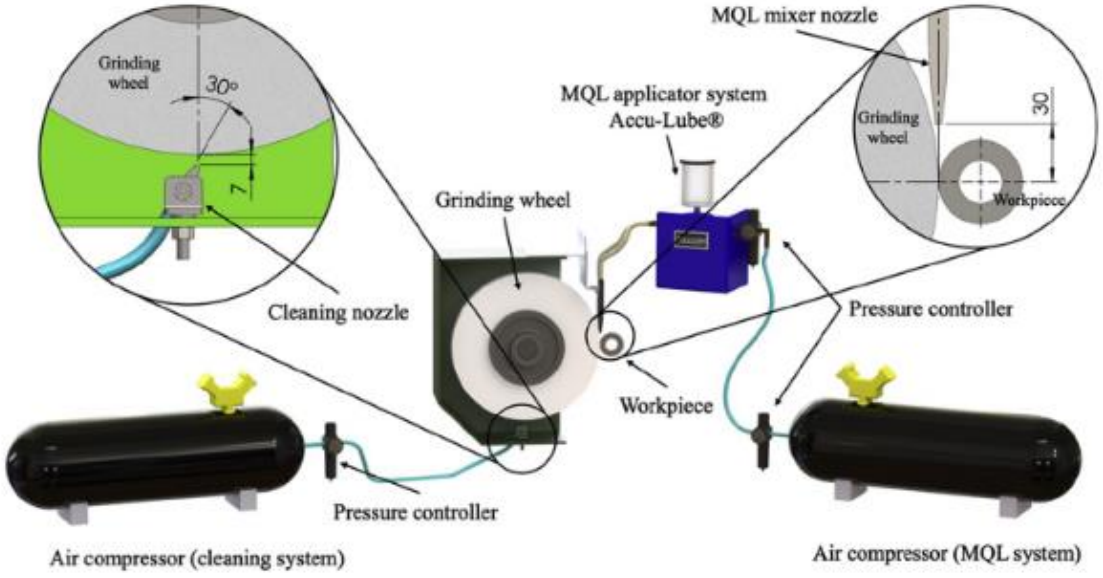

Figure 5. Schematic diagram of MQL system [12].

Conditioning technology holds significant importance in the realm of grinding as it directly influences material removal rate, forces, and surface quality, all of which are vital in manufacturing outcomes. The best machine manufacturers are those equipped with top-notch conditioning systems, driving research towards optimizing this technology. Among these advancements is thermomechanical dressing, which conditions coarse-grained diamond grinding wheels through a chemical reaction involving heat, oxygen, and austenitic steel calottes as catalysts. Coarse-grained diamond allows for excellent surface quality and high precision [17]. Another notable technology is electrolytic dressing in process (ELID), where electrolysis occurs in the grinding wheel through the supply of grinding fluid and an electric current. This method employs diamond abrasives to achieve superior surface quality, particularly on ultra-hard materials. Additionally, wire electric discharge dressing (WEDD) has gained attention after intensive research, offering conditioning of metal-bonded wheels with continuous current supply. WEDD brings

advantages such as improved dressability, low power consumption, minimal grinding wheel wear, and increased grit protrusion. However, it is limited to grit sizes up to 150µm [18]. These advancements reflect the ongoing pursuit of excellence in grinding, aiming to optimize conditioning processes for improved manufacturing outcomes, efficiency, and precision.

High-precision gears have emerged as a critical component in ensuring optimal performance and reliability in transmissions for automobiles, aircraft, and industrial machinery. Modern gears are expected to possess characteristics such as lightweight design, reduced noise emissions, high power density, and enhanced energy efficiency. To meet these demands, a continuous generating gear grinding process has become the preferred method for achieving the hard finishing of high-precision gears. This process employs a vitrified bonded threaded grinding wheel, enabling simultaneous machining of the edges and flutes of the workpiece in a continuous operation, significantly reducing processing time and improving efficiency [13]. Temperature control systems are integrated into the machines to ensure precise and repeatable results, promoting thermal stability during grinding operations. Furthermore, state-of-the-art machines feature advanced electromechanical drive systems and intelligent software, enabling high-speed measurement, as depicted in Figure 6. These measurements assess the quality and distortion of the surface prior to grinding, eliminating the need for non-contact grinding passes and ensuring the entire surface is ground effectively [19].

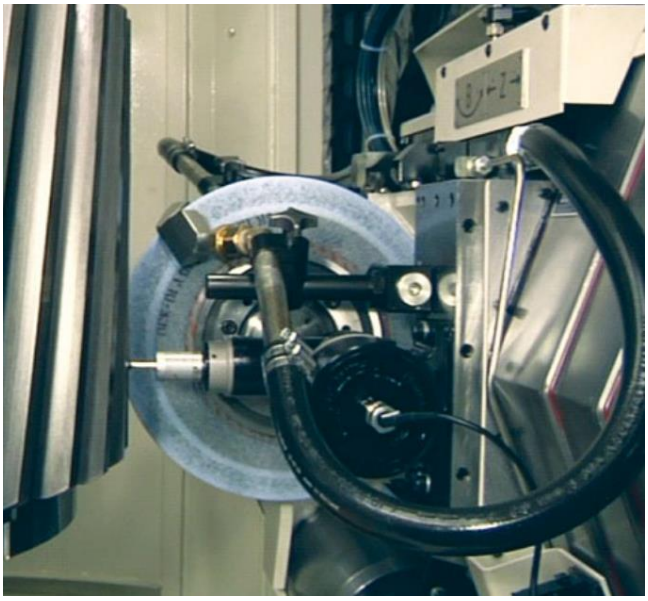

Figure 6. High-speed measurement for full contact grinding [19].

In modern manufacturing, the using of simulation tools has become indispensable for machining operations. These tools offer the capability to predict the outcomes of grinding processes accurately. One such simulation tool is the centerless grinding setup, which employs an algorithm to eliminate geometric instabilities and generate stable maps. This tool visualizes both stable and non-stable geometric configurations, providing information into the evolution of profile errors during the grinding process, as depicted in Figure 7 [20]. Another notable simulation tool is the intelligent grinding assistant (IGA), a software system that records machining information and uses an algorithm to select pertinent data for operators, aiding decision-making and process optimization [21]. Additionally, the finite element method (FEM) is employed as a simulation tool in the grinding process. FEM enables the design of grinding wheel models, predicting grinding forces and workpiece surface topography, yielding results consistent with experimental tests [22]. These simulation tools empower manufacturers to optimize grinding operations and enhance productivity.

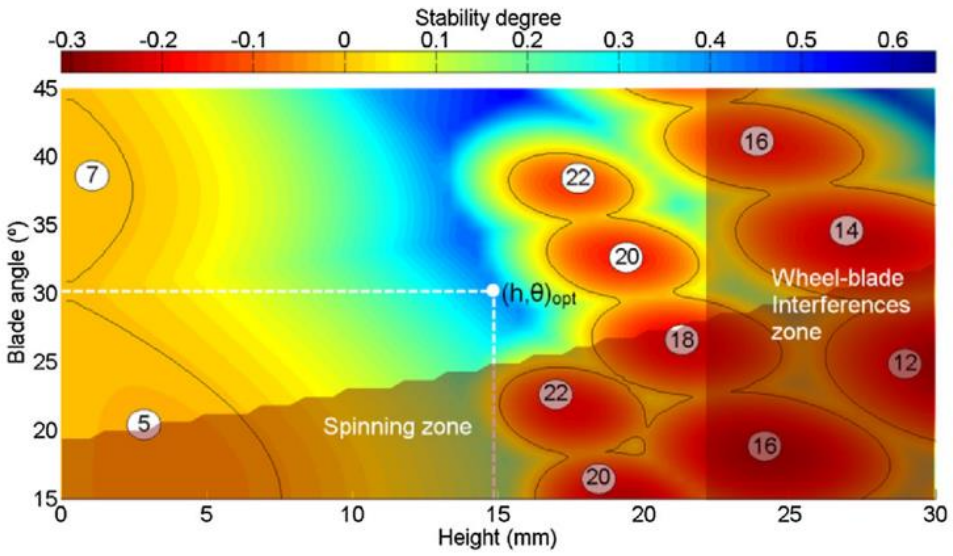

Figure 7. Simulation of centerless grinding geometric stability [23].

2.3 Grinding with complex profile grinding wheels

2.3.1 Characteristics of the profile grinding wheels

The precision profile grinding is a process used to grind the surface of a material to a specific shape. The grinding wheel is shaped to match the desired profile of the finished product [24]. Figure 8 shows a profile grinding wheel grinding a helicoidal gear. The shape of the grinding wheel allows to grind the contour surfaces of the gear teeth and to produce low tolerances with a good surface finished. As can be observed from the illustration, the radius of a profile grinding wheel changes along its width.

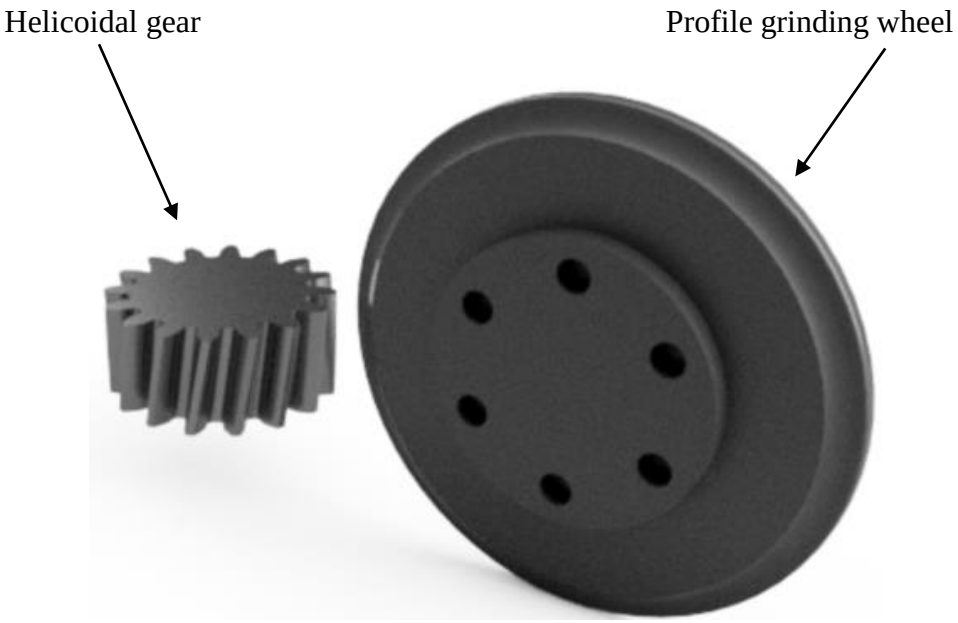

Figure 8. Schematic drawing for grinding helicoidal gear with profile grinding wheel.

The principal characteristics of the profile grinding process are: high precision, complex shape and fine surface finishes. The profile grinding is capable of producing very precise shapes and profiles with tight tolerances. Also, as it is mentioned above, the process is well-suited for producing complex, contoured shapes that would be difficult or impossible to produce with other manufacturing methods. Finally, the process often involves making multiple passes over the workpiece, each time removing a small amount of material and refining the shape and finish. It can produce very fine surface finishes, with roughness values as low as a few micrometers. For example, Ra of the profile surface of turbine blade root ground reaches values of 0.6 μm [25]. All these factors make profile grinding a highly

valued technique in the manufacturing industry, as it offers advantages that are not possible with traditional grinding methods.

Due to its high precision and ability to produce complex and fine finishes, profile grinding has become a technique in great demand in various industries, resulting in a wide range of applications. The profile grinding wheel are often used to create precision in railways or guide, root of a turbine blade, the production of machine parts including bearings, gears, cams, spindles and in the manufacture of tools and cutting edges [26]. One example is in the gears, the tooth gap is ground. These spaces are impossible to reach with conventional profile wheels. When grinding gears, the profile grinding wheel is utilized to grind the teeth to a specific profile, including spur gears, helical gears, bevel gears, and worm gears. For cams, the profile wheel is used to grind the camshaft's cam profile, which is frequently required in the production of high-performance engines and machinery. When grinding tools, such as drill bits or milling cutters, the profile grinding wheel is used to shape the tool's contour. Another example is in the blade roots of gas turbine compressor. The blades are connected to the central axis by the structure that has the root. As seen in Figure 9, the root has a trapezoidal shape with its valleys and ridges on the lateral walls. In one article Denkena et al [27] reduce drag in turbulent flow and improve the efficient of the turbine by grinding microgrooves, known as riblets, onto the surfaces of compressor blades with help of the profile grinding wheels. Therefore, the versatility and suitability of the profile grinding wheel make it a popular choice in many industries, enabling the production of precise and complex shapes for a wide range of applications.

Figure 9. Turbine blade from a Turbo-Union jet engine [28].

Maintaining tight tolerances is important in precision grinding with profile grinding wheels. Typical tolerances for grinding gears using a profile grinding wheel are typically AGMA class 14 or higher [29] to ensure adequate dimensional accuracy. In addition, tolerances for surface roughness can be 0.4 micrometers or less, allowing for smooth and efficient power transmission. For grinding cams with a profile grinding wheel, tolerances can vary depending on the application and specifications provided [2]. Typically, a maximum variation of around 0.0025mm in cam height and shape is allowed, and the tolerance for surface roughness can be 0.2 micrometers or less, ensuring smooth and accurate operation. In the case of grinding cutting tools with a profile grinding wheel, tolerances can also vary depending on the application and customer specifications. Typically, a maximum variation of approximately 0.0025mm in cutting geometry and dimensional accuracy is allowed. In addition, the tolerance for surface roughness can be 0.4 micrometers or less, ensuring reliable performance and a long tool life [29].

Grinding strategies are necessary in various fields such as manufacturing, engineering, and machining. The primary purpose of grinding strategies is to shape and finish the surfaces of different materials to achieve the desired specifications, such as size, shape, and surface roughness. Profile grinding strategies refer to the techniques and methods used to grind complex profiles on workpieces using a profile grinding wheel. One of the techniques is the selection of profile grinding wheel geometry. Depending on the application, the specific design of the profile grinding wheels have different shapes and sizes. Standard International ANSI B74.2 “Specifications for shapes and sizes of grinding wheels and for shapes, sizes and identification of mounted wheels” [30] shows a variety of shapes and sizes of grinding wheels. This specific information is marked on the profile grinding wheel. The complexity of the shapes, the size of the profile and the abrasive material used, are factors that determine the profile grinding wheel design.

Based on the diversity of shapes and sizes outlined in the standard specifications, profile grinding wheels are designed to meet specific grinding needs. There are several types of profile grinding wheels, each designed to work with specific materials and grinding equipment as shown in Figure 10. Some of the most common types of profile grinding wheels include [31]:

- Straight wheels - the most widely used type of profile grinding wheel and are suitable for a variety of grinding operations such as surface grinding, centerless grinding, and cylindrical grinding. The size of these wheels can vary significantly, with the diameter and width of the face depending on the size and power of the grinding machine being used. These wheels are designed with a flat surface and straight edges, which allows for efficient and precise grinding. The versatility and availability of straight wheels make them a popular choice for many grinding applications. They belong to group 1 of the standard.

- Cone wheels – A small abrasive wheel that is bonded and shaped like a cone, cylinder or bullet, and is used with a portable grinder. This type of wheel is mounted on a pin or mandrel for easy use. They belong to type 16, 17, 17R, 18, and 18R cones.

- Cup wheels are specifically designed to be used in horizontal spindle surface grinders. These wheels are tilted at an angle θ from the vertical [3]. They are widely used in precision optics due to their ability to produce exceptionally smooth surfaces. Cup wheels are frequently utilized for re-sharpening and finishing purposes in various applications, depending on the size of the abrasive used.

- Dish wheels refer to shallow cup-style wheels that are typically attached to a vertical spindle grinder. Due to their narrow design, they can easily fit into tight crevices that a cup wheel may not be able to reach. These wheels are commonly used for applications similar to those of cup wheels.

- Tapered wheels belong to either ANSI Type 3 or 4 category and have a thicker cross section near the central bore, which gradually tapers down towards the outer diameter

- Segmented wheels come in various styles, but their defining feature is the segmented arrangement of abrasive sections on the wheel's surface.

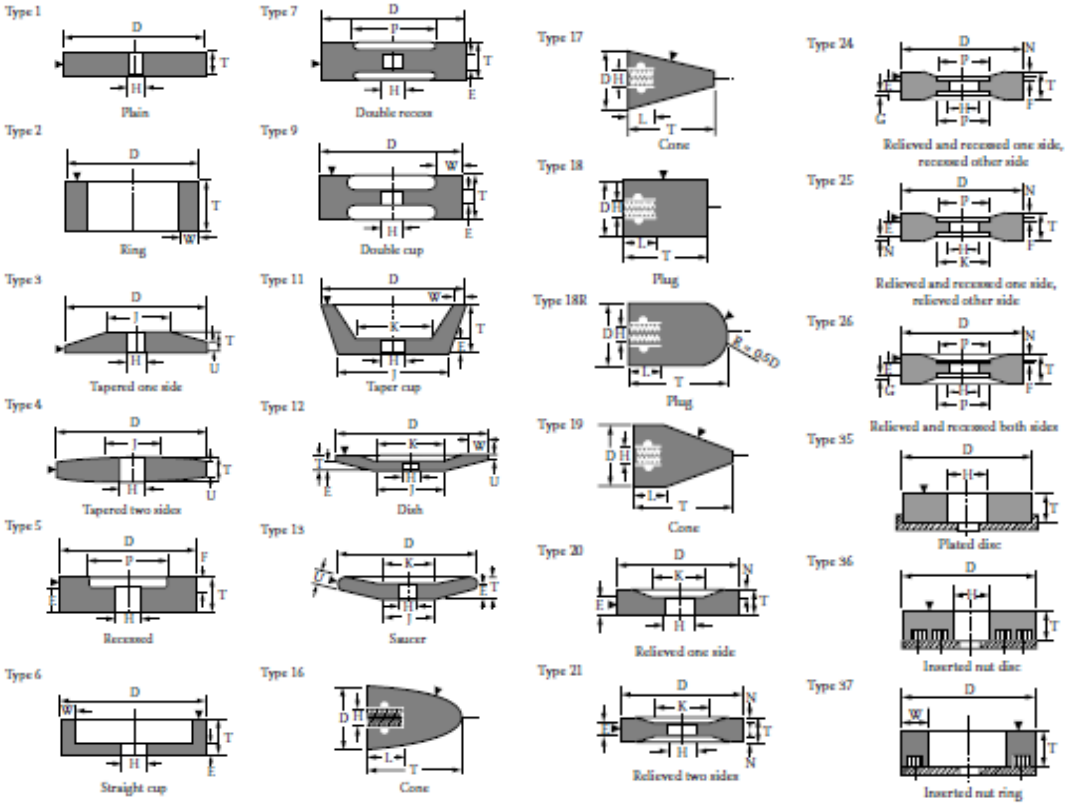

Figure 10. International Standard Shapes for Conventional Wheels [3]

Other of the strategies for correct grinding with profile grinding wheel is dressing. It is an important step in the profile grinding process. Dressing is used to condition the grinding wheel and produce a precise and consistent surface on the workpiece. The dressing process involves removing the dull and worn abrasive grains from the grinding wheel and exposing fresh and sharp abrasive grains (see Figure 11.) to ensure that the grinding wheel can grind accurately.

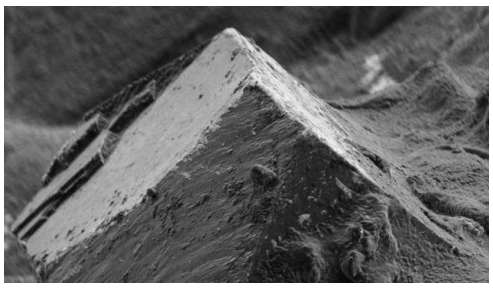

Figure 11. Sharp Cutting Edges of a CBN Grit seen in SEM. [32]

There are several methods of dressing a profile grinding wheel. Here are some of them:

- Single-point diamond dressing: This method is a a commonly used method for shaping a profile grinding wheel. This involves using a single-point diamond to remove

material from the surface of the wheel, allowing the creation of various shapes and profiles. It is suitable for grinding wheels made of aluminum oxide, ceramic, and silicon carbide abrasives. However, it's important to note that this method should not be used on CBN grinding wheels [33]

- Form dressing: This method involves using a form or template to shape the grinding wheel. The form is pressed against the wheel while it is rotating, and the wheel is ground to match the shape of the form. For example, in order to modify the profile of a gear, a diamond dressing tool is used as shown in Figure 12. The tool moves parallel to the worm's axis at a helix angle while the worm turns. Since each modification requires a new profile, a new diamond dressing tool must be used each time [34].

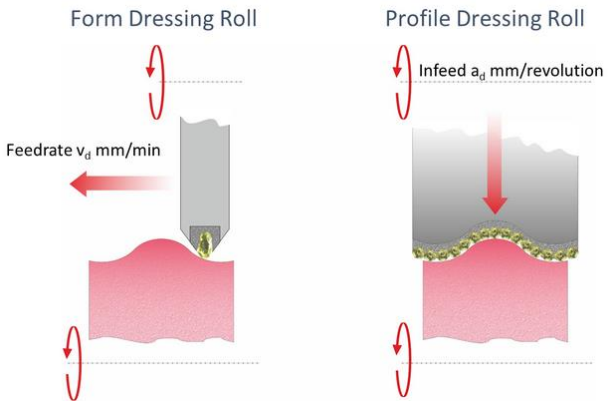

Figure 12. Dressing with rotatory diamond dressers [35].

- Electroplated diamond dressing: This method uses an electroplated diamond tool to shape the grinding wheel. The diamond tool is shaped to match the desired profile, and it is then used to grind the wheel to the desired shape. The abrasive grains onto the surface of the wheel body electroplated are fixed. Due to the irregular shapes and sizes of the grains, the resulting tools have a rough profile.

- Abrasive dressing: This method involves using an abrasive material, such as a grinding stone, to shape the grinding wheel. The abrasive material is pressed against the wheel while it is rotating, and it removes material from the surface of the wheel.

The method used to dress a profile grinding wheel will depend on the specific application and the desired profile. Each method has its own advantages and disadvantages, so it's important to choose the method that is best suited for the particular job at hand.

The next strategy is the grinding parameters. The grinding parameters, such as the wheel speed, feed rate, and depth of cut, should be carefully controlled to achieve the desired profile and surface finish. The appropriate wheel speed is dependent on several factors, including the material being ground, the type of grinding wheel being used, and the specific profile being ground. For the case of helical gears [36], the wheel speed is low to ensure the self-sharpening in the grinding wheel. The wheel speeds for rough grinding range from 24 to 30 m/s, while for finishing, they typically range from 30 to 35 m/s. On the one hand, the feed rate is dependent on the speed ratio q_s, with a standard machine typically having a feed rate of around 3500 mm/min. On the other hand, the depth of cut a_e is depend on the Q'_w , which value is determined by the type of process being applied. The feed rate and depth of cut is selected based on the material being ground and the hardness of the grinding wheel.

A lot of studies are currently being conducted to investigate important topics such as surface finish, grinding burns and wear. One example is a study [7] where the authors created a theoretical model to predict surface finish in profile gear grinding. This model combined the movement of the grains and a previously established method for calculating material removal to accurately predict the surface finish of the gear. The model is tested using a 3.8788 mm module gear made of 12Cr2Ni4A material and a 3SGA80F10V grinding wheel. The results of the study are found to align well with experimental data, with differences of less than 10% in 3D roughness measurements. There are also similar studies that have focused on how contact conditions affect thermal behavior during grinding. For instance, in another study [37], the authors performed a comprehensive thermal analysis of a fir-tree type DZ125 nickel alloy workpiece and a single-layered CBN grinding wheel. They used a set of grinding tests to analyze how various grinding parameters affected temperatures and forces. They also developed a new thermal model that took into account the shape of the contact zone and heat source in relation to the grinding process. The results showed deviations of less than 1.5% for the maximum temperature predicted.

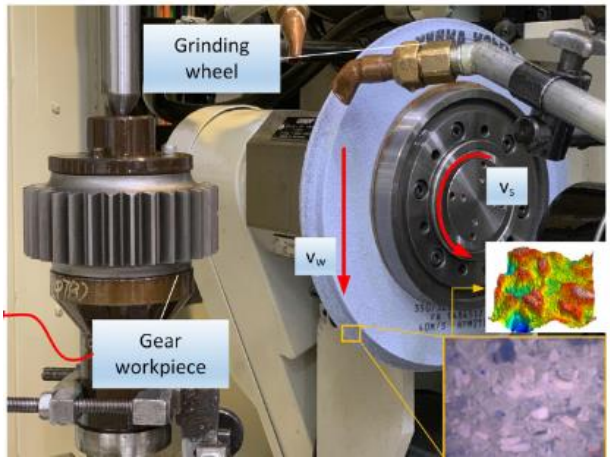

Figure 13. Profile grinding wheel and gear in grinding setup [7]

Currently, there are limitations associated with profile wheel grinding, such as non-symmetrical wheel profile, temperature distribution, and non-uniform coolant flow. When grinding asymmetrical profiles, there can be a major issue with the axial forces that occur. This can cause the grinding wheel to deform in the axial direction, resulting in an incorrect final profile. This can affect the accuracy and precision of the final product [38]. Another significant limitation is the temperature distribution, where the temperature concentration can form at corners and it may result in a local zone. Consequently, it may lead to thermal damage in the workpiece [38]. In addition, a limitation important to consider is the non-uniform coolant flow in the profile grinding wheel [39]. This makes it even more critical, as it increases the forces and temperature during the process. To avoid these limitations the grooved grinding wheels on profile grinding wheel is required. However, although multiple techniques have been created to make grooved grinding wheels, no method exists to produce groove on the profile grinding wheel [40]. Despite these limitations, research and development in the field of profile grinding wheel continues to push the boundaries and improve upon current methods.

2.3.2 Vitreous bond wheels

Vitrified super abrasive technology is currently the fastest-growing field in the precision grinding market. Vitrified bond wheels, which represent approximately 50% of conventional wheels, have gained significant popularity [41]. The function of the vitreous bond is to encapsulate the abrasive grains and bind them together with a spacing. In Figure

14, it can be observed that there are two grains joined by a vitreous bond, with a length of 0.100 mm and a thickness of 0.040 mm. The vitrified bond offers several advantages in grinding applications. Firstly, it enhances the transportation of cooling lubricants, effectively reducing thermal stress on the workpiece. Secondly, providing structural support to the abrasive grains and maintaining the desired separation between them. Additionally, the porosity of the vitrified bond facilitates efficient chip removal during grinding operations.

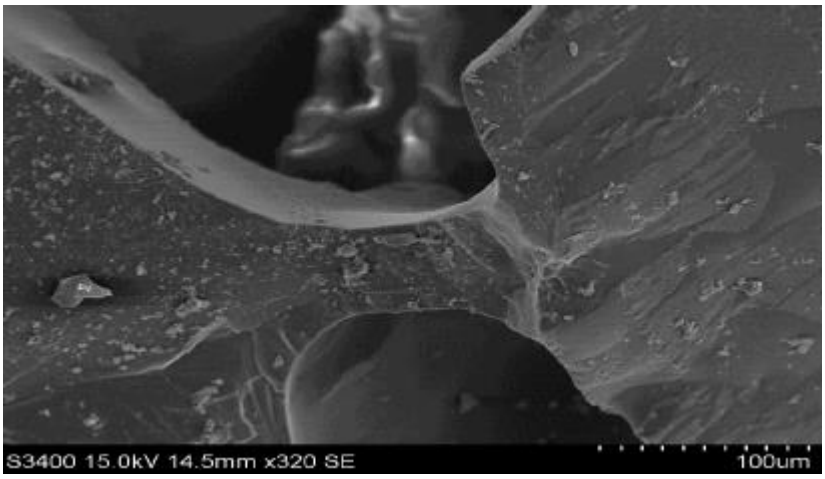

Figure 14. Vitreous bond between two abrasive grains [42]

However, the vitreous bond, despite its excellent ability to maintain the sharpness of the abrasive wheel, does have a drawback in terms of brittleness. This brittleness increases the risk of bond breakage. Despite this limitation, the importance of vitreous bonding materials remains clear. Recent publications [43]–[46] have focused on the development of new formulations for ceramic bonds. These studies have not only described these new bond compositions but have also established their improved grinding performance through systematic grinding tests.

Vitreous bonds are compounds composed of silicates, quartz, feldspar, kaolin, and frits [3]. The main ingredients of vitreous bonds include borosilicate glass, lead glass, and other vitreous materials with low melting points. Although manufacturers do not provide information about the composition of the vitreous bond due to confidentiality concerns surrounding their products, Herman and Kroz mentioned that a commercial glass bond belongs to a system known as Na_2O-K_2O-Al_2O_3-B_2O_3-SiO_2 [47]. These components allow for control over the porosity of the wheels and, in combination with volumetric proportions, provide strength to the bonding bridges. Unlike other bonding agents, vitreous bonds

exhibit a significant number of pores in the wheel structure, which contributes to their high-temperature resistance, fragility, and rigidity. In addition, throughout the grinding operation, vitrified bonds demonstrate exceptional bonding capabilities, enabling them to effectively manage the grinding wheel profile, withstand maximum load carrying capacity, exhibit flexibility, and maintain excellent corner retention properties. The flexibility allows for conditioning the topography of these grinding wheels to achieve a wide range of metal removal rates and surface finishing characteristics. The appearance of vitreous bonds can vary due to differences in ingredients and sintering conditions. Furthermore, they are highly effective in material removal.

The vitreous bond exhibits the advantageous capability of dressing. Dressing involves the removal of dull or worn abrasive grains, facilitating the exposure of fresh cutting edges and reducing pore clogging within the grinding wheel [48]. This process effectively maintains the sharpness and profile of the grinding wheel, contributing to its sustained performance and longevity [49].

It is worth noting that vitreous bonds are not used in high surface speed applications, except for when the speed is below 120 m/s [41]. In conventional precision grinding, alumina grains are predominantly used in vitrified bonds. However, in superabrasive grinding, which represents less than 20% of the total market, vitrified CBN (cubic boron nitride) is the preferred choice.

2.3.3 Kinematics

The grinding process is conceptually similar to micromilling [50], wherein the abrasive grains on the grinding wheel act as miniature cutting tools, machining the material in a manner of a scaled-down milling operation. Notably, the grinding process exhibits a stochastic nature, with abrasive grains possessing distinct geometries and being randomly distributed across the grinding wheel surface. Consequently, each grain removes a varying amount of material during the process. As a result, investigations into grinding phenomenon at both macro and micro scales need the using of statistical calculations to derive meaningful insights and draw reliable conclusions.

In order to define the appropriate grinding process parameters, a thorough examination of the kinematics is crucial. These parameters play a vital role in predicting key outcomes such as surface roughness, power consumption, grinding wheel wear, and thermal considerations [41]. Among the several parameters involved, two of particular significance are the geometric contact length (l_c) and the chip thickness (h_{cu}).

The contact length serves as a vital machining parameter, providing insights into the extent of interaction between the surface of the grinding wheel and the workpiece [50]. This parameter, along with the width of the pass (b_s), allows obtaining the contact area between the grinding wheel and the workpiece. Since the width of the pass remains constant in common grinding operations, the contact area is directly related to the contact length. Assuming the grinding wheel and workpiece to be non-deformable, the contact length can be determined geometrically. It is defined by the arc length, Eq. (1), which relies on the geometric contact length determined by the depth of cut and the grinding wheel diameter, Eq. (2). Additionally, the deflection of the grinding wheel is influenced by its deflection and diameter, also contributes to the geometric contact length (see Eq. (3)). However, it is important to note that the actual contact length surpasses the geometric contact length by two to three times [51], owing to the deformations experienced by the grinding wheel as a result of contact forces.

$$l_c^2 = l_g^2 + l_f^2 \tag{1}$$

$$l_g = \sqrt{a_e \cdot d_s} \tag{2}$$

$$l_f = 2\sqrt{\delta \cdot d_s} \tag{3}$$

The effects of the actual contact length and the geometric contact length are illustrated in Figure 15. As depicted in this geometric analysis, it is assumed that elastic contact exists between the two bodies without any load. After applying a load, the penetration (δ) is obtained from the equivalent diameter of the contact diameter (d_3) against the curved surface of the workpiece. After removing a load, the workpiece recovers the diameter d_2.

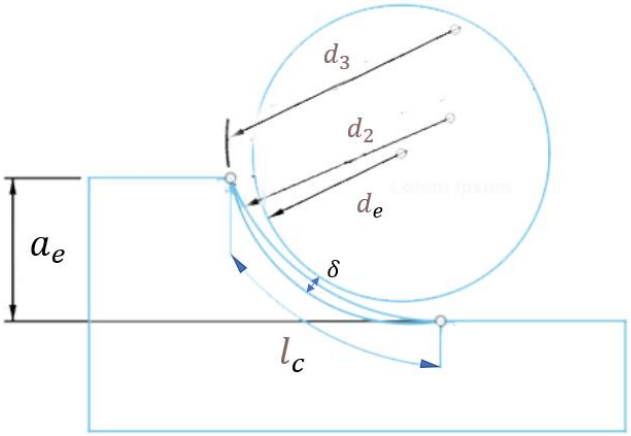

Figure 15. Grinding wheel combining the effects of depth of cut a_e and the deflection.

On the other hand, according to Hertz, the contact length between smooth bodies (assuming the grinding wheel and workpiece are two parallel cylinders) is determined by the following equation:

$$l_c = l_f = \sqrt{\frac{8\,F_n'\,d_e}{\pi\,E^*}} \tag{4}$$

where F'_n is the specific normal force, d_e is the diameter of the grinding wheel and E^* is the equivalent modulus of elasticity. E^* represents the elastic properties of the grinding wheel and workpiece. To calculate E^*, the Poisson's ratio and modulus of elasticity of both the grinding wheel and workpiece are required. The elastic deflection between the abrasive grain and the workpiece due to the normal grinding force. The equation is expressed as follows:

$$\frac{1}{E^*} = \frac{1-\nu_s}{E_s} + \frac{1-\nu_w}{E_w} \tag{5}$$

Combining equations (1), (2) and (4) the expression becomes:

$$l_c = \sqrt{a_e d_s + \frac{8\,F_n'\,d_e}{\pi\,E^*}} \tag{6}$$

This formula applies when both surfaces are smooth. However, in reality, this is far from accurate as the surfaces are rough when observed microscopically. Therefore, Rowe and Qi introduced the term rough surface or roughness factor (R_r) into the contact length

equation by incorporating the elastic contact model proposed by Greenwood and Tripp. The resulting equation is as follows:

$$l_c = \sqrt{a_e d_s + \frac{8\, F_n'\, R_r\, d_e}{\pi\, E^*}} \tag{7}$$

The rough surface parameter is determined experimentally and is directly linked to the increase in surface roughness. According to Rowe and Qi, this factor varies between 7 to 23 [51] depending on the characteristics of the surface roughness. However, Marinescu [3] consider a typical value of $R_r \approx 5$. As can be observed, this factor exhibits a wide range of variation in the calculation of the contact length, and its value has a significant impact.

Another parameter that plays a pivotal role in the kinematics of the grinding process, representing the amount of material that each abrasive grain removes is the uncut chip thickness [50]. Calculating the maximum uncut chip thickness involves assuming a uniform distribution of abrasive grains and a specific spacing, denoted as L. Furthermore, *s* can be defined as the horizontal distance traveled by the grinding wheel from the engagement of one grain to the engagement of the next as illustrated in Figure 16.

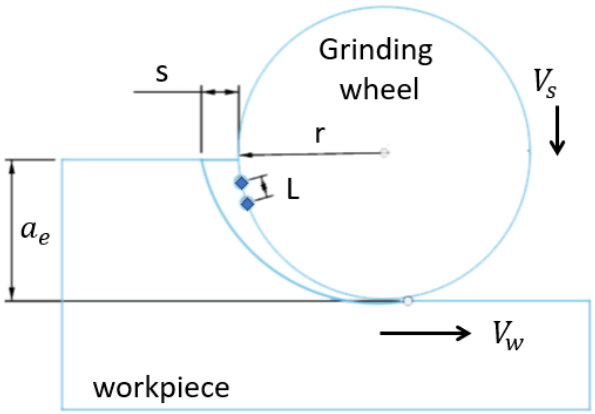

Figure 16. The displacement of two consecutive grains during the grinding process.

The chip thickness is not a constant value but rather fluctuates between 0 and its maximum value, h_{cu_max}. As described by Eq. (8), modifying the feed rate or reducing the grinding wheel speed results in an increased chip thickness. Consequently, this increase of chip thickness exposes each abrasive grit to higher forces, thereby raising the likelihood of grit breakage and/or bonding breakage.

$$h_{cu\_max} = 2L\frac{v_w}{v_s}\sqrt{\frac{a_e}{d_s}} \tag{8}$$

The forces at play serve as critical indicators of process quality. When compared to milling and turning operations, grinding forces are typically smaller in magnitude. These forces encompass the normal force, tangential force, and axial force. The normal force, responsible for sparking and deformations, arises from the frictional interactions and is closely tied to grain wear. It directly influences the contact length between the grinding wheel and workpiece. Meanwhile, the tangential force correlates with power consumption in the machine spindle and contributes to the generation of heat. As for the axial force, it primarily induces lateral deformation; however, its impact remains minor, as it is effectively absorbed by the clamping plate through screws. In general, the normal force (F_n) tends to be three times larger than the tangential force (F_t), reflecting the relative magnitudes of these forces in grinding operations.

The grinding process is widely recognized as an energy-intensive operation, primarily attributed to its substantial power consumption relative to the amount of material removed. This characteristic is encapsulated by the concept of specific energy consumption, which quantifies the power required to achieve a specific material removal rate. The inherent energy inefficiency of grinding arises from the nature of material removal, wherein a significant amount of energy is expended to remove relatively small volumes of workpiece material. Therefore, the eq. (9) is represented as follows:

$$e_c = \frac{F_t v_s}{b_w a_e v_w} \tag{9}$$

2.3.4 Contact mechanics

Contact mechanics in the grinding process involves the examination of the interactions and forces exerted by the grinding wheel on the workpiece during the grinding operation. The grinding wheel undergoes deformation and penetration into the workpiece. In this field of study, factors such as contact forces, contact areas, and pressure distribution need to be considered.

Contact mechanics is a discipline that delves into the analysis of stresses and deformations that arise when two solid bodies come into contact. It encompasses various theories and models that aid in understanding contact behavior and predicting its outcomes.

One significant theory in contact mechanics is the Hertzian theory of non-adhesive elastic contact. Proposed by Heinrich Rudolf Hertz in 1881 [52], this theory provides a fundamental framework for solving contact problems involving elastic bodies with curved surfaces. Its primary focus is on non-adhesive contact, where tensile forces are not permitted within the contact area. The Hertzian theory has been extensively employed through analytical, empirical, graphical, and numerical approaches to tackle a wide range of contact problems.

Another essential theory is the Coulomb friction theory, which explains the generation of frictional forces when two surfaces come into contact and slide relative to each other. Often used in conjunction with the Hertzian theory, it allows for the modeling of contact between rough surfaces. For instance, researchers such as Lui et al. [53] have used both theories to develop contact models for single asperities on rough wheel surfaces under normal or side contact conditions.

Additionally, the study of indentation stress fields plays a crucial role in contact mechanics. This theory focuses on the distribution of stresses that occur when a hard indenter, such as a hard sphere or a sharp diamond tip, is pressed into a softer material [54]. This process leads to the creation of a region characterized by high stress and deformation. The Hertzian theory is commonly employed to model the elastic deformation of the material, while plastic deformation is addressed using the theory of plasticity.

Lastly, it is essential to consider adhesion and friction forces, which are often overlooked in the Hertzian model but can be significant in certain situations. Adhesion refers to the attractive forces that exist between different materials when they come into contact, while friction is the resistance to relative motion between two surfaces in contact. Researchers have developed models that incorporate adhesion and friction forces to gain a better understanding of contact behavior at the nanoscale.

When two objects come into contact, they undergo elastic deformation, leading to the generation of forces and resulting in surface deformations. The Hertz theory provides a

framework to describe this elastic deformation and allows for the calculation of the contact area. Based on this theory, the distribution of stresses throughout the contact area can be determined.

In the context of static contact between a rigid geometry, such as a sphere, and a half-space, Heinrich Hertz formulated an analytical expression. This expression, denoted as Eq. (10), mathematically represents the contact behavior between the sphere and the half-space. It takes into account the properties of the contacting bodies, such as their elastic moduli and geometry and defines the force-penetration relationship between these bodies.

$$F = \frac{4}{3} E^* R^{1/2} \delta^{3/2} \tag{10}$$

Where, F is the force, E^* is the young modulus of both materials, R is the radius of the sphere and δ is the penetration. The analytical formulation derived by Hertz enables the estimation of contact pressures, the determination of contact areas, and the prediction of stress distributions within the contact region. A theory of contact between two elastic rough surface enables us to predict the normal and shear elastic properties of the surfaces [55].

As it is seen in Eq. (10), the elastic behavior of surfaces in contact is influenced by several important parameters, including the modulus of elasticity and the surface geometry. The modulus of elasticity, also known as Young's modulus, is a material property that determines its stiffness. It is defined as the ratio of stress to strain under tensile or compressive tests. Young's modulus can be expressed as:

$$E = \frac{\sigma}{\varepsilon} \tag{11}$$

where σ is the stress and Ɛ is the strain. Each material has a specific Young's modulus that provides information about its mechanical characteristics. Higher values of Young's modulus indicate a stiffer material, while lower values correspond to less rigid materials. The Young's modulus of the grinding wheel is considered as continuous medium, and its value is much lower than that of the abrasive grains due to the porosity present in the wheel. The units of Young's modulus are in pressure, such as pascals (Pa). By knowing the actual Young's modulus, one can predict the material's response to applied loads. This knowledge is crucial for designing of the model to ensure their mechanical integrity and performance.

Another parameter that influences elastic behavior is the geometry of the contact surfaces. The shape and roughness of the surfaces play a significant role in determining the stresses and deformations. On one hand, if the shape has a more pronounced curvature, the contact area increases, leading to higher stresses and deformations. On the other hand, the roughness of the surfaces affects the contact area. Rougher surfaces tend to have higher contact areas, resulting in reduced contact pressure.

According to Zhang et al [56] the Young's modulus of the grinding wheel is influenced by various factors, including temperature, specific gravity, type of grain, hardness, total volume of the grinding wheel, volume of the grain, as well as the fraction and type of the bond material. Additionally, the Young's modulus of the bond depends on the interatomic strength of the bond and the state of its packing. Hence, the Young's modulus of the grinding wheel is highly dependent on the Young's modulus of the applied bond.

It is well known that material removal in grinding is achieved through the action of abrasive grains, and that the contact of each abrasive grain generates the grinding forces. Once the abrasive grains come into contact with the workpiece, they initiate grit penetration. Grit penetration refers to the depth at which the abrasive grains of the grinding wheel penetrate into the workpiece during the grinding process. It is a critical factor that directly influences the amount of material removed and the surface roughness of the workpiece and consequently, in the process outputs such as heat, force and grinding wheel wear. A higher grit penetration results in a greater material removal rate. However, it also leads to a lower surface quality due to the increased surface roughness.

Controlling the degree of grit penetration is essential to achieve the desired grinding outcomes. Various factors impact the grit penetration, including the properties of the grinding wheel, such as the hardness, the abrasive grain size and shape, the grinding parameters, such as the grinding speed and feed rate, and the workpiece material properties and the applied pressure of the grit penetration. For instance, by selecting a grinding wheel with finer grains the grit penetration can be reduced, resulting in a lower material removal rate and a finer surface finish. Adjusting these parameters allows for the control of the grit penetration and, subsequently, the material removal and surface roughness.

Macerol et al. [57] conducted a study on the effects of grit properties, including toughness, thermal stability, and grain shape, as well as dressing on the grinding process. They found

that single-layer or electroplated grinding wheels typically exhibit a rougher surface and more prominent grit protrusion compared to vitrified-bonded grinding wheels.

Palmer et al. [58] conducted a study that demonstrated the significant impact of abrasive grit morphology on grinding performance. One notable finding they presented is the effect of elongated abrasive grits, which resulted in the formation of the roughest workpiece surface roughness. This outcome can be attributed to the larger grain size, which leads to an increased penetration depth.

2.4 Wear phenomenon of the grinding wheels

2.4.1 General description

Current research trends are focused on finding solutions to enhance the life expectancy of grinding wheels. The grinding wheel, being the most expensive component in grinding operations, undergoes wear as it comes into contact with the workpiece. The life expectancy and wear of the wheel are intricately linked to the topological evolution of the wheel surface, which is influenced by the forces exerted during the grinding process. Moreover, the wear of the grinding wheel directly impacts its efficiency [59]. Consequently, reducing grinding wheel wear is a topic of great industrial interest, aiming to prolong wheel lifespan.

Grinding wheel wear manifests in both the abrasive grains and the binder, as a result of the forces encountered during grinding. The wheel undergoes a wear process during its interaction with the workpiece. The contact between the workpiece and grinding wheel during the process is characterized by very high pressures (1-2 GPa), chemical reactions and high relative speeds (>30 m/s) [3]. This leads to modifications to the shape, quantity, and arrangement of the abrasive particles on the surface of the grinding wheel. Consequently, it produces a progressive wear of the grinding wheel which makes it lose its cutting capacity. The grinding wheel wear means the gradual reduction in size and shape of a grinding wheel. The wear has negative consequences in the grinding process. It affects the final quality of the parts, causes loss of dimensional tolerances, productivity, and leads to changes in process parameters. In addition, if the grinding forces exceed, they can cause

damage that very negatively affects the behavior to the part fatigue [60]. Therefore, the study of grinding wheel wear is a significant area of research.

In terms of the vitrified bond, it needs to be sufficiently strong to maintain the grains under normal grinding conditions, yet capable of controlled grain fracture under higher stress conditions [3]. The quest to mitigate grinding wheel wear encompasses advancements in material composition, bonding techniques, and surface topography to enhance wheel durability and optimize grinding performance.

2.4.2 Wear mechanism

Building on the impact of grinding wheel wear on the grinding process, it is crucial to understand the mechanisms behind it. As shown in Figure 17, regarding to the classic grinding references [2], [3], there are three mechanism of grinding wheel wear: attritious wear, grain breakage and bond fracture. These wear mechanisms can occur due to a variety of factors including the properties of the grain abrasive and bonding system, the forces applied to the wheel during grinding, and the properties of the workpiece being ground. In addition, the wear mechanisms can vary depending on the combination of the grinding wheel and the workpiece material. For example, Duwell and McDonald [61] has shown that when grinding mild steel with silicon carbide grits, the dominant wear mechanism is attritious wear. However, when using aluminum oxide grits to grind the same material, both attritious wear and grain breakage can occur. This demonstrates that different grinding wheel-workpiece pairs can exhibit different dominant wear trends. In order to know the different characteristics of the three wear mechanisms, details will be given below.

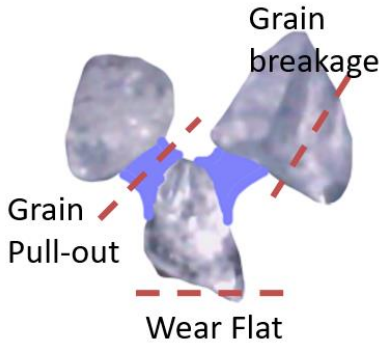

Figure 17. Grinding wheel wear mechanism

Attritious wear are usually formed on the edges of the abrasive grains by rubbing against the workpiece. The contact between cutting edges and material produces grain abrasion. The attritious wear can likely occur when the force applied to individual abrasive grains is low and the temperature of the grinding process is high. The high temperature causes thermal damage and low workpiece accuracy. Also, they can reduce the effectiveness of the grinding wheel, making it less efficient at removing material from the workpiece. Comparing with other wear mechanism, the volumetric wear is negligible.

Grain breakage refers to the fragmentation of the abrasive grains by fracture. It occurs when the abrasive particles on the wheel break due to the mechanical and thermal stresses and strains of the grinding process. These stresses cause microcracks that eventually produce micro-fracture. This in turn can create new sharp, but normally inactive cutting edges on the surface of the wheel. Also, this wear mechanism may lead to shelf-sharpening and consequently reduce attritious wear areas.

The bond fracture is a phenomenon in which abrasive grains are extracted of the bonding material. As well as the grain breakage mechanism, the bond fracture may lead to shelf-sharpening and consequently reduce attritious wear areas. Comparing with other wear mechanism, the volumetric wear is considerable, which is typically measured using the grinding ratio G. It can also cause the grinding wheel to become imbalanced, leading to vibrations and affect to final dimensions of the workpiece. In Figure 18, the phenomenon of bond fracture can be observed in an electroplated CBN wheel, where the entire grain detaches from the wheel.

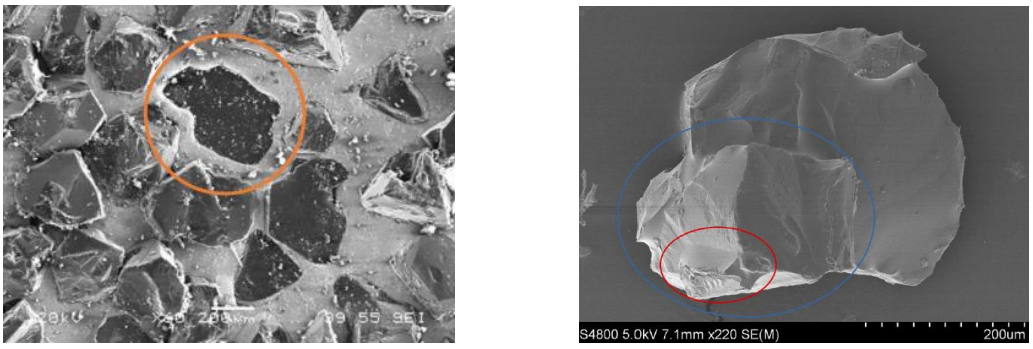

(a) (b)

Figure 18. Bond fracture phenomenon. (a) Electroplated CBN wheel [62], (b) Vitrified alumina grinding wheel [42].

These mechanisms wear is directly linked to its durability. According to Jackson [63], durability is influenced by the depletion of grain, which is dependent on both the strength of the bonding material and the protrusion of the abrasive grains. In this case, the strength of the bonding material is particularly significant as it ensures effective interaction between the abrasive grains and the workpiece, as well as bearing the forces of grinding, heat generation, and surface quality. Furthermore, the strength of the bonding material serves as a crucial indicator of the grinding wheel's overall quality. While the selection of a grinding wheel is typically based on the characteristics of the abrasive grains, the development of new combinations of bonding materials with exceptional mechanical properties has enabled an increase in their bending strength compared to conventional wheels [64]

2.4.3 Wear characteristic

As it mentioned above, to characterize the volumetric wear, the grinding ratio or also called G-ratio is a parameter commonly used [2]. This parameter is obtained from the volumetric wear of the grinding wheel and the removal volume of the workpiece in the steady state regime as shown in Figure 19.

The grinding ratio can be expressed as follows:

$$G = \frac{\Delta V_w}{\Delta V_s} \tag{12}$$

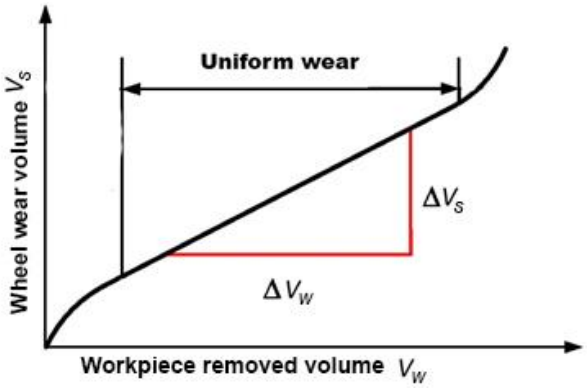

Figure 19. Wear pattern of grinding wheel [65].

where ΔV_w is the workpiece removed volume y ΔV_s is the wheel wear volume. During the grinding process both grinding wheel and workpiece lose material. The grinding ratio has reached over 60,000 [66]. This depends on several factors, such as the type of grinding wheel, type of workpiece, the grinding conditions, and the duration of the grinding process. This parameter is key in assessing the efficiency and effectiveness of the grinding process, as well as in predicting the wear of the grinding wheel.

With the mechanism wear characteristics detailed above, the grinding wheel wear can have significant impacts on the accuracy and precision of finished parts, especially when grinding critical components. In a study by Miao et al [5], used vitrified microcrystalline alumina wheels for the creep feed grinding of fir-tree geometries on turbine blade roots made of a Ni-based alloy. The authors found that wear is more pronounced on the peaks of the grinding wheel compared to the valleys, and that various wear mechanisms contributed to this wear. They also identified the fracture of bond bridges as a key factor in wear in the peak regions. Based on these findings, the authors developed an experimental model for predicting grinding wheel wear. Overall, the grinding wheel wear is influenced by the composition of the grinding wheel and the grinding process conditions.

The grinding wheel wear of the profile grinding wheel can be influenced by the dressing and grinding parameters [5] in the profile grinding wheel. Research in the scientific community has shown that several factors governing wheel wear, including the type of abrasive material, the hardness, the grinding wheel speed, the feed rate, the depth of cut, and the type of coolant used. Additionally, the type of workpiece material, bond volume and its hardness can also have an impact on the volumetric wear of the wheel. Gong et al [67] studied the influence of grinding parameters in the wear of the micro grinding tool when grinding soda-lime glass. The study shows that the higher the feed and grinding speed, the greater the wear of the abrasive. Additionally, as more material is removed, the diameter of the micro grinding tool decreases rapidly initially and then gradually. Overall, the surface roughness of the material decreases as the process progresses. Thus far, higher wheel speeds, deeper cuts, and harder workpiece materials will result in increased volumetric wear of the profile grinding wheel. The use of coolant can also help to reduce wear by reducing heat and friction at the grinding interface. Therefore, to improve the limitations on the grinding process caused by wear, understanding the wear mechanisms

and the grinding parameters can help to minimize the impact of grinding wheel wear on the workpiece.

To mitigate excessive wear of the grinding wheel, special techniques are employed. These techniques include supplying an appropriate grinding fluid, using special dressing methods, employing an open structure wheel, and operating at high cutting speeds [68]. These techniques enable a significant increase in the G ratio.

To minimize the impact of grinding wheel wear on the workpiece, an appropriate dressing method must be used [69]. Regularly dressing the wheel with a dressing tool ensures that the wheel is properly balanced. Consequently, it can help to reduce the stresses and strains on the abrasive particles and minimize the risk of volumetric wear. Huang [70] states that the intensity of the dressing process affects the surface quality of the workpiece. They indicate that a higher dressing intensity results in larger, sharper edges on the wheel, which in turn leads to deeper grooves and lower forces on the workpiece, while a lower intensity produces a greater number of smaller edges, resulting in a smoother surface and higher grinding forces. Therefore, it is important to find the right balance between the dressing intensity, the regularity of dressing, and the wheel balance to achieve the desired surface quality of the workpiece while minimizing the impact of grinding wheel wear.

2.4.4 Bond fracture

One aspect of grinding wheel wear that has received significant attention in the literature is the bond fracture phenomenon, which can affect both the volume of wear (as measured by the grinding ratio) and the accuracy of profiled precision wheels. However, due to intellectual property considerations, there is limited information available on the characteristics and behavior of vitreous bonding materials. In a classic paper [71], proposed a bond-stress factor to account for the likelihood of vitreous bridges fracture. Herman and Markul [72] investigated how altering the composition of the vitrified bond affects reducing the volumetric wear on the grinding wheel. They presented results showing that the use of a glass-crystalline bond in grinding wheels can increase the G-ratio by up to 10 times compared to a common glass bond. This behavior is related to the presence of intergranular boundaries in the glass-crystalline bond, which can inhibit or stop crack

propagation. Such bonds also exhibit higher values of fracture toughness, up to 3 times those of conventional glass bonds. These findings are later confirmed in a study by Herman and Krzos [47] on the volumetric wear of polycrystalline vitreous CBN wheels. They confirm that the wearability is attributed to the interatomic bond strength and the microstructure of the grain bond bridge network. In this work, the radial wear on a grinding wheel with a glass-crystalline bond is 28% less than on a wheel with a traditional glass bond (see in Figure 20). The research design allows a deeper understanding of the mechanical characteristics of different bond types.

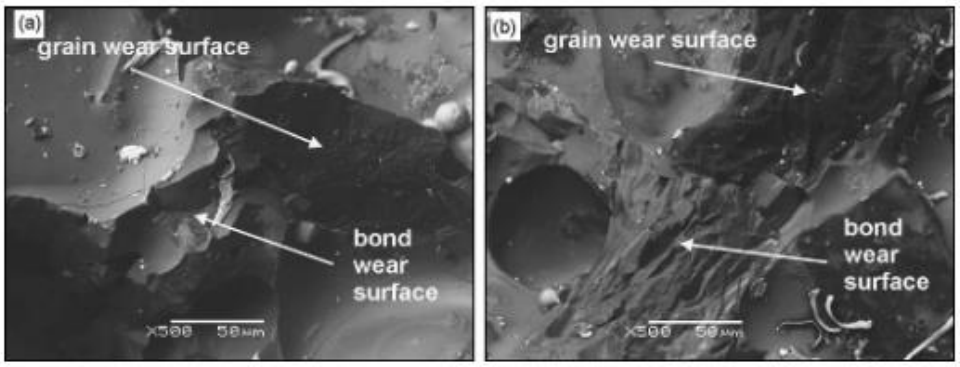

Figure 20. Wear of the bond of the CBN grinding wheel (a) with conventional glass bond (b) with glass crystalline bond [47].

Moreover, in the Gómez and Sánchez's work [42] observed by SEM images that there was porosity in the central area of the fracture of the vitreous bond as shown in Figure 21. This porosity is generated due to bubble defects that form within the binder during the sintering of grinding wheels. These defects act as stress concentrators and promote crack propagation. Gómez and Sánchez's findings highlight the importance of understanding the influence of manufacturing processes on the structural integrity of materials. The presence of porosity or voids within a material can significantly affect its mechanical properties, including its rigidity and strength.

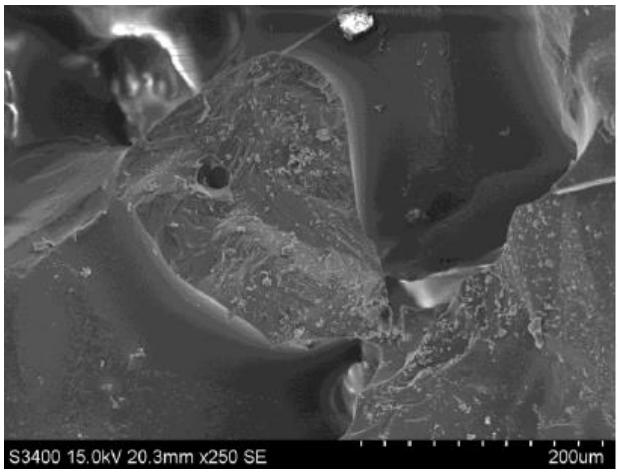

Figure 21. Fracture of the vitreous bond in the grinding wheel [42].

Despite the limited information on vitreous bonding materials, one of the most comprehensive sources of information on the behavior of components and sintering conditions for grinding wheels is a PhD thesis by Jackson [73], which provides a detailed analysis of the reactions that govern the sintering of vitreous bonding materials. Jackson later continued his research [74] to examine microscale wear in grinding wheels, considering both grit fracture and bond fracture. This study examines how the process of sintering affects the mechanical properties of vitreous bond. Also, in the case of vitrified alumina grinding wheel, the authors found that the theory of brittle fracture applies to both abrasive and vitreous bonding, and that the application of cyclic thermo-mechanical loads leads to crack propagation and eventually fracture. The dressing process is closely linked to the initial presence of microcracks. Another study [75] examined the effect of thermal loads on the abrasive grain, but did not consider the differences in the coefficient of thermal expansion between bonding and abrasive materials. The authors suggest that the high temperatures that occur at the grit-workpiece interface may locally modify the properties of the ceramic grain, leading to the formation of attritious wear. They also note that there is a lack of understanding about the loads applied to both abrasive grains and their bonding bridges, and how these materials respond to these loads, which makes it difficult to relate grinding wheel wear due to fracture to specific grinding conditions.

Building upon Jackson's work, the volumetric wear of the grinding wheel can have a major impact on the accuracy of the machined parts. The volumetric wear is mainly due to bond fracture, which implies a dimensional loss and less precision of the grinding wheel.

Therefore, it is important to monitor the wear of the grinding wheel in order to maintain the precision of the contour surfaces in profile grinding.

Moreover, during the grinding process, the bond material in the grinding wheel is subjected to various types of wear mechanisms. While bond fracture refers to the breakage of the bond material, wear occurs as a result of the abrasive interactions between the chip material being removed and the binder. This wear can have different manifestations depending on the type of chip being generated [3].

When long-chipping material detaches from the workpiece, the flowing chip can cause damage to the bond at the grain cutting edges. The force and movement of the chip can result in the wearing down of the bond material in those regions.

On the other hand, when short-chipping material detaches, the wear process occurs through the lapping process. The chip material, instead of flowing smoothly, undergoes repeated contact and rubbing against the bond surface. This repetitive lapping action leads to gradual wear and erosion of the bond material.

According to Sieniawski and Nadolny [76], the most significant phenomena leading to fracture in the form of cracking or chipping in both abrasive grains and bonding agents are effective wear (mechanical shock load), fatigue wear (repeated mechanical shock load), and thermal fatigue wear (intermittent thermal shock load). These factors play a crucial role in the deterioration of the vitreous bond.

These considerations highlight the importance of understanding not only bond fracture but also bond wear in grinding processes.

2.4.5 Monitoring and analysis of grinding wheel wear.

The efficiency of the grinding wheel has a direct impact on the efficiency of the machining process and on the final quality of the workpiece. As such, it is crucial to monitor and assess wheel wear. However, to measure the profile grinding wheel can be quite complex due to the harsh conditions of the machining process. Fangyi et al [77] monitor and evaluate the wear of vitrified alumina grinding wheel during grinding the material Cr12. They use the method of histogram analysis to study the distribution of gray values in an image of the

wheel surface. The image is obtained by a camera type of ZQ-603 and it is placed near from the grinding wheel as it is shown in Figure 22a. This image is converted to binary form by determining a gray threshold value. This process allowed for the identification and calculation of worn areas on the grinding wheel. Another significant method to measure of the wheel wear is proposed by Rahman et al [78]. They develop a system for measuring the profile of a surface while it is still on the machine, using the principles of a coordinate measuring machine (CMM). In this research, a software compensation method is used during ELID grinding of an aspheric surface to compensate the grinding wheel wear. Other interesting method using Artificial Neural Networks (ANNs) is developed by Arriandiaga et al [79]. They create a virtual sensor for on-line monitoring the grinding wheel wear and surface finish. A Layer-Recurrent neural network architecture is presented for measuring of wheel wear and surface roughness in the grinding process by measuring power consumption in the wheel spindle. The sensor has been calibrated and its performance validated through comparison with actual measurements, showing excellent concordance. Similar to the previous method, Guoqiang et al [80] developed a multi-information fusion recognition model for assessing the wear status of a ceramic bonded CBN grinding wheel. This model uses a combination of BP neural network and genetic algorithm. The study tested the model by using the wheel to grind GH4169 alloy and evaluating the surface condition and shape accuracy of the wheel. The acoustic emission and grinding force signals are also analyzed during the grinding process and it is found that the ratio of these signals has a good concordance with the wear status of the wheel as determined by the experimental analysis. Unlike the above mentioned, Xu et al [81] create a new system for visually measuring the profiles grinding wheels and quantifying the wear during the process. They also developed a method of calibrating this new vision system. Figure 22b shows an illustration of system for visually measuring the profiles grinding wheels. The accuracy of the measurement results is verified. In addition, the compensation method is created for dressing of the grinding wheel. As it can be seen, various techniques have been presented for measuring the profiles of grinding wheels and monitoring of wheel wear. However, there is still room for improvement in these methods to make them more accurate, comprehensive and reliable in measuring volumetric wear of grinding wheels and understanding its impact on the precision of machined parts.

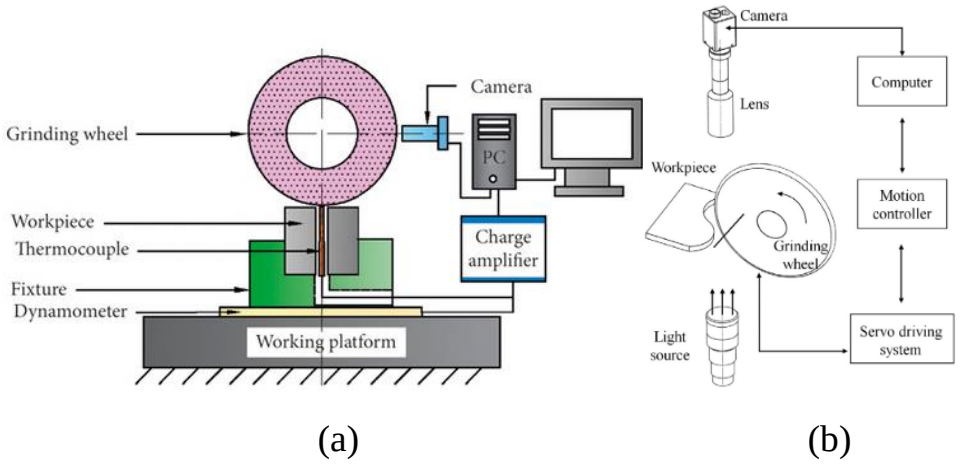

(a) (b)

Figure 22. Set up of experiment test for the measurement of the grinding wheel (a) Monitoring of the grinding wheel wear [77] (b) Machine vision measurement of profile grinding wheel [81]

Recent experiments have supported earlier discoveries about the characteristics of volumetric wear. A study in [82] examines the precision of grinding the inner ring groove of 6208 ball bearings. Thang et al created a new sensor that uses compressed air to measure grinding wheel wear in real-time. The sensor is tested using a profiled vitrified white fused alumina (A100L5V). The findings indicate that the wear is not evenly distributed, which affects the precision of the part. Multiple types of wear are observed, but it is found that a significant amount of wear occurred early on in the grinding process. This is because the abrasive grains easily detached from the bond, resulting in a high wear rate. A complete examination of wear patterns for various types of vitrified alumina wheels used in creep-feed grinding of Ni-based superalloys can be found in [34]. The authors acknowledged the presence of multiple types of wear and found that when the material removal rate is low, attritious wear, workpiece adhesion, and loading on the wheel are the dominant forms of wear. However, as Q' increased, the wear mechanism changed and it became clear that the grain fracture and bond fracture are occurring. This means that the fracture wear is the main cause and is responsible for inaccuracies in key areas and poor surface quality. In other study, Miao et al [6] examines how the wear of the grinding wheel impacts the process of shaping specific patterns on the roots of turbine blades. As it is shown in Figure 23, the researchers identified multiple ways in which the wear occurs in profiled vitrified microcrystalline alumina wheels, but found that the fracture of the bond bridges is particularly significant in the wheel peak regions. They developed a method for predicting the wear on the wheels based on their experiments, but did not take into account the strength of the materials. This highlights the importance of considering the mechanical properties

of the materials used in grinding wheels and as it can greatly impact the wear and performance of the wheel. Further research is needed to fully understand the behavior of grinding wheels under various conditions and how their mechanical properties can be optimized.

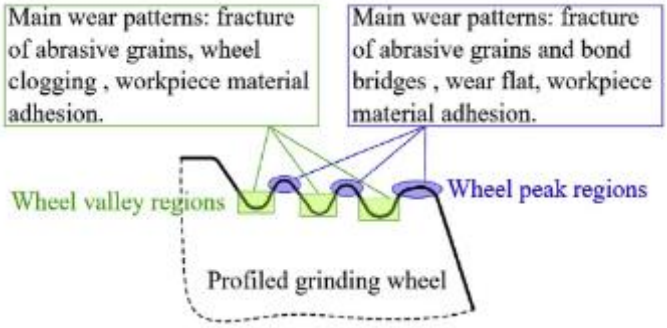

Figure 23. Wear patterns on the surface of profile grinding wheel [5].

Other method for measuring of radial wear of the grinding wheel is the graphite. Graphite is one of the most cost-effective, practical, and straightforward methods for measuring the wear of grinding wheels, especially in relation to the bond fracture phenomenon. Being a soft material, graphite allows obtaining the true profile of the wheel with a single pass. The pattern of graphite detachment can indicate the amount of radial wear on the wheel. One of its advantages is that it provides direct information about the radial wear of the wheel. However, the main disadvantage of graphite is that the graphite particles can adhere to the machine walls, leaving it quite dirty. One example of research that utilizes graphite is the work of Liu et al. [83], where they use a graphite sheet to obtain an accurate profile of the surface wear of the grinding wheel. The profile is marked on the graphite through contact with the wheel. Another case is the study conducted by Yu et al. [84], who imprint the arc profile of the diamond grinding wheel onto a graphite plate. Additionally, Shi and Attia [85] measure the radial wear of electroplated diamond wheels on graphite after grinding titanium alloys. Finally, in creep feed grinding Miao et al [5], using a measuring process to obtain the profile wear of the vitrified microcrystalline alumina grinding wheel, which the graphite allows to get the profile duplication of the grinding wheel. In summary, the use of graphite as a method for measuring the wear of grinding wheels offers a cost-effective and practical approach. While it provides direct information about radial wear, care must be taken to prevent graphite particles from contaminating the machine during the measurement process.

2.5 Mechanical and thermal properties of the grinding wheel

The grinding wheel's material plays a significant role in determining its performance and durability. The volumetric amount of the components and the composition of the bond allow adjust the properties of the grinding wheel. The grinding wheel is a composite material consisting of two ceramic components. One of the most common types of grinding wheel material is vitrified alumina, which is known for its high strength, corrosion resistance, stiffness and wear resistance [86]. However, vitrified alumina is also a brittle material, meaning it can fracture easily under stress, impacting the wheel's lifespan and grinding performance. Furthermore, the vitreous bond exhibits an amorphous structure, displaying a non-ductile behavior until fracture. Additionally, the grinding wheel contains a volume of pores that reduces its overall strength. In this context, it will assume that the grinding wheel is a brittle material and investigate its behavior.

Brittle materials are materials that are characterized by their low ductility and high yield strength [87]. This means that they are prone to fracture without significant deformation and have a low resistance to deformation. This is due to that the fundamental properties of brittle materials are determined by their microstructure which are characterized by a lack of dislocations. The mechanical behavior of brittle materials is characterized by the application of tensile stress, which leads to elastic deformation and brittle failure (see Figure 24). Despite their brittle nature, brittle materials have a number of important applications in a variety of fields, including construction, engineering, and manufacturing. They are often used in situations where high strength and low weight are important, such as in the construction of airplanes and other vehicles. However, one of the disadvantages of using brittle materials is their tendency to fracture under high stress.

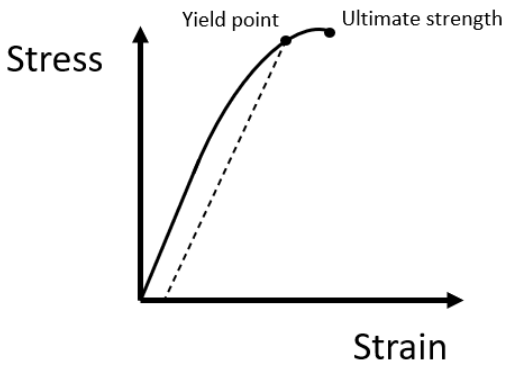

Figure 24. Stress vs strain in brittle material

The Young's modulus (*E*), Poisson's coefficient (*ν*), stiffness modulus (*K*), and shear modulus (*G*) are parameters that define the elastic properties of ceramic materials. These parameters are related to each other through the following equations:

$$\nu = \frac{E}{2G} - 1 \tag{13}$$

According to Griffith's theory, the presence of structural defects such as pores or microcracks in brittle materials plays a crucial role in determining their strength [88]. These defects act as stress concentrators, causing localized stress intensification and promoting crack propagation. Brittle materials are generally stronger under compressive loading conditions compared to tensile loading. This is because compressive forces tend to close and compress the existing defects, reducing their effect on the material's overall strength. As a result, brittle materials can withstand higher compressive stresses before failure occurs. In contrast, when subjected to tensile stress, the existing defects act as initiation points for cracks, leading to a more rapid propagation and eventual failure of the material. This lower resistance to tensile stress is a characteristic feature of brittle materials. It is worth noting that the magnitude of the difference in strength between compression and tension can vary depending on factors such as the specific material composition, microstructure, and the size and distribution of defects within the material.

The brittle materials have a number of important applications in various fields, including grinding process. An example of this is the vitrified alumina grinding wheel. Vitrified alumina grinding wheels are assumed as brittle because they are made from a mixture of aluminum oxide and clay that is fired at high temperatures to produce a hard and dense material. The high firing temperatures cause the aluminum oxide and clay to fuse together and form a solid, glassy structure. Additionally, the microscopic structure of vitrified grinding wheels is inherently porous, which can lead to the formation of cracks and weaknesses that further contribute to its brittleness. Therefore, the vitrified alumina grinding wheels is a hard and dense material due to the high firing temperatures and it is brittle due to its poor tensile strength and porous structure.

One of the components that makes brittle to the grinding wheel is the aluminum oxide or alumina. It is a ceramic material [86] and it is used to grind ferrous materials at medium cutting speeds. The alumina is obtained from bauxite with a greater or lesser degree of purity. There are several types of alumina which are conventional, pure or semi-pure,

ceramic or sintered (SG) and monocrystalline. Conventional alumina is probably the most important abrasive since it represents approximately 90% of grinding applications. It is generally used in materials of high tensile strength, including all ferrous materials [89]. This corundum has high toughness and it is ideal for roughing of non-hardened and heat-treated steels, wrought iron, cast steel gray cast iron and malleable cast iron. Pure or semi-pure alumina is another type of alumina which depends on its degree of hardness, the semi-pure being 97% pure. According to its purity is its application, since increasing purity increases hardness and fragility.

Another component that makes the grinding wheel brittle is the vitreous bond. Vitrified super abrasive technology is the fastest growing field in the precision grinding market. The vitrified bond can better transport the cooling lubricant and the porosity can effectively remove chips. Commercial vitreous bonds are commonly composed of Na_2O - K_2O - Al_2O_3 -B2O3 - SiO2 [47]with a low coefficient of thermal expansion and high fracture resistance. The importance of vitreous bonding materials is obvious at the sight of the large number of recent publications (for instance [44]–[46], [90], amongst many others). However, there are limited studies specifically focused on the mechanical properties of vitreous bond investigated in isolation of grinding wheel. This is primarily due to the inherent characteristics of the material, such as its brittleness, as well as the diverse composition of its components, which can vary between different manufacturers.

The brittleness of vitreous bond poses challenges in conducting mechanical testing, as the material is prone to fracture under stress. Moreover, the specific composition of vitreous bond, can vary as it is often formulated as a proprietary mixture. This further complicates the understanding and characterization of its mechanical properties.

As a result, the available research on the mechanical properties of vitreous bond often focuses on its behavior within the context of grinding wheel systems rather than as an isolated material. Studies tend to examine the overall performance of grinding wheels, including factors such as wear resistance, fracture toughness, and grinding efficiency. These investigations consider the combined effects of vitreous bond, abrasive particles, and pores.

Overall, the grinding wheel is composed of abrasive grains ($\boldsymbol{V_g}$), bonding ($\boldsymbol{V_b}$) and pores ($\boldsymbol{V_p}$), therefore, the grinding wheel is considered as a three-phase system, since each

component occupies a given volume. The proportion of each one of these three phases determines the mechanic characteristics and behavior of the grinding wheel for a specific application. The sum of all its elements is one. For example, a grinding wheel used for high-precision surface grinding may have a different composition than a grinding wheel used for rough conditions. The effects of the variations of each of the components of the grinding wheel can be seen in Figure 25. Furthermore, the composition can be represented in the form of an equilateral triangle, as shown in figure YY [91].

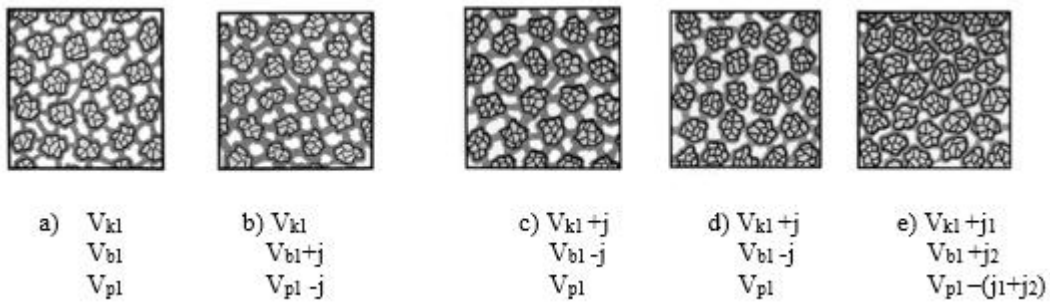

Figure 25. Effect of the variation of the volume of the three components on the structure grinding wheel [91].

The structure of the grinding wheel is crucial for material removal, chip evacuation, and cooling during the grinding process. As shown in Figure 26, the equilateral triangle graph offers an overview of the possible choices. The exact place of the equilateral triangle depends on the application. For instance, large porosity in the wheel is related to normally to large removal and rate, because you have space between the grits and every grain engaged more material. However, on the left of the triangle you have very compact of the wheel which is for precision application. Finally, the size and shape of the pores depend on abrasive grit size and shape.

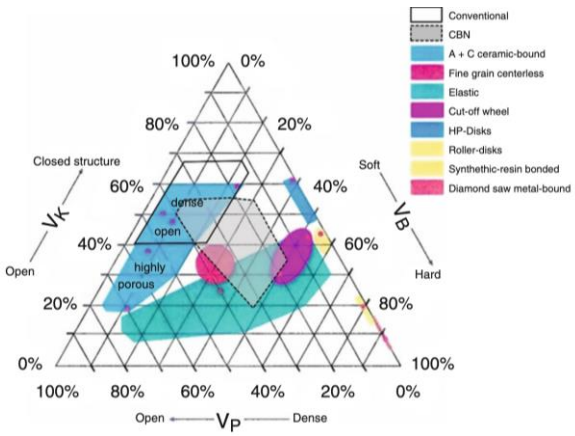

Figure 26. Equilateral triangle of the composition of the grinding wheels [92].

According to Gómez and Sánchez [42], the structure and hardness of the grinding wheel are important factors that define bond fracture. A harder grade of grinding wheel corresponds to easier grinding, as the bond will prevent the wheel from releasing the grains before they are consumed. The porosity of the binder and its high porosity define the thickness of the binder, which can cause premature failure of the grinding wheel. Although the adhesion between the abrasive grains and the binder also influences bond fracture, experiments did not show that this phenomenon occurred.

In the contact zone of grinding, both the workpiece and the grinding wheel are exposed to high temperatures and pressure. The material properties and the stresses and strains to which they are subjected during the grinding process determine the mechanical behavior of a grinding wheel. The mechanical behavior of a grinding wheel can be described by its stiffness, which is a measure of its resistance to deformation under load. The stiffness of a grinding wheel is determined by its material properties, such as its elastic modulus, and by the geometry of the wheel. In addition, the mechanical behavior of a grinding wheel is influenced by its temperature. High temperatures can cause the grinding wheel to become softer and more prone to deformation. For the case of the vitrified alumina grinding wheel, they possess a robust and stiff elastic property, making them well-suited for tasks requiring precise grinding [93]. This high elastic modulus provides stability, allowing for accurate and consistent grinding results. The strength of the vitrified bond in holding abrasive grains together is relatively high, while the process of dressing is relatively easy [94]. These characteristics make them a popular choice in grinding process.

During the grinding process, the grinding wheel is subjected to a number of different stresses and strains, including normal stress (compression and tension), shear stress, and torsional stress. These stresses and strains can cause the grinding wheel to deform, which can affect its performance and lead to wear. Furthermore, the combination of mechanical and thermal cyclic stresses can result in fatigue within the vitrified bond [95]. The cracks of fatigue commonly appear in the impurities, boundaries, different in hardness and so on.

In order to optimize the performance of a grinding wheel, it is important to consider its mechanical behavior and the stresses and strains that it is subjected during the grinding process. This can help to ensure that the grinding wheel is able to withstand the demands of the grinding process and maintain its performance over time.

To continue the discussion of optimizing the performance of a grinding wheel, it is important to examine the mechanical properties of the wheel material and how they affect the behavior of the bond bridges during grinding. To further elaborate, having a strong understanding of the mechanical properties of the wheel material is crucial in creating reliable models that can predict the behavior of bond bridges during grinding. These properties, such as the elastic modulus and ultimate strength, can be determined through various testing methods, such as three-point and four-point bending tests, as well as Brazilian and compression tests (see in Figure 27) [96]. This knowledge is essential in conducting stress analysis of the vitrified binder during grinding, as it serves as input for a discontinuous-hypothesis-based approach, which is the foundation for a discrete element model of the grinding wheel. This model provides a more in-depth understanding of the grinding process and will be explored further later on.

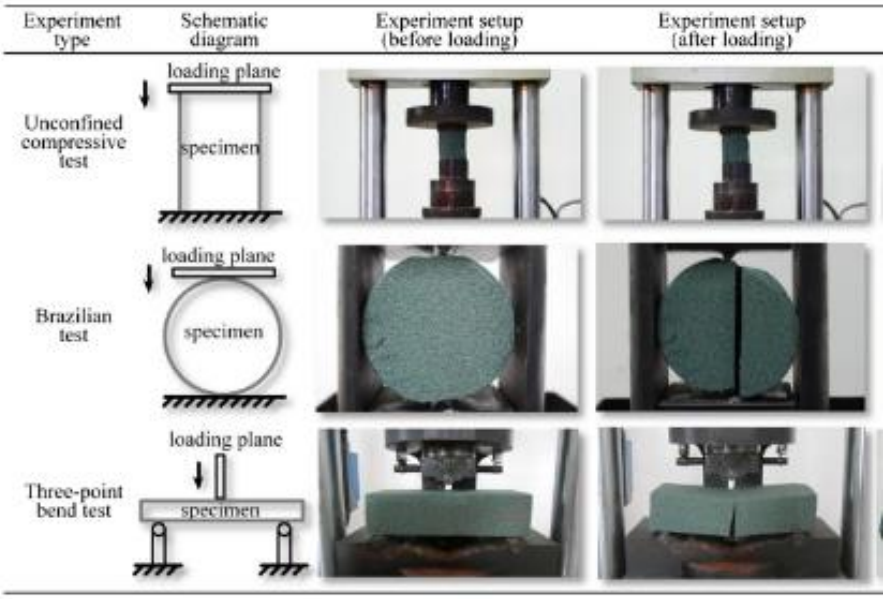

Figure 27. Schematic and experiment setup for compressive, Brazilian and three-point bending test [96].

The literature suggests that the performance of a grinding wheel is largely influenced by its composition and the method used in its production. However, obtaining specific information on the vitreous bonding systems employed in the industry can be challenging due to intellectual property restrictions. Alumino-borosilicate and alumino-alkali silicate systems are known to be widely used in grinding wheels [74]. These systems are created by adjusting the proportions of Al2O3, B2O3, SiO2, and alkali oxides. Additionally, the inclusion of alkaline-earth oxides can alter other physical and chemical properties of the

bond. Recent research indicates that incorporating nanomaterials, such as SiO2 and CeO2 nanoparticles, can enhance the performance of the vitrified bonds utilized in CBN wheels. This is achieved by refining the grain of the bond and increasing its flexural strength and toughness [43], [97], [98]. The presence of nanoparticles can also alter the normal pattern of intergranular cracks that occur in conventional vitreous bonds, leading to a shift towards a transgranular mode of fracture and increasing the bond's bending strength and fracture toughness.

The mechanical and thermal properties of grinding wheels are usually evaluated based on their composite structure. Assessing the mechanical properties of the wheel may involve testing samples that have undergone molding and firing similar to the manufacturing process. The use methods such as three-point and four-point bending tests, as well as Brazilian and compression tests to measure ultimate tensile strength [96]. Sonic testing is a non-destructive testing (NDT) and it is a commonly utilized method to determine the elastic modulus of the wheel in the industry. As for fracture behavior, the most frequently used parameters for brittle, porous materials are the fracture strength and the Weibull modulus [99], [100]. There is limited information available on the thermal properties of grinding wheels and the values found in literature can vary significantly. For instance, a study of the thermal conductivity of CBN grits [101] discovered values ranging from 87W/mK to 1300W/mK. Data on the thermal conductivity of the vitreous bonds used in grinding wheels is particularly scarce, with the only reported value of 2.85W/mK found in a paper by Takazawa [102]. This value is consistent with other data published in literature on other alumino-alkalisilicate ceramic systems [103]. Based on the available literature, it seems that there are still pressing questions regarding the thermal-mechanical behavior of vitrified bonds and the causes of bond fracture that need further investigation.

It is widely recognized that high temperatures, sudden changes in temperature (thermal shock), and repetitive fluctuations in temperature (thermal cycling) can have a negative impact on the structure of a grinding wheel. However, there has been limited research conducted on the specific impacts that these variables have on grinding wheels with vitreous bonds.

Several studies have investigated the effects of high temperatures on vitrified bond properties. Quang et al. [104] have demonstrated that the bond strength can be affected by

high temperatures. As shown in the Figure 28, in the 4 samples, there is a slight increase in strength at the beginning of the tests, followed by a decrease in strength. Moreover, the properties of the vitrified bond such as the thermal expansion coefficient, flow ability [105], wettability [106] and bond hardness [107] can be improved, adding certain materials. For example, Guo et al [108], conducted research focusing on the thermal expansion coefficient of vitrified bonds. Their findings revealed that by increasing the Bi_2O_3 content, the thermal expansion coefficient of the bonds can be reduced.

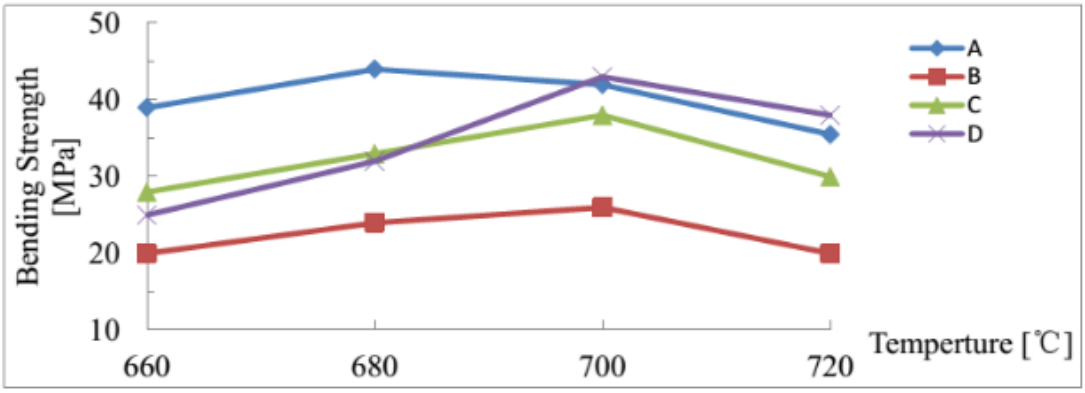

Figure 28. The bending strength curve of vitrified bond CBN composites with varying sintering temperatures [104]

The Brazilian Test is a simple indirect testing method for assessing the maximum strength of brittle materials. This method involves applying a compressive force to a disk-shaped sample using a curved support block. Bahaaddini et al [109] showed that the shape of the sample and the area of contact can affect both the stress values and distribution within the disk as well as the mode of failure during the Brazilian Test. They changed the angle of contact loading from 1° to 30° and found that the most reliable results are obtained with angles greater than 30°. Zhang et al [110] conducted an experimental study of the tensile stress in a modified Brazilian Test on nuclear graphite, also changing the contact angle up to 30°, and noted that cracks initiate in the contact area. To address this issue, Ayallatollahi et al [111] examined the impact of V-notched polycrystalline graphite specimens on crack initiation, varying the size and angle of the notch. They obtained both theoretical and experimental results for a combination of fracture modes I and II and showed how the notched angle affects crack initiation. These studies emphasize the significance of considering the test set-up and sample geometry in order to produce reliable results when conducting Brazilian Tests.

Another experimental characterization technique is fracture toughness testing. Toughness is defined as the ability of a material to absorb energy before fracturing. This experimental technique is used to measure the resistance of a material to cracking and breaking under stress. Sarno and Tomazawa [112] determine the fracture toughness (K_{IC}) of zirconia-lithium aluminosilicate glass-ceramic using hardness identation method. This method allows to get K_{IC}. With this method, Herman and Krzos [47] obtained K_{IC} values of glass-crystalline bond up to 3 times higher than conventional glass bonds.

Another technique used to characterize the mechanical behavior of vitreous bond is the three-point (see Figure 29) and four-point bending test, as described in ASTM C78 and ASTM C293 standards, respectively. These tests aim to determine the flexural strength of beams made from the vitreous bond material. In these tests, the load is applied through either three or four points on the beam.

The flexural strength of the vitreous bond can be obtained from these tests by measuring the maximum applied load (P), the span between the lower supports (L), and the thickness (h) and width (b) of the beam. The flexural strength can be calculated using the following equation:

$$\boldsymbol{\sigma = \frac{3PL}{2Bh^2}} \quad (14)$$

By conducting the three-point or four-point bending tests and applying this equation, valuable information regarding the flexural behavior and strength of vitreous bond can be obtained.

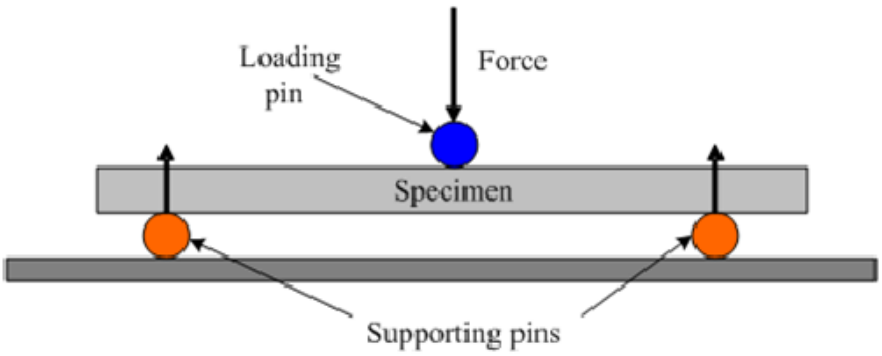

Figure 29. Three-points bending test [113]

The characterization of a material's mechanical behavior requires a comprehensive understanding of not just its maximum strength, but also its crack initiation and propagation

under applied forces. The Digital Image Correlation (DIC) method has been utilized to study the progression of cracks in the fracture zone [114], [115]. DIC analysis offers in-depth insights into the behavior of cracks at the crack tip and enables a connection between the applied load, crack length, and propagation rate as shown in Figure 30.

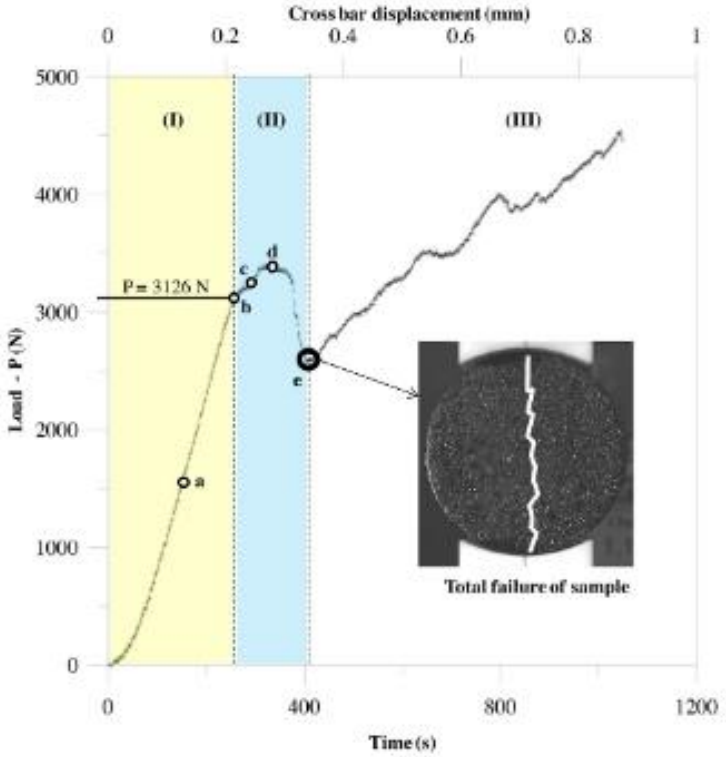

Figure 30. Force vs displacement during Brazilian experimental test [115].

Furthermore, when evaluating the grinding process, it is crucial to consider not just the properties of the material but also the forces acting on the grinding wheel and the loads transmitted to the binder. Previous research has acknowledged the significance of stress distribution in the binder and its effect on the elasticity and deformation of the grinding Wheel [116], [117]. A probabilistic model based on the idea of undeformed chip thickness is proposed by Hecker [118]. Other studies have demonstrated the complex nature of the contact between abrasive grains and the workpiece, which involves a continuous change in the friction coefficient and local contact stiffness [119]. Wang et al [120] developed a model that describes the forces and energy partition based on the various types of contact between the grit and the workpiece, providing a qualitative understanding of the loads on the binder. However, there is limited information available on the relationship between the mechanical properties of the binder and the volumetric wear of the wheel.

2.6 Simulation and modelling of the grinding wheels performance

In recent years, the importance of modeling and simulating grinding processes has greatly increased due to the industrial demand. This demand can be evidenced by the growing number of publications and research in this field. Simulation and modeling techniques are excellent tools used to predict, understand and optimize the performance of grinding wheels [121]. These techniques (see Figure 31) allow engineers to simulate the grinding process and understand the factors that influence the performance of the grinding wheel, such as abrasive particles, bond material, wheel geometry, wheel structure, thermal damage, surface topography and the grinding parameters. In the past, basic models using physical-analytical and physical-empirical methods based on multiple linear regression are used. Nowadays, thanks to the advancements in technology, high-performance computers allow the use of more advanced and accurate models and simulation methods.

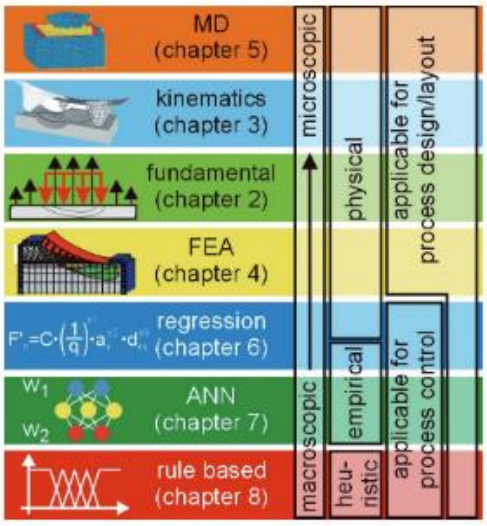

Figure 31. Models and their applications areas for simulation [121].

In order to develop an accurate model for addressing the volumetric wear of grinding wheels, several crucial aspects need to be considered. The aspects that play a significant role in the modeling process and contribute to a comprehensive understanding of the wheel's performance are the following:

- The characteristics of the grinding wheel surface have a profound impact on its overall performance. Factors such as the topography of the wheel, the distribution and shape of abrasive grains, and the porosity of the wheel surface are critical in determining the wear patterns that will occur during the grinding process.

- The forces exerted on the grinding wheel during grinding operations directly influence its wear behavior. These forces include the grinding forces, such as normal forces and tangential forces. Understanding and accurately modeling these forces is essential for predicting the wear characteristics of the wheel.
- The mechanical response of the grinding wheel material to the applied forces is another crucial aspect to consider. Material properties, such as hardness, strength, and elasticity, significantly affect the wheel's wear resistance and deformation characteristics. Incorporating these material properties into the model enables a more realistic representation of the wheel's performance.
- Wear is a fundamental aspect that must be considered in the modeling of grinding wheel performance. The volumetric wear of the wheel can be influenced by various factors, including the type of abrasive used, the grinding parameters employed, the cooling conditions during grinding, and the properties of the workpiece material. Taking these factors into account allows for a more accurate prediction of the wheel's wear behavior.

By carefully considering and incorporating these aspects into the modeling process, an effective and reliable model for the volumetric wear of grinding wheels can be developed. Several models have been developed that take into account these important aspects.

2.6.1 Grinding wheels surface modelling

A thorough comprehension of the interaction between the wheel and workpiece in grinding can be derived from a detailed analysis of the surface of the grinding wheels. It is known that the surface of the grinding wheel comprises the porosity volume, the density and the protrusion height of abrasive grains. In the past, the surface of the grinding wheel is evaluated through empirical measurements and real photographs. However, nowadays, various models have been developed to analyze the surface topography of grinding wheels under different grinding conditions. One approach to modeling grinding wheel surfaces involves using advanced computational techniques, such as finite element analysis (FEA) or discrete element modeling (DEM). These methods simulate the behavior of the wheel and the grinding process, allowing for a more accurate prediction of the wheel's performance and the quality of the ground surface.

Doman et al. [122] divided their research into three distinct sections: 1D, 2D, and 3D. The 1D section focused on characterizing surface conditions using a single parameter. However, this approach did not provide sufficient detailed information about the surface conditions. In contrast, the 2D section took a physical perspective, considering the impact of the structural components of the grinding wheel such as the size and shape of the abrasive grains (see Figure 32), and dressing mechanics. Additionally, the section accounted for grain fracture and deformation, providing a more comprehensive understanding of the surface conditions. In the 3D modeling section, Doman et al. considered the arrangement of grains on the dressed wheel surface. By incorporating this element into their model, they are able to further enhance the accuracy and precision of their predictions. In addition, the stochastic treatment and arrangement of grains proposed by Chen and Rowe [123] align well with the structure of the grinding wheel, making it a highly suitable approach.

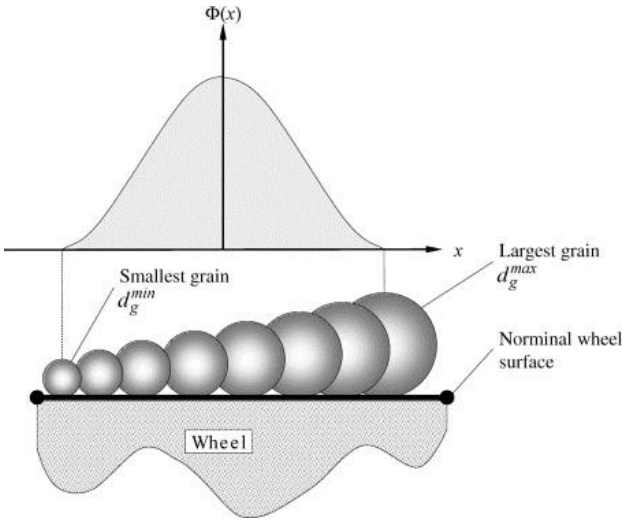

Figure 32. Normal distribution of the grain size [122]

Sridhar et al. [124] developed a surface topography model using a DEM software that takes into account the dressing process, as well as the effects of the manufacturing process and the influence of grinding wheel properties. However, one of the main limitations of this model is that the DEM generates elements that are completely spherical, which does not accurately reflect the shape of the grains. Additionally, the DEM does not separately consider the abrasive grain and the bond. Finally, the model's results are verified with the experimental test.

In some models, the shape and the position of the grain have been considered to create the surface topography of grinding wheels. Kacalak et al. [125] have developed three different methods for generating surface topography of the grinding wheel. In order to create the topography, they consider the shape and position of the highest vertices and compare them with the actual surface of the grinding wheel. The distribution, density, and position of the vertices are highly relevant for generating the topography. Finally, there is a high level of agreement between all three models and the actual surface of the grinding wheel. In another approach, Brakhage et al. [126] developed a grinding wheel structure model based on the actual shape of the abrasive grains. In this article, they evaluated the shape of the grains using tomography and visualized the volumetric structure of the wheel. The goal is to determine the grain density of the wheel. However, the model did not take into account the bonding material and pores, which are important for generating a realistic structure of the grinding wheel. In the third approach, Zhang et al. [127] simulated the actual topography of the grinding wheel using finite element method (FEM), considering hexahedral grains randomly positioned across the entire surface of the wheel. In this article, they obtained the grinding forces, whose results have an effect on the deformation of the wheel. Finally, De Pellegrin and Stachowiak [128] analyze the shape and scale of abrasive grains using an analysis technique. In this article, the shape of the grains is an important factor in surface wear due to the penetration they exert on the workpiece.

Unlike other models for grinding wheel simulation, Zhang et al. [129] consider the volume of the wheel's porous factors. In other words, in addition to taking into account the shape and distribution of abrasive grains on the wheel, they also consider the distribution of porosity. This makes the grinding wheel model more realistic than other models.

Since the grinding process is inherently stochastic in nature, on the one hand, Zhen and Ranga [130] developed an analytical model that considers the intrinsic stochastic process of grinding. This means that they use probability statistics to take into account the geometry and quantity of abrasive grains that pass through the contact between the grinding wheel and workpiece. In this article, they analyze the finishing and cut-off operations, taking into account parameters such as the number of grains in contact, the number of grains cutting, their dimensions, as well as the penetration of the grains and the chip removed (see in Figure 33). The aim is to compare these results with experimental data. The results showed that a very low number of grains participate in cutting, which also depends on their size.

Conversely, a high number of grains participate in rubbing or plowing. On the other hand, Koshy et al.[131] present a stochastic simulation, utilizing 3D topography, regarding the structure of resin/metal bonded diamond grinding wheels. In this study, the authors take into consideration the protrusion and density of grains, as well as the spacing between them and the percentage of exposed abrasive grains. By doing so, they are able to evaluate the effectiveness of the dressing operation on the diamond wheel's topography. In this approach, Agarwal and Rao [132] have developed an analytical model for surface roughness based on the stochastic nature of the grinding process, which considers the geometry and random distribution of abrasive grains. The results obtained show excellent agreement with experimental data. Finally, Warnecke and Zitt [133] describe a 3D model of a grinding wheel in both macro and micro geometries, with an array of multiple grains on its surface.

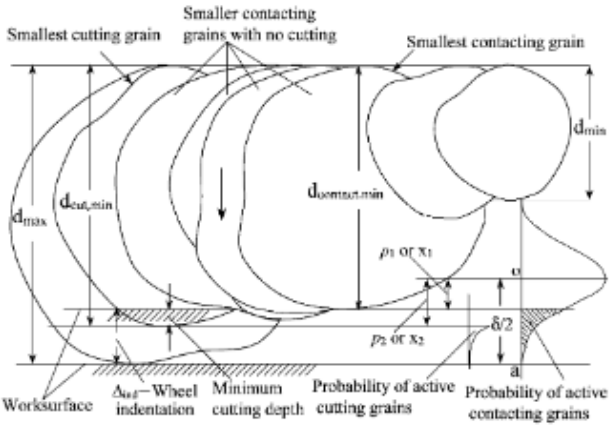

Figure 33. Schematic of active contact grains, active cutting grains and the penetration into the workpiece [130].

Chen and Rowe [123] provide a comprehensive analysis and simulation of the grinding process, focusing on the generation of wheel topography through single point diamond dressing. One of the key challenges in this process is the random spacing of grains throughout the wheel. To address this, the simulation considers various factors, including grain size, spacing, fracture, break-out, and the movement of the dressing tool. The simulation results demonstrate excellent qualitative agreement with experimental results. As such, this method enables the simulation of the wheel surface with a high degree of accuracy.

The investigation of the trajectory of grains is crucial because it impacts both the surface finish of the workpiece and the wear of the grinding wheel. For this reason, Chakrabarti

and Paul [134] have created a numerical model of an abrasive wheel with square pyramidal abrasive grains. By simulating the trajectory of all abrasive grains, the model generates the ground workpiece surface by removing material. This model is developed to study the effects of grinding parameters on the surface of the wheel. The results presented in the article are consistent with experimental results published in the literature. In addition, Cao et al [135] develop a numerical model that enables the prediction of surface topography and improves surface quality. In this article, the trajectory of grains and vibrations between the grinding wheel and workpiece are considered.

2.6.2 Grinding forces modelling

Several models have been developed to predict grinding forces, most of which are analytical models. These models include micro and macro grinding force models, as well as plowing grinding force models [136]. Accurate modeling of grinding forces is crucial for improving grinding parameters and the overall grinding process. On the one hand, Badger and Torrance [137]developed two models aimed at predicting the grinding forces produced by rigid plastic contact with the surface of a grinding wheel. One model is 2D and it is based on the lane-strain slip-line field theory, while the other is 3D and it is based on a pyramid-shaped asperity model. In both models, the behavior of the contact is dependent on the abrasive grains and the coefficient of friction. In this research, take into account the breakage of the bond regarding to the maximum stress. Finally, the forces obtained from both models are compared with experimental results, and the more accurate predictions are obtained with the 3D model. On the other hand, a model for single point diamond dressing of grinding wheels developed by Torrence and Badger [138], not only predicts the grinding forces but also the workpiece roughness and topography of the diamond-dressed wheel. This model incorporates stochastic characteristics related to the breakage of bonds and grains, as well as the arrangement of abrasive grains and their interaction with the dressing tool.

In another case study, Hecker et al. [139] analyzed the topography of the grinding wheel to determine its characteristics, such as grain size and density. Using this information, they are able to model the normal and tangential forces acting on each abrasive grain, taking

into account the kinematic effects generated by the active grains and their deflection during contact. The grinding force results obtained are validated through experimental tests.

Inasaki [140] developed a surface model for grinding wheels with the goal of predicting roughness and grinding force. This model takes the chip removal process into consideration. The results indicate that the cutting force can predict changes in topography to a certain extent.

2.6.3 Grinding wheels mechanical behavior modelling

The mechanical behavior of the grinding wheel can be determined through various methods, and one of them is the use of numerical methods. In particular, Discrete Element Method (DEM), are useful tools for studying the mechanical behavior of porous brittle materials. DEM has been used to simulate Brazilian and triaxial tests on geomaterials and concrete [141]. Li et al. [96] used DEM to analyze the loads on the binder in vitrified grinding wheels. Their model is based on the discontinuum hypothesis and considers different grit geometries and discretization of both abrasive and vitreous bond. Due to the high computational cost, the model is limited to the contact region between the wheel and the workpiece. Figure 34 shows the configuration of the grinding simulation. The grinding wheel material is characterized using Brazilian tests, and the model is validated through grinding tests that measure grinding forces and final part topography. While this research does not consider volumetric wear and the G ratio, it provides a foundation for the efficient characterization and simulation of the behavior of vitreous bonds. Li et al. [142] extended their research in a subsequent paper.

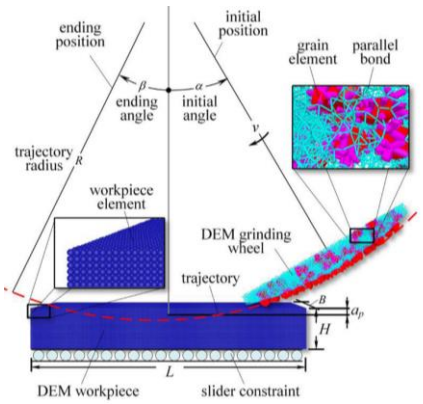

Figure 34. Configuration of the grinding simulation [96]

Osa et al. [143] used a model based on the hypothesis of a discontinuous body, in which abrasive grains are represented as discrete elements and the binder is represented as elastic beams as shown in Figure 35. The use of spheres to approximate the complex geometry of grains and beams to represent the binder greatly reduces computational cost. The model calculates the stress distribution on the binder and the elastic deformations caused by grinding forces. It is validated through calculations of the contact length and comparisons with existing references. The model shows that the active number of grains has a large influence on the contact stiffness and, therefore, the stresses on the binder, and that different dressing strategies can highlight this. While the model does not consider the fracture of bond bridges or the prediction of the G ratio, DEM has been shown to be effective in describing fracture mechanics in tribological studies [144].

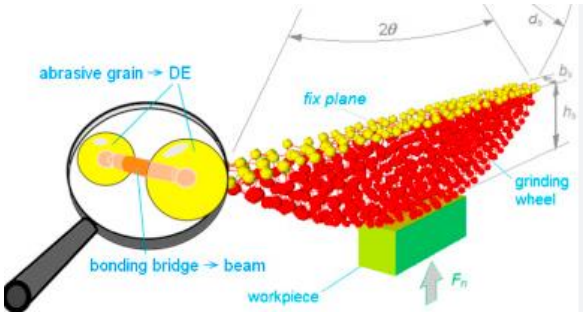

Figure 35. Schematic representation of the grinding wheel model [143]

2.6.4 Grinding wheels wear modelling

Currently, there is a lack of theoretical models available to analyze the volumetric wear of vitrified grinding wheels. However, researchers have developed experimental models to determine the life expectancy of other types of grinding wheels. For example, Yu et al. [62] have created a model to assess the life expectancy of electroplated CBN grinding wheels when machining nickel-based superalloys. In their study, they analyzed the evolution of the surface topography of the grinding wheel and the wear mechanisms, observing the bond fracture phenomenon in the initial wear phase followed by steady grit wear in the second phase. To develop their model, process parameters, thermal loading, and the Paris-damage evolution law are required for the first stage. For the second stage, knowledge of the material abrasion evolution law (Preston approach) is necessary. Additionally, they

developed a single grit pull-out device to analyze changes in residual strength at CBN wheels during contact.

Another study by Novoselov et al. [145] analyzed the relationship between the wear of the grinding wheel and the wear of the abrasive grain analytically. They performed a kinematic analysis, yielding a differential equation that relates the wear of the grinding wheel to the wear of the abrasive grain. Furthermore, they used a probabilistic approach to estimate the actual condition and wear of the grinding wheel.

Hwang et al. [146] developed a statistical model to determine the surface topography of a grinding wheel during the grinding process, taking into account the attritious wear and active grains, which have a pyramidal shape. The results showed that as the grinding progresses, the number of active grains and the attritious wear increase, leading to an increase in the grinding forces. They also obtained a relationship between the grinding forces and the attritious wear area.

Godino et al. [147] used discrete element methods to model the grain wear of Sol Gel alumina and white fused alumina, taking into account the third body generated during the contact between the workpiece and abrasive grain. They also considered the influence of the crystal structure and analyzed the thermal behavior of SG alumina. Finally, they compared their numerical and experimental results, revealing errors of 8% and 15% in WFA and SG alumina grain, respectively.

In summary, developing a model for volumetric wear requires consideration of several crucial aspects, including the surface of the grinding wheel with a focus on the penetration of abrasive grains, grinding forces, and the mechanical behavior of the wheel.

2.7 Preliminary conclusions

Based on the review of the state of art on the grinding process to characterize the bond fracture of grinding wheels, several key findings and conclusions can be drawn:

- The review has highlighted the main wear mechanisms of grinding wheels in the grinding process. It is observed that the specific wear mechanisms vary depending on the combination of the grinding wheel and the workpiece material. However, in some

cases, the wear mechanisms can overlap, making it challenging to analyze each mechanism individually. In particular, the phenomenon of bond fracture stands out as the predominant wear mechanism, leading to imbalances and rapid wear, which can result in vibrations and negatively impact the final dimensions of the workpiece. Additionally, this phenomenon, along with grain breakage is produced with high Q_w' and contributes to the reduction of attritious wear. Finally, it has been observed that reducing the hardness of the grinding wheel leads to a higher occurrence of bond fracture and a lower occurrence of grain fracture. Therefore, in the present work, special attention will be given to isolating and addressing the bond fracture phenomenon separately from other types of wear.

- Characterizing the phenomenon of bond fracture in vitrified alumina grinding wheels is crucial, as they are commonly grinding wheel used in various industries. Therefore, this study aims to investigate the evolution of bond fracture on vitrified alumina grinding wheels. Furthermore, among the various methodologies analyzed for quantifying bond fracture, the measurement of the ground graphite material will be employed. Grinding on graphite offers information into the actual radial wear of the grinding wheel during the grinding process. By examining the bond fracture phenomenon and using the graphite material as a means of measurement, a comprehensive understanding of the behavior and progression of bond fracture in alumina grinding wheels can be achieved.

- The theory of brittle fracture for vitreous bonding is valid. The occurrence of fractures at bridges and the interface between the abrasive grit and the vitreous material has been consistently observed. Moreover, the correlation between the dressing operation and the presence of microcracks underscores the significant role of these microcracks in determining bond integrity. The review also emphasizes the susceptibility of vitreous bonds to crack propagation when subjected to cyclic thermo-mechanical loads during grinding.

- The composition of the vitrified bond has a great influence in the wear characteristics of the grinding wheel. By incorporating intergranular boundaries, the bond composition enhances fracture toughness, leading to microchipping and ultimately reducing volumetric wear. In addition, the development of new formulations for ceramic bonds

establishes the improved grinding performance and properties of the grinding wheel through systematic grinding tests.

- The advancement and implementation of theoretical models to understand the behavior of bond bridges in grinding processes necessitate thorough experimental characterization of the mechanical properties of the grinding wheel material. Essential properties, including ultimate strength and elastic modulus, can be accurately assessed using three and four-point bending tests. Additionally, the ultimate strength of the composite body of the grinding wheel can be successfully measured through Brazilian and compression tests. These valuable insights into the mechanical properties serve as crucial input for stress analysis of the vitrified binder during grinding.

- To take into account both the material properties of the grinding wheel and the forces exerted on it, as well as the loads transmitted to the binder is essential. Classical studies have emphasized the importance of stress distribution within the binder, underscoring its impact on the elasticity and deformations of the grinding wheel.

- Numerical methods have emerged as a powerful tool for investigating the mechanical behavior of porous brittle materials, including grinding wheels. Advanced computational techniques such as finite element analysis (FEA) or discrete element modeling (DEM) have proven to be the most effective approaches for modeling grinding wheels. These methods enable the simulation of wheel behavior during the grinding process providing relevant information and more accurate predictions regarding wheel performance and the quality of the resulting ground surface. DEM, in particular, has demonstrated its superiority in reproducing the granular structure of grinding wheels and effectively reflecting bond fracture wear. Existing grinding wheel wear models have emphasized various factors, including grinding parameters, thermal and mechanical loading, wheel elasticity, damage evolution laws, probabilistic approaches, surface topography, and grits penetration. The wear models aim to capture the complex interactions between these factors. Analyzing the contact between grinding wheel and workpiece is crucial for obtaining accurate predictions of radial wear. Therefore, the grinding wheel wear model should adequately account for the stiffness of the grinding wheel and consider the surface topography.

In conclusion, this study aims to address the existing gaps in the current state of the art. Specifically, the focus will be on conducting a comprehensive analysis of bond fracture in vitrified alumina grinding wheels. The occurrence of bond fracture will be thoroughly investigated, taking into account the influence of the grinding parameters and hardness of the grinding wheel. Additionally, a detailed examination of the grinding forces results will be conducted to enhance the understanding of bond fracture generation during contact. Furthermore, three-point bending tests will be performed to determine the failure stress and the grindometer will be used in order to get the elastic modulus of the grinding wheel, providing valuable information into the mechanical properties of the grinding wheel. Subsequently, a grinding wheel wear model will be developed to study the influence of stress in the contact and the evolution of radial wear in vitrified alumina grinding wheels. By addressing these aspects, this research aims to contribute to a deeper understanding of the mechanisms underlying bond fracture in vitrified alumina grinding wheels. The findings will provide relevant knowledge for optimizing grinding processes and improving the durability and performance of such wheels.

Chapter 3

Experimental analysis of volumetric wear of vitrified alumina grinding wheels.

3.1 Introduction

The state-of-the-art review has identified the challenges associated with characterizing volumetric wear during grinding. To overcome these difficulties, this chapter presents an experimental test designed to replicate real-world grinding conditions. Specifically, the primary focus of these experiments is to analyze the bond fracture phenomenon that occurs during grinding. To isolate this phenomenon, a design methodology is employed that replicates real grinding conditions using an extremely soft wheel that develops volumetric wear as the predominant effect. The experiments use 100% monocrystalline structures of alumina, which enable the development of bond fracture. In addition to analyzing the bond fracture phenomenon, several secondary objectives are proposed, including the measurement of the volumetric wear of the grinding wheel and the determination of the

relationship between power, specific energy, forces, and part material removal. Finally, to achieve these objectives, this chapter defines the test conditions, methodology and presents the experimental results. Furthermore, the experimental results provide the input data for the simulations.

3.2 Equipment

Studying a particular type of wear can prove challenging due to its tendency to overlap with other types of wear. However, the present study overcomes this challenge by designing a soft grinding wheel grade EF that prevents attritious wear and grain breakage. The main focus of the study is to create an experimental test that can accurately replicate the bond fracture phenomenon that occurs during grinding against steel, with the aim of characterizing the volumetric wear of the grinding wheel under specific grinding conditions.

Additionally, grinding parameters are chosen, always close the range of industrial parameters, to ensure accurate analysis of bond fracture with grinding wheel and grinding parameters design. Thus, to minimization of the grain fracture, 100% monocrystalline abrasive grain is chosen.

The development of an experimental grinding test for the analysis of volumetric wear necessitates the consideration of grinding test conditions and various elements of the grinding system, which include the grinding machine, the workpiece, the grinding wheel and the dresser. To conduct the tests, the specifications of the grinding machine and dynamometric device used to measure grinding forces during the tests are also provided. The main characteristics of the machine are presented in this section. To ensure the precision of the force measurements, a wattemeter is employed to gauge power output. Table 1 outlines the device name and conditions used for acquiring the grinding forces and power, and it should be noted that the tests are conducted with cooling to maintain optimal grinding conditions. The others elements of the grinding system and the grinding test conditions will be detailed based on their specific characteristics as follows.

To better observe the bond fracture phenomenon in detail, an open structure is chosen for the grinding wheel. This structure consists of 100% cubic monocrystalline alumina

abrasive grains, with a diameter of 0.330 mm, embedded in a vitreous bond matrix. As alumina is commonly used in the grinding industry, it is chosen for this study. This results in an open and soft grinding wheel with the nomenclature MA46EF12V. The grinding wheels have dimensions of 250x40x127 mm (see Figure 36) and are manufactured by UNESA S.L. in Spain.

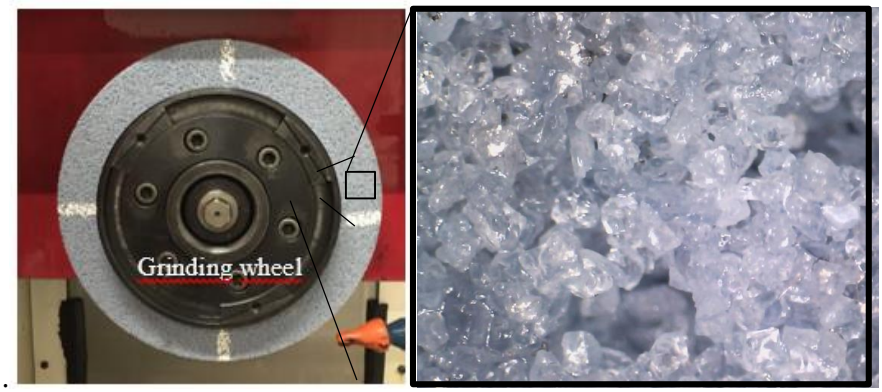

Figure 36. Vitrified alumina grinding wheel 100% monocrystalline

Grinding experiments are conducted with an surface grinding on a three-axis CNC machining center (Blohm Orbit 36), as shown in Figure 37.

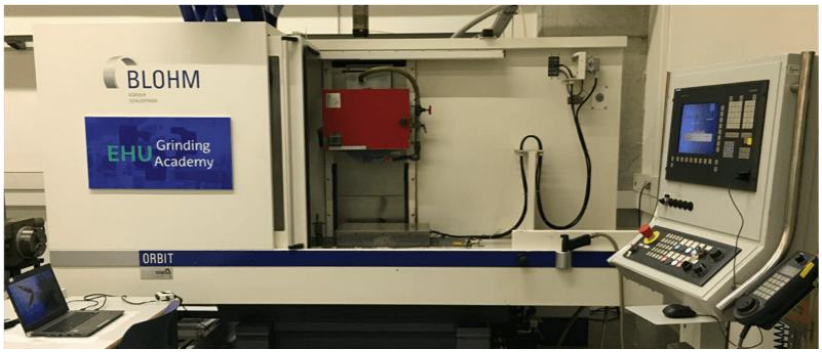

Figure 37. Surface grinding machine Blohm orbit 36

The main characteristics of the surface grinding machine are:

- The maximum power of the machine surface grinding is 8.5 KW.
- Maximum spindle speed is 6500 rpm.
- Maximum work speed is 40000 mm/min.
- Maximum wheel speed is 35 m/s.
- The workpiece camping is a magnetic device

- Static diamond.
- Maximum wheel dimensions: 450 x 50 x 127 mm
- Workspace dimensions: 1000 x 300 mm

For this study an ASTM A681 (DIN 90MnCrV8) hardened tool steel T-profile block is chosen as the workpiece. The workpiece has a hardness of 54HRc and dimensions of 45 x 30 x 125 mm, as shown in Figure 38. This workpiece material is known for its excellent wear resistance due to its high carbon and high chromium composition, making it a suitable candidate for grinding tests.

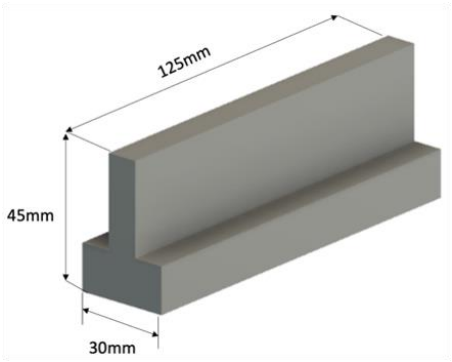

Figure 38. Geometry of the workpiece.

3.3 Monitoring devices

The monitoring devices are used for power measurement, force measurement, volumetric wear measurement and attritious wear quantification (wheel surface analysis) during the grinding. Firstly, this section explains the power and forces measurement during the grinding process. Secondly, once the tests are completed the worn surface analysis is carried out to measure the volumetric wear, the topographic profile wear and confirm that other type of wear, besides bond fracture phenomenon, is observed in relatively low proportion.

3.3.1 Power measurement

To measure the power, a Load Controls UPC-230FR, device connected to an NI 6009-USB data acquisition card is used as shown in Figure 39. Signal collection and processing are

performed using GREAT software, a custom Python-based development tool. A sampling frequency of 10000 Hz is employed to ensure a significant number of measurements. With work speed of 0.25 m/s and workpiece length of 125 mm, 5000 data points are obtained. To eliminate signal noise, a low-pass filter is applied after capturing the power signals. The cutoff frequency of 0.25 Hz is determined based on an analysis of the acquired signals' Fourier transform (see Figure 40).

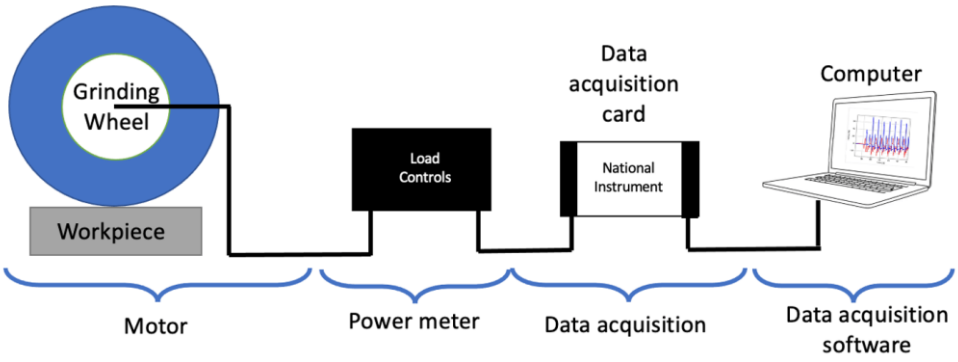

Figure 39. Power measurement during the grinding operation

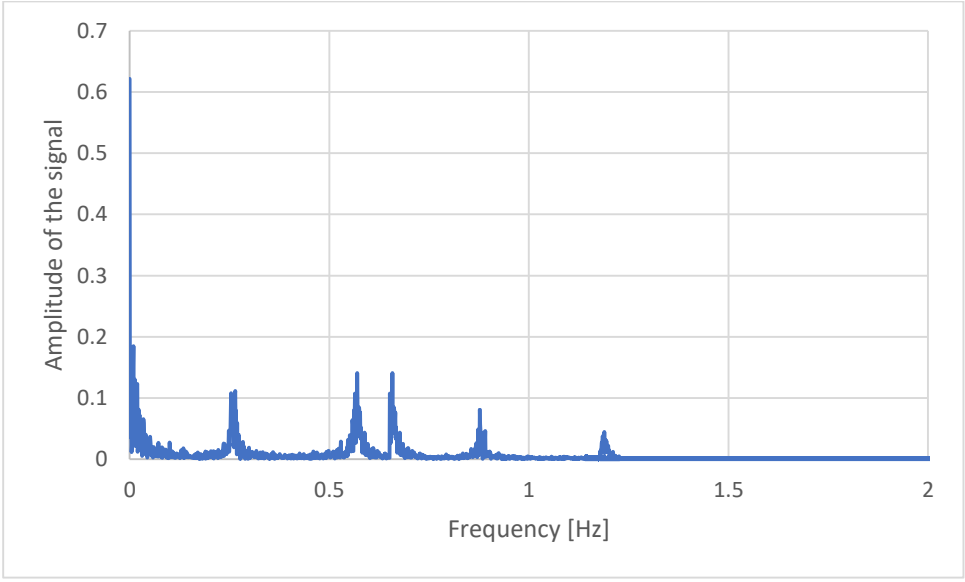

Figure 40. Amplitude vs. frequency analysis of the power signal for determining the cutoff frequency

3.3.2 Force measurement

To measure the grinding forces, a Kistler 9257B table connected to a signal acquisition device from Kistler is used as shown in Figure 41. Signal collection is performed using Dynoware software, with a sampling frequency of 10000 Hz to ensure a significant number of measurements, following the same criteria as the power acquisition. Signal processing and filtering are conducted using GREAT/Matlab software. The processing involves removing drift in the obtained signals and applying filtering. The Fourier transform of the acquired force signals produces similar results to those obtained from the power signals. Therefore, a cutoff frequency of 0.25 Hz is chosen.

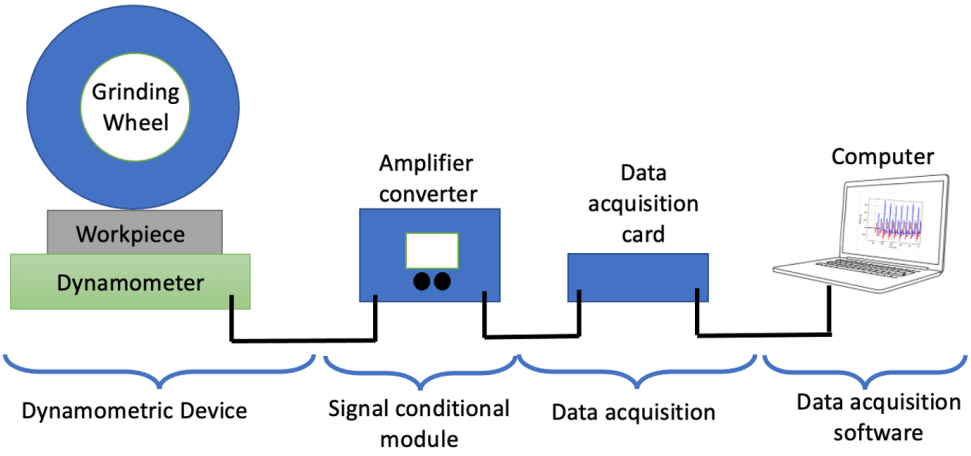

Figure 41. Force measurement during the grinding operation.

3.3.3 Volumetric wear measurement

To measure volumetric wear, the classical method of marked on a graphite piece is employed. In this case, as shown in Figure 42 the width of the workpiece (a) being ground is smaller than that of the grinding wheel width, ensuring that a portion of the wheel remains unworn (b). After a predefined number of grinding passes, a graphite piece (a very soft material) wider than the grinding wheel is ground. The marked left on the graphite piece includes both the worn and unworn areas. Finally, the difference in heights ($H_f - H_i$) measured by the dial gauge indicates the radial wear and consequently the volumetric wear of the grinding wheel.

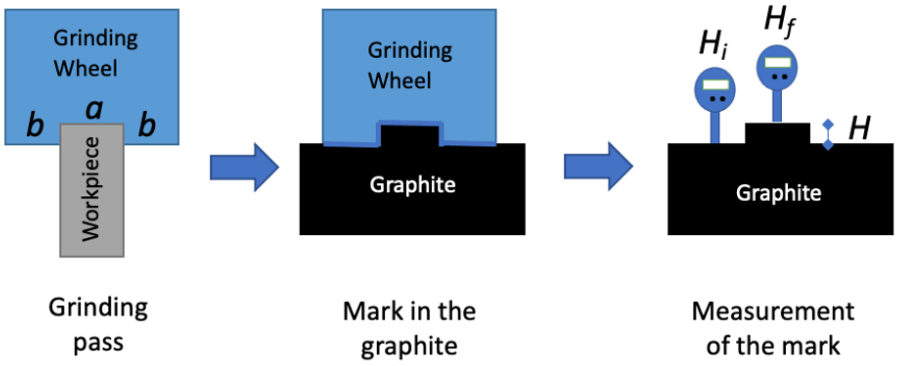

Figure 42. Volumetric wear measurement in the center of the grinding wheel

Additionally, the profile of the wheel wear is analyzed. To measure the profile of the wheel wear, the shape of profile is taken in the graphite piece. In this case, as shown in Figure 43, the topographic profile is taken by the microscope Dino-Lite (Dino-Lite Digital ProX (AM4013)) in the graphite piece. Once the images have been taken, the images processing is performed. The images acquisition software (Dino-lite Capture 2.0) and profile measurement application (Web Plot Digitizer software) are used. Finally, the data are collected in MATLAB.

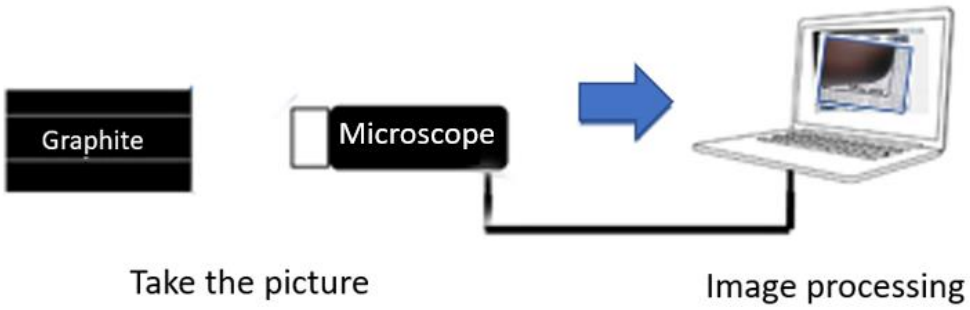

Figure 43. Topographic profile wear measurement in the graphite piece.

3.3.4 Attritious wear measurement

In order to validate that volumetric wear is the dominant factor in the experiment, attritious wear measurements are measured on the surface of the grinding wheel. For this, the capture of images of the topography of the grinding wheel worn is made with the optical microscope at 50x (Dino-Lite Digital ProX (AM4013)) with the light direction oriented perpendicular to the grinding wheel surface as shown in Figure 44. The captured images

are processed using Adobe Photoshop Cs for the identification of attritious wear areas. Furthermore, for providing quantitative measurements of their respective percentages a module called attritious wear analysis is used, which is integrated into the Great software. The detailed results will be presented in section 3.5.5.

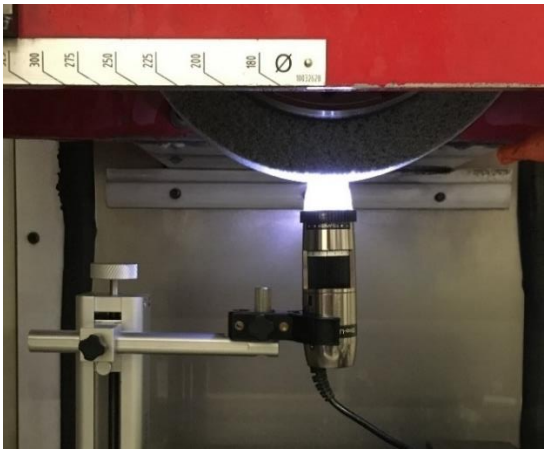

Figure 44. Attritious wear measurement with the optical microscope Dino-Lite with the light direction oriented perpendicular to the wheel surface.

3.4 Methodology

This section provides an explanation of the conditions in which the experimental work is carried out. Initially, the dressing and grinding parameters are set for the entire test, which are documented in Table 1. This encompasses factors such as depth of cut, cutting speed, number of passes and other relevant variables. It can be observed that the initial dressing parameters correspond to medium-level dressing conditions. Power and force measurements are taken for each grinding pass. After the completion of the experimental tests, the analysis of forces and wear are conducted.

3.4.1 Test condition

During the experimental test, grinding forces and power consumption are measured at each grinding pass. The test is divided into 11 blocks to measure the grinding wheel wear and real material removal rates. Table 1 provides the number of passes in each block. Following

each block, the workpiece material removed and wheel profile wear are measured. Table 1 displays the grinding conditions used in the experiment.

Throughout the tests, the cutting speed (v_s) is maintained at a constant value of 30 m/s. The workpiece speed (v_w) is set at 0.25 m/s, and a programmed depth of cut (a_e) of 0.036 mm is applied to investigate its influence on bond fracture occurrence. The working zone is positioned in the middle of the grinding wheel as shown in Figure 45. Table 1 provides the programmed parameters for the 11 tests block, including the specific material removal rate Eq. (15) and the speed ratio Eq. (16). It should be noted that Q'_w overcomes slightly outside the range of conventional grinding for the 11 designed tests block, highlighting the bond fracture phenomenon. However, q_s is set at 120, just at the limit of thermal damage to the workpiece. Additionally, the experimental tests are conducted with a grinding wheel width (b_w) of 10 mm, with the working zone positioned in the middle of the grinding wheel, as illustrated in Figure 45.

$$Q'_w = a_e \cdot v_w \tag{15}$$

$$q_s = \frac{v_w}{v_s} \tag{16}$$

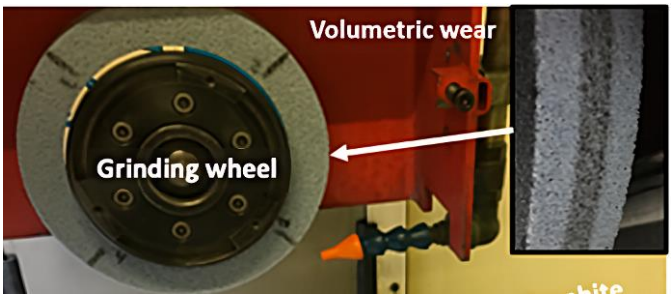

Figure 45. Working zone positioned in the middle of the grinding wheel.

Accumulative grinding tests are performed to investigate the progressive evolution of volumetric wear during the grinding process. Consequently, the grinding wheel is dressed only at the beginning of the tests, providing data for the initial surface. The dressing operation is carried out using the parameters specified in Table 1. It is noteworthy that a fine dressing approach is employed, with an overlap ratio (U_d) of 7.33. Regarding the depth of cut, a value of 0.01 mm will be assigned, and the peripheral speed of the grinding wheel will be the same as that used in the grinding process.

Hence, the initial phase of the grinding tests involves dressing the surface of the wheel, which is done only once throughout the entire test duration. During the complete tests, a total of 1041.46 mm^3/mm of material is removed from the grinding wheel, enabling the subsequent analysis of grinding forces, power consumption, attritious wear, topographic profile wear and the evolution of volumetric wear. It is important to note that the power consumption is measured using the spindle motor of the grinding machine, where the grinding wheel is located, while the grinding forces are obtained through the use of a Dynamometer plate, specifically the Kistler 9257B, which is positioned beneath the workpiece.

In the Figure 46, the setting up of the experimental system is shown. The graphite and the workpiece can be seen. The graphite is placed in a position where there is no collision between the grinding wheel and graphite during the grinding process.

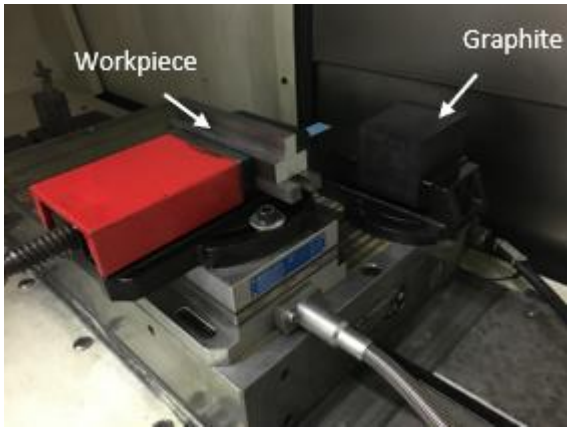

Figure 46. Setting up of the experimental system

Grinding wheel	
Dimensions (mm)	Ø250x127x40 mm
Specification	MA46EF12V489P20P
Workpiece material	
Material	AISI 02 (90MnCrV8)

Hardness (HRc)		54	
Dimensions (mm)		30x10x125 mm	
Grinding conditions			
	a_e = 0.036 mm	v_s = 30 m/s	v_w = 0.25 m/s
	$Q_w' = 12.5\ mm^3/mm{\cdot}s$		$q_s = 120$
Dressing conditions			
	a_{ed} = 0.010 mm	V_d = 250 mm/min	v_s = 30 m/s
		$U_d = 7.33$	
Number of passes	*10*	*20*	*40*
Grinding test block	*1 - 4*	*5 - 8*	*9 - 11*
Force measurements			
Dynamometer plate: Kistler 9257B		Acquisition rate 10000 Hz force range ±500 N Low Pass filter Cut-off frequency: 0.25	
Power measurements			
Wattmeter Load Controls Universal Power Cell: Model UPC-FR		Acquisition rate 10000 Hz Low Pass filter Cut off frequency: 0.25	

Table 1. Test conditions

3.4.2 Testing Procedure

Before starting the grinding process, the grinding wheel must be dressed. During the operation, the grinding forces and power consumption are measured at each grinding pass. To assess wheel wear and actual material removal rates, the entire experimental test is divided into 11 tests block, with the number of passes detailed in Table 1 for each block. After each test block, the amount of material removed from the workpiece and the wear on the wheel profile are measured.

The grinding machine not only allows for grinding passes but also performs spark-out after each pass. Therefore, once the passes and spark-outs are completed in each test block, the amount of material ground is measured using a dial gauge on the workpiece. Since the power consumed in each pass and spark-out is measured, it is calculated. To calculate the material removal rate, it is assumed that the depth of cut is proportional to the power consumption. Hence, by knowing the total amount of material removed, the proportional part of power consumption in the pass and spark-out is assigned. This allows for the estimation of a_e. Furthermore, the grinding forces is measured in each pass and spark-out.

Additionally, after each test block, the procedure used to measure the wheel volumetric wear is shown in section 3.3.3. To minimize measurement errors, the height of the wear on the surface of the graphite are measured in nine different zones. Then, in order to validate that volumetric wear is the dominant factor in the experiment, attritious wear measurements are measured on the surface of the grinding wheel. This methodology is performed after each grinding test block. To minimize measurement errors, the attritious wear on the surface are measured in four different zones of the periphery of the grinding wheel. 2D images are taken, as can be seen in Figure 47a, RGB color code in adjust of image of Adobe Photoshop Cs is used. The resulting image shows the attritious wear in white color and the rest of the wheel in black (see in Figure 47b), facilitating comparison with the original image. Once the image matches, the attritious wear analysis software (GREAT) provides the percentage of the area representing the attritious wear on the grinding wheel.

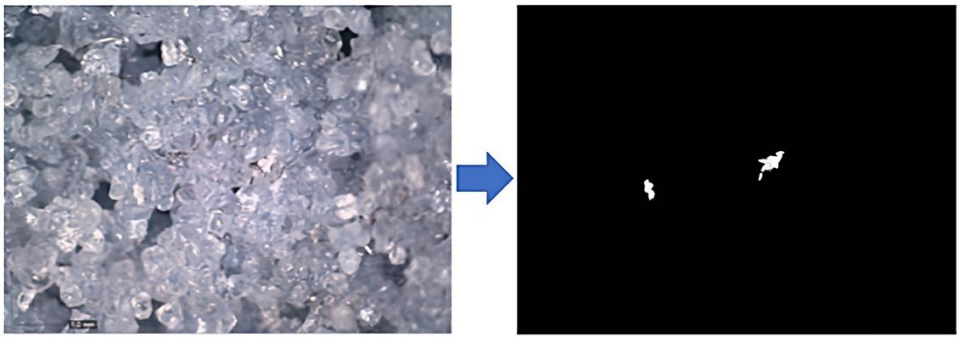

(a) (b)

Figure 47. Attritious wear quantification processing. (a) raw 2D images, (b) flat areas detection

Subsequently, the wheel profile is captured using a Dino-Lite Microscope, and the profile processing is performed using Matlab.

Finally, with the data obtained previously, the grinding wheel wear resistant is characterized. To characterize the grinding wheel wear, the grinding ratio or also called G-ratio is used [2]. This parameter is obtained from the volumetric wear of the grinding wheel and the removal volume of the workpiece in the steady-state wear regime. The grinding ratio can be expressed in Eq. (17). The formula is as follow:

$$G = \frac{\Delta V_w}{\Delta V_s} \tag{17}$$

where ΔV_w is the material removal volume of the workpiece in the steady-state wear regime and ΔV_s is the worn volume of the grinding wheel in the steady-state wear regime. In order to get a reliable G-ratio value, ΔV_s and ΔV_w must be correctly measured.

3.5 Discussion of results

This section presents a detailed analysis of the influence of grinding parameters on the generation and occurrence of bond fracture. Firstly, the authors discuss the impact of grinding parameters on bond fracture, specifically focusing on the evolution of volumetric wear with specific material removal for this type of grinding wheel. Additionally, the analysis of the influence of bond fracture on power, specific energy, grinding forces, topographic profile wear and the volumetric wear. Finally, the section presents an evaluation of the wheel surface, examining other types of wear in addition to the bond fracture phenomenon.

3.5.1 Power and specific energy

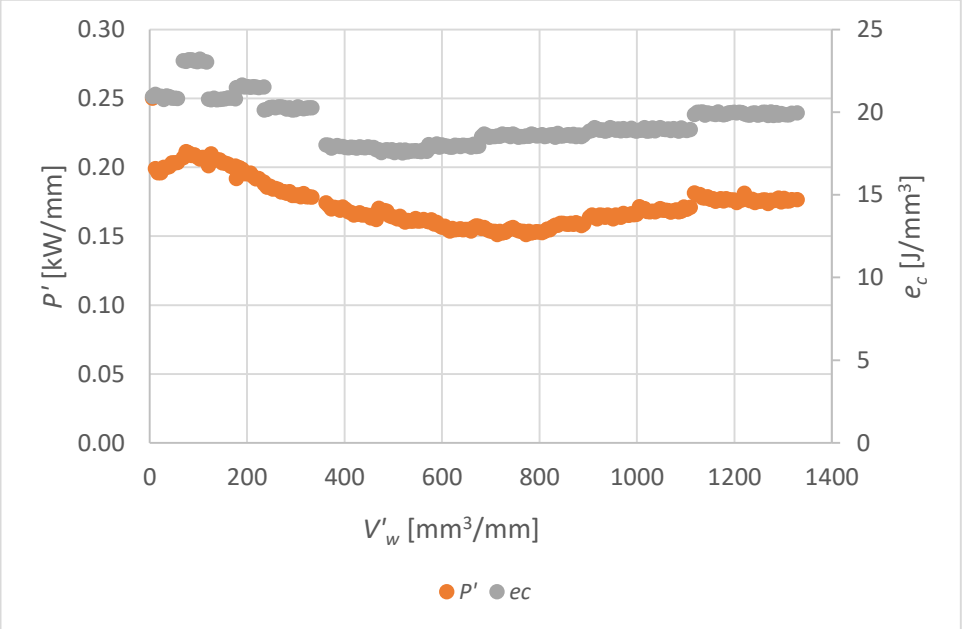

Figure 48. Specific power (P') and specific grinding energy (e_c) vs. specific volume of part material removed (V'_w)

The graph in Figure 48 displays the evolution of specific power (P') and specific grinding energy (e_c), in comparison to specific material removal. The graph can be divided into two distinct regions. The first zone, up until V'_w=400 mm^3/mm, is dominated by the dressing operation, during which P' and e_c reach maximum values of 0.21 kW/mm and 23.21 J/mm^3, respectively. The second zone remains unaffected by the dressing operation, and the values of P' and e_c remain almost constant at 0.18 kW/mm and 19.92 J/mm^3, respectively. It is evident that once the effect of the dressing process dissipates, the values of P' and e_c decrease. This behavior aligns with the fundamental principles of grinding theory, given that the overlap ratio used in the dressing process is 7.33 (fine dressing).

Moreover, in the second part of the graph, the constant values of P' and e_c suggest that the abrasive surface has similar cutting edges with every use, indicating that the predominant type of wear must be grain fracture and bond fracture. As such, attritious wear is not expected to occur, and volumetric wear is more likely to take place, which is reasonable considering that the grinding wheel is relatively soft.

3.5.2 Grinding forces

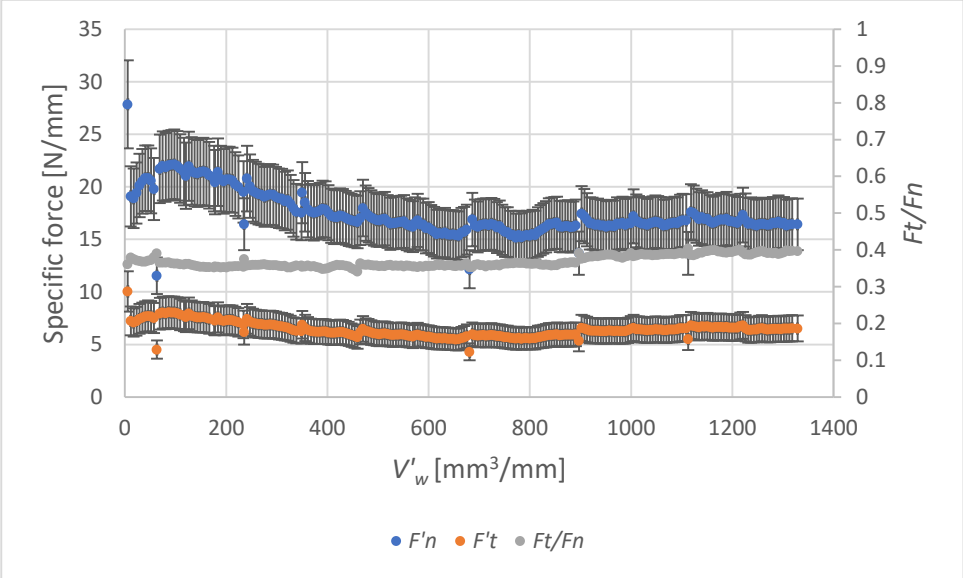

Figure 49. Specific normal (F'_n) and tangential (F'_t) grinding force vs. specific volume of part material removed (V'_w)

Figure 49 illustrates the evolution of the normal and tangential components of the specific grinding force (F'_n and F'_t respectively) as a function of the accumulated specific material removal. The results reveal a pattern similar to that observed in the power results, indicating the presence of two regions. The tangential force can be related to power consumption using Eq. (18), which demonstrates that in the dressing transitional zone, a maximum specific power consumption value of 0.24 kW/mm is reached, while a mean value of 0.18 kW/mm is observed in the non-affected stationary dressing zone. These findings are consistent with the P' values obtained in the previous graph.

$$P = F_t \cdot v_s \tag{18}$$

In contrast, the specific normal force remains constant in the non-affected stationary dressing zone, with average values of 16.39 and 6.12 N/mm for F'_n and F'_t, respectively. Additionally, the force ratio remains almost constant throughout the entire test ($F'_t/F'_n \approx$ 0.37). This observation suggests that the surface grinding wheel maintained a consistent material removal capacity, minimizing the occurrence of attritious wear and maximizing volumetric wear. Furthermore, the standard deviation of the measurements for both components remained stable at 15% during the entire experiment.

The total amount of part material removed is V'_w = 1338.92 mm^3/mm, which corresponds to a total of 240 passes since each grinding pass is 125 mm. The loss of geometry of the grinding wheel is assessed by machining a graphite replica and taking photographs at 50X of the profile left by the grinding wheel on the graphite using a Dino-Lite Digital ProX (AM4013) camera. The loss of complete grains and wheel geometry becomes evident at the center of the wheel, as shown in Figure 50.

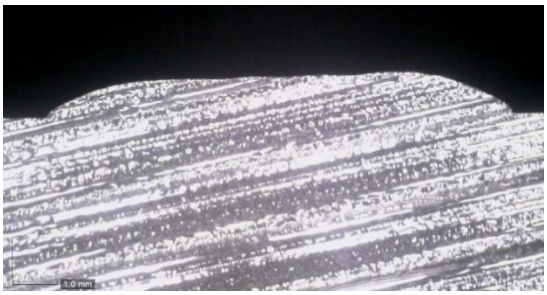

Figure 50. Loss of geometry as measured on the graphite workpiece at the center of the wheel (V'_w=900.12 mm^3/mm)

3.5.3 Volumetric wear

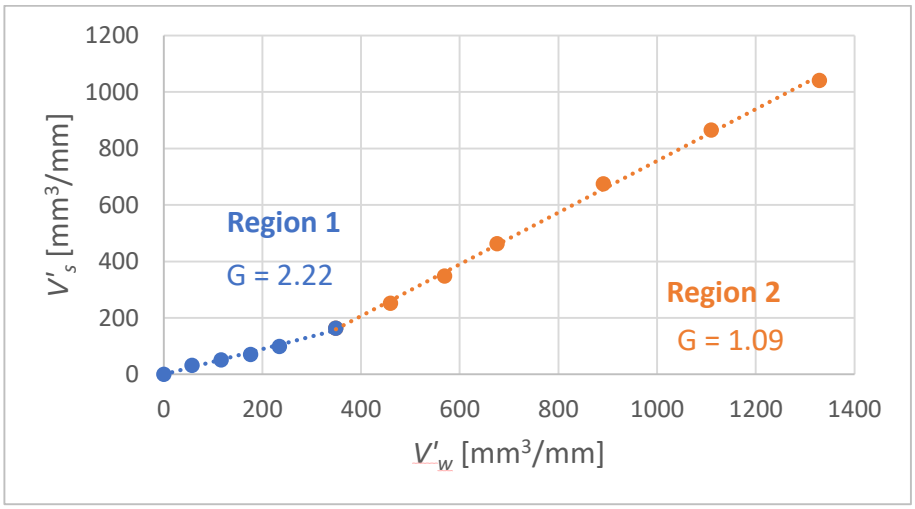

Figure 51. Specific volumetric wear V'_s versus specific metal removed V'_w.

Figure 51 illustrates the evolution of volumetric wear and G ratio, providing further evidence for the force analysis findings. The graph is divided into two regions, with the first region of which covers up to approximately V'_w=350 mm^3/mm and reflecting the influence of the dressing operation, while the second region highlights the impact of the

grinding wheel's actual structure. Both regions show linear behavior for volumetric wear, consistent with existing literature, with R^2 values of 0.989 and 0.998, respectively. The G ratio can be determined from these plots, with values of 2.22 for the first region and 1.09 for the second. These low G ratio values are not surprising given the use of a soft wheel for the experiments. The G ratio of the second region will be used for model validation, as it is not impacted by the transitional effects of the dressing process that will be excluded from the numerical modeling of the grinding process.

3.5.4 Profile wear of the grinding wheel

The profile wear evolution during the experiments is carefully monitored and recorded. The patterns of volumetric wear observed on the graphite sample are depicted in Figure 52. Each curve in the graph represents a specific value of V'_w, with the uppermost gray curve corresponding to the end of the experiment. It is important to note that, due to the configuration of the workpiece, the grinding width of $2w$ is applied within the total width of the wheel. However, for computational cost, the grinding width can be simplified to just w, as illustrated in Figure 52.

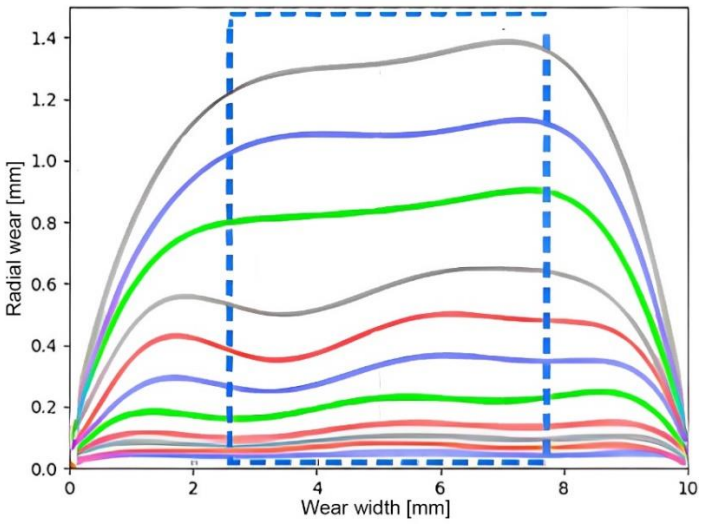

Figure 52. Evolution of the topographic profile wear of the grinding wheel after each grinding test block observed in the graphite replica.

3.5.5 Attritious wear quantification

As it mentioned previously, for the analysis of the wheel surface, the attritious wear analysis software is used. It compares the white and black image with the original image to measures attritious wear areas in percentages. The results are presented in Figure 53, where each experimental test block displays the average attritious wear values extracted from the images. The total results show an average 0.27% of attritious wear area. Based on these results, it is justified that there is no influence of attritious wear. These results are in line with Malkin's findings [2], where similar experimental tests showed attritious wear levels of up to 2%.

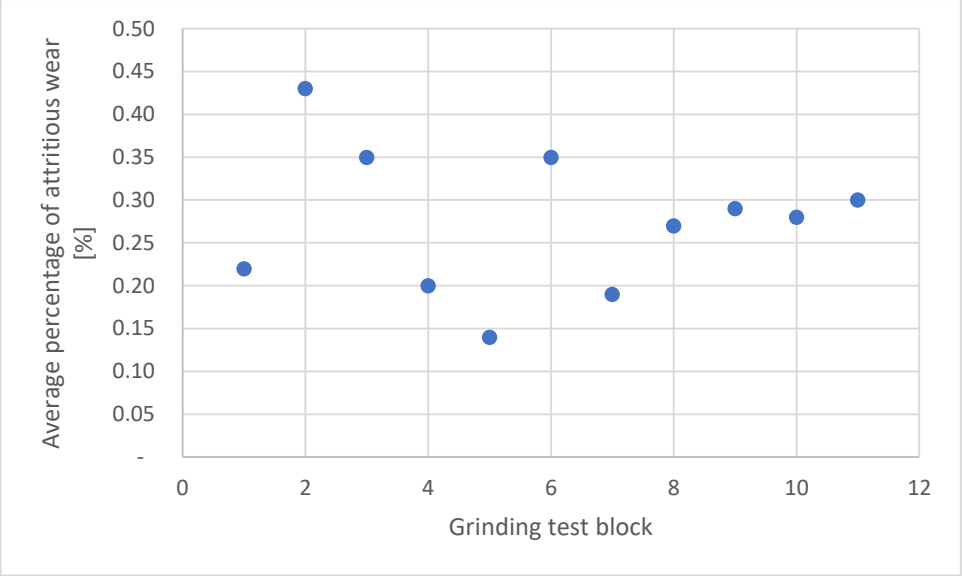

Figure 53. Average percentage of attritious wear in each experimental test block.

3.6 Preliminary conclusions

In this chapter, a comprehensive analysis is conducted to investigate the bond fracture phenomenon and its impact on the wear of vitrified alumina grinding wheels. An experimental methodology is meticulously detailed, aiming to isolate and highlight the evolution of bond fracture in these wheels. The influence of the grinding wheel's soft hardness grade EF is observed, specifically examining its effect on the appearance of the attritious wear in the grinding wheel surface. Significantly, it is observed that the occurrence of bond fracture is strongly influenced by both the grinding parameters and the hardness of the grinding wheel. These findings lead to the following conclusions:

- The methodology employed in this study to induce the bond fracture phenomenon in the grinding wheels is systematic and comprehensive. An approach is adopted, taking into account various factors such as the selection of appropriate grinding wheel and careful control of experimental conditions. By meticulously designing and implementing this methodology, it is possible to isolate and promote the occurrence of bond fracture in a controlled and reproducible manner.

- The findings of the present study shed light on the influence of soft hardness grinding wheels with hard monocrystalline grains on the occurrence of attritious wear. In the case of vitrified alumina grinding wheels composed of 100% monocrystalline grains, the total attritious wear area is determined to be approximately 0.27%. These results highlight the significant effect of soft hardness grinding wheels in amplifying the manifestation of bond fracture. The quantification of this effect further confirms the relationship between the soft hardness of the grinding wheel and the development of attritious wear. Different hardness grades can result in varying degrees of bond fracture and wear characteristics. The presence of hard monocrystalline grains in the grinding wheel reduces the occurrence of attritious wear, demonstrating the importance of the hardness characteristics of grinding wheels.

- The review of the state of the art has revealed that high Q_w' values contribute to the occurrence of the bond fracture phenomenon. As a result, an approach is proposed to use a Q_w' value of 12.5 $mm^3/mm \cdot s$, combined with elevated grinding parameters such as workpiece speed v_w =15000 mm/min, depth of cut a_e = 0.036 mm, and cutting speed v_s = 30 m/s. By adopting these settings, a clear tendency of bond fracture generation can be observed. These findings emphasize the importance of understanding and controlling the Q_w' value and grinding parameters in order to manage the occurrence of bond fracture. The proposed approach provides a practical strategy to induce and analyze bond fracture in a controlled manner, facilitating further research into its effects on grinding processes.

- Once the experimental test has been completed, the analysis of grinding forces and power has revealed the existence of two distinct zones: the dressing transitional zone

and the non-dressing transitional zone. On the one hand, in the first zone reach a G ratio of 2.22 and on the other hand, in the second zone reach a G ratio of 1.09. The obtained low G ratio values in the experiments can be attributed to the using of a soft grinding wheel. This finding is not unexpected, as softer wheels are known to exhibit higher wear rates. Within these zones, both tangential and normal grinding forces exhibit a nearly constant behavior. After of dressing transitional zone, this pattern is consistent with the friction coefficient, which also maintains a quasi-constant value of 0.37. The observed phenomenon can be attributed to the initial surface condition of the grinding wheel, as well as the specific grinding parameters designed to induce bond fracture phenomenon. These factors contribute to the prevalence of bond fracture as the primary mechanism during the grinding process.

Chapter 4

Multiscale simulation of the volumetric wear of vitrified alumina grinding wheels

4.1 Introduction

Grinding wheel wear is a significant research topic, as highlighted in previous chapters. Chapter II specifically addresses wear characterization, particularly bond fracture, emphasizing the need to address this issue. In Chapter III, bond fracture in vitrified alumina grinding wheels is investigated within the context of studying the grinding process. The experimental results underscore the substantial impact of bond fracture on grinding performance. However, a comprehensive analysis is required, considering the complexities of modeling grinding wheel wear and the variability in grinding wheel topography. Despite the existing literature's inability to predict grinding ratio (G ratio) accurately, this chapter aims to introduce the develop discrete element method model that simulate the contact

between the grinding wheel section and the workpiece and subsequent volumetric wear under realistic conditions. The idea is to understand bond fracture phenomenon and to get G ratio. For this reason, in the multiscale approach two parts are presented, integrating the mechanical behavior of vitrified bonds with the stochastic nature of grain location in the grinding wheel. The first part involves a DEM microscale model (μSM) represents the mechanical behavior of any specific region of the grinding wheel, while the second part incorporates the randomization of the μSM (RμSM) of the grinding wheel represents the stochastic nature of grain location. This approach significantly reduces computational time and determines the actual number of lost grains under specific grinding conditions. As demonstrated in Chapter II, there are DEM studies considering detached elements of the main bodies, providing a notable information. Additionally, chapter III focuses on characterizing bond fracture, emphasizing the importance of the grinding parameters and the hardness of the grinding wheel. Given the critical role of mechanical behavior in the bond fracture generation, DEM is employed to model the volumetric wear of vitrified alumina grinding wheels under grinding contact conditions. The model development uses GranOO, a free C++/Python discrete element workbench.

4.2 Description of the multiscale simulation

In this chapter, the main objective is to predict the volumetric wear of the grinding wheel. To accomplish this goal, a multiscale numerical model will be developed. Additionally, the research aims to gain a deeper understanding of bond fracture behavior under realistic contact conditions during the grinding process. To achieve this, two hypotheses based on the properties of each grain in the μSM, such as the variability of the critical penetration (δ_c) and the number of abrasive grains removed (N_r), are proposed. δ_c refers to the depth of penetration at which the initial separation of at least one discrete element occurs. On one hand, the first hypothesis updates the mechanical behavior of the binder as the grinding wheel wears. On the other hand, the second hypothesis considers the possible cumulative damage to the binder as grinding wheel wears. In the RμSM, random properties are generated in each grain. This means that every abrasive grain in the RμSM possesses its own unique values for δ_c and N_r.

The volumetric wear of a grinding wheel is influenced by both the mechanical behavior of the vitrified bond and the stochastic nature of the abrasive grain locations. Any proposed model must consider these fundamental factors. Grinding wheels are composed of randomly embedded abrasive grains on a bonding matrix, with a degree of porosity. Therefore, accurately reproducing the behavior of an entire grinding wheel is challenging, and most studies focus on modeling a section of the wheel [96], [142], [143].

DEM are numerical techniques used to model the behavior of a large number of individual particles or discrete elements [148]. These methods simulate various physical states, such as velocity, position, temperature, magnetic moment, and electric potential, which can require significant computational resources. DEM is a first-principle-based approach that employs Newton's laws of motion and contact mechanics to describe particle dynamics. The distinctive characteristic of DEM is their ability to represent media in a discontinuous manner, which makes them particularly suitable for studying phenomenon like multi-fracturing. Unlike Finite Element Methods (FEM), which may not accurately describe material wear or fracture, DEM excels in capturing such behavior. Hence, DEM is the appropriate numerical technique for the analysis conducted in this study. Additionally, DEM has been widely applied in various fields, including geomechanics, analysis of brittle materials, and controlling bulk solids in different industries.

The grinding wheel, composed of grains, vitrified bond, and pores, can be considered a discontinuous material, exhibiting behavior that can be effectively simulated using the DEM. The advantage of using DEM for simulating the wear of the grinding wheel lies in its ability to easily detach discrete elements corresponding to bond fracture. However, the focus of the analysis in this study is on the mechanical behavior of the vitrified bond. Therefore, it is desired to represent the grinding wheel as a continuous material. Nevertheless, simulating continuous material poses a challenge for DEM. To address this, a 3D cohesive beam model is implemented to accurately capture the behavior of the grinding wheel [144].

The model must possess the capability to accurately replicate the inherent heterogeneity present within the grinding wheel. For this reason, to capture the mechanical properties, a discontinuous body hypothesis is adopted, where the abrasive grains are represented as spherical discrete elements (DEs), and the binder is modeled using 3D cohesive elastic beams. The developing of a complete DEM model that simulates all grinding wheel would

be computationally impossible. Instead, a multiscale simulation model consisting of two parts is employed. First, a grinding wheel section model (μSM) is developed to represent the mechanical behavior of any region of the grinding wheel. However, the μSM alone cannot capture the wear behavior due to the stochastic nature of grain locations. Hence, the second part of the model incorporates a randomization of the μSM (RμSM), which contains complete geometric information about the abrasive grain locations on the grinding wheel.

The numerical environment follows the following steps: Firstly, μSM and RμSM are built according to their respective characteristics. Secondly, since the default behavior of the DEM leads to grain piling, resulting in a higher grain density compared to the center, a certain number of grains are removed. It allows to ensure a uniform grain density throughout the entire body. A similar process is applied to the RuSM, which is developed in Python, but in this case, there is a lower grain density at the edges. Subsequently, boundary and contact conditions are applied, and finally, the simulations are run.

In the following sections, both the μSM and the RμSM are described in detail, highlighting their respective roles in modeling the volumetric wear.

4.3 DEM microscale simulation model (μSM)

As mentioned in the previous section, the microscale model (μSM) represents the mechanical behavior of any specific region of the grinding wheel. This model adopts the discontinuous body hypothesis, where the discrete element (DEs) in the shape of spherical particles represents abrasive grains, while the elastic beams represent the binder.

4.3.1 Fundamentals of the DEM microscale model (μSM)

A DEM of the grinding wheel is developed using the GranOO workbench. GranOO is a collection of C++/Python libraries and tools that are specifically designed to describe the physical properties of discrete elements [148]. DEM is well-suited for modeling materials with discontinuities, making it a suitable choice for simulating wear, as discrete elements

can easily detach from the body. The decision to use DEM as the numerical method is driven by numerically representing the phenomenon of bond fracture.

To simulate the physical phenomenon of wear due to bond fracture, the separation of DEs from the virtual wheel body is numerically performed. The numerical model must accurately represent the mechanical properties of the grinding wheel, including the randomness in grain size and distribution. The hypothesis of this work is that bond fracture is related to the fracture of the vitrified bond, which is considered a continuous material (3D cohesive beam model). Additionally, the use of beam cohesive bond produces more realistic fracture patterns [144].

The model is discretized into DEs (mass, radius and position), which is represented by abrasive grains, and the beams represented by the vitrified bond. Two DEs and the cohesion between them is achieved by using beams are depicted in Figure 54a. To describe the mechanical behavior of the cohesive beam, the Euler-Bernoulli beam theory is applied. The cohesive beam model [144] has beams that provided stiffness to the model, forming bridges between DEs. The beams have no mass, and instead, the total mass of the body is attributed to DEs. The behavior of a beam is determined by four parameters, including two mechanical properties (Young's modulus E_μ and Poisson's ratio v_μ) and two geometrical parameters (radius r_μ and length L_μ). These parameters are considered microscopic parameters due to the discrete element scale and its interaction with its neighbors.

The position of each DE varies in each iteration, depending on the interaction of forces and torque reactions acting between them. These forces and moments generated tensile, bending, and torsion loading on the beams, resulting in normal stress (tensile and bending loading) and shear stress (torsion loading) as shown in Figure 54b. Elasticity is provided to the complete DEM model by following the calibration procedure of the micro-scale properties of the beams, which is applied by Osa [143] and based on the method established by André et al. [144]. The calibration procedure involves an iterative process based on virtual tensile testing of specimens until convergence between micro and macro properties of the sample is achieved. However, the model does not consider the possibility of beam fracture. Iordanoff et al. [149] use GranOO to describe multi-fracturation in tribological studies. This point will be addressed as a contribution in this work.

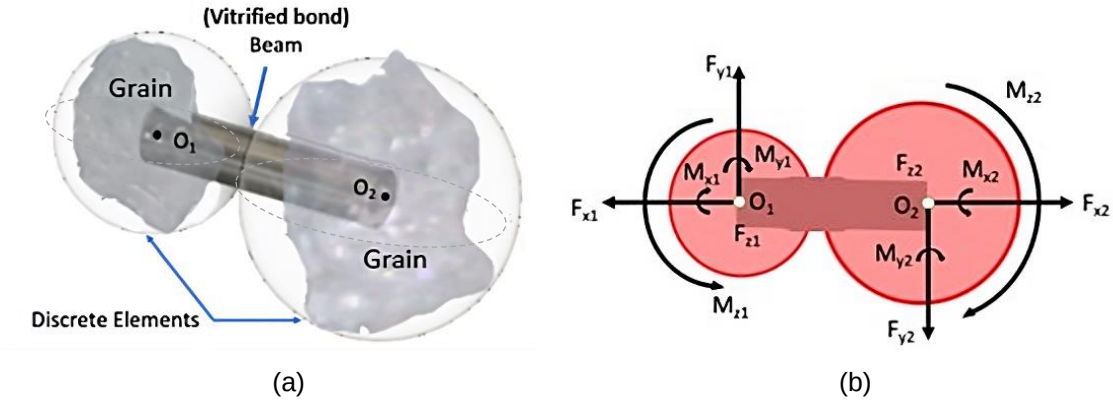

(a) (b)

Figure 54. Representation of DEs and beam: (a) DEs and beams representing abrasive grains and vitreous bonds, respectively; (b) System of forces and torques acting between two DEs.

4.3.2 Modelling wheel structure

This work begins by constructing a numerical model that accurately reflects the key characteristics of the grinding wheel, such as the radius of the DEs, the distribution of grit size, percentages of abrasive and binder materials as well as the domain dimensions.

4.3.2.1 Radius and mass distribution of DEs

In the scientific literature, various shapes of abrasive grains have been used in numerical models based on DEM, including spherical [150], pyramidal [151] and conical [152]. For this study, the selected shape for the abrasive grains is spherical, as it accurately reproduces the slope of the cutting edges.

The grain size is measured the diameter using microscope Dino-Lite Digital ProX (AM4013), and for the verification the average grit diameter (d_g) is calculated using Eq. (19) [2]. To account for the variation in grain size, the model employs a normal distribution of grain size, and sets maximum (d_{gmax}) and minimum (d_{gmin}) grain diameters based on the experimental grain size measured as shown in Figure 55. Once this information is gathered (see Table 2), the numerical sintering method [144] is used to construct the numerical model, which accurately represents the properties of randomness, homogeneity, and isotropy inherent in the actual grinding wheel.

$$d_g = \frac{15.2}{M} \tag{19}$$

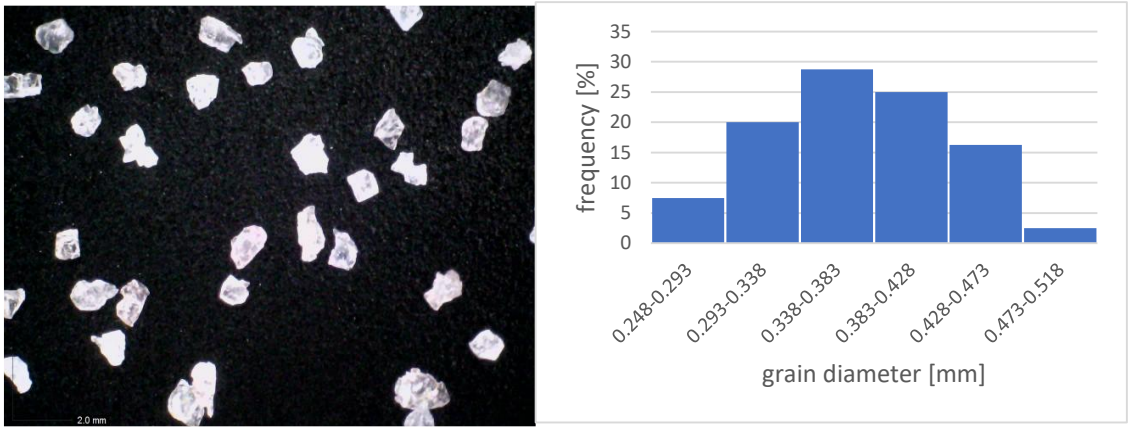

(a) (b)

Figure 55. Results for the wheel (MA46EF12V) used in the experimental test.
a) Different shapes of alumina grains observed under microscope (30x);
b) Experimentally obtained normal distribution of grain diameter.

Grinding wheel	
Dimensions (mm)	Ø250x127x40 mm
Technical designation	MA46EF12V489P20P
Abrasive type	Alumina
Binder type	Vitrified
Abrasive volume fraction, V_g (%)	41
Average grain diameter, d_g (mm)	0.36
Maximum grain diameter d_{gmax} (mm)	0.48
Minimum grain diameter d_{gmin} (mm)	0.244
Mass m (Kg)	2.5
Density ρ (Kg/m^3)	1776

Table 2. Physic characteristics of the vitrified alumina grinding wheel

In order to construct the μSM that accurately reflects the randomness, homogeneity, and isotropy properties of the actual grinding wheel, three conditions are considered during the model development such as the volumetric density of grains, mass density, and size distribution of grains. These conditions in the numerical body must match those of the real grinding wheel.

Undoubtedly, the computational cost for the creation of the model (all the grinding wheel) is exorbitant due to the vast number of elements involved (31742345 DEs). Additionally, the preceding step of numerical sintering may require an excessively long time to sinter the entire model. Therefore, it's imperative to reduce the number of elements without losing the connection with the actual problem.

For this reason, the build of the multiscale approach (μSM and RμSM) is necessary in this work. The μSM represent a section of the grinding wheel. It simulates the stress field in the region of the wheel in contact with the workpiece and reduce computational cost while RμSM accounts for the actual and random location and size of the alumina grits in all grinding wheel.

4.3.2.2 Domain dimensions

To ensure both accuracy and computational efficiency of the μSM, a localized approach has been implemented, limiting the μSM's extent to the region of the grinding wheel where grinding forces significantly influence the process. For this particular case, 3D model of the grinding wheel is created using ANSYS® Mechanical software. Hexahedron elements are employed to mesh the grinding wheel in three dimensions. The mesh size is uniformly set at 1 mm, with a refined size of 0.5 mm specifically in the contact area. The analysis incorporates grinding and centrifugal forces, contact area, and wheel properties that align with the experimental tests outlined in Section 3. Figure 56 show the model and the resulting deformations. Notably, deformations exceeding 0.8 μm are considered. For this analysis, the model height of 6 mm is applied. Additionally, to prevent border effects, the surface length of the model section, denoted as $2l_c$, is twice as long as the actual contact length, l_c. Furthermore, to account for the symmetrical nature of the results, the contact width, w, is halved, and forces are assumed to act within $w/2$. Additionally, to mitigate any potential border effects, the μSM's width is set to w. The resulting dimension of the μSM

section is depicted in Figure 57. As a consequence of adopting this localized approach, the volume of the grinding wheel section can be effectively represented.

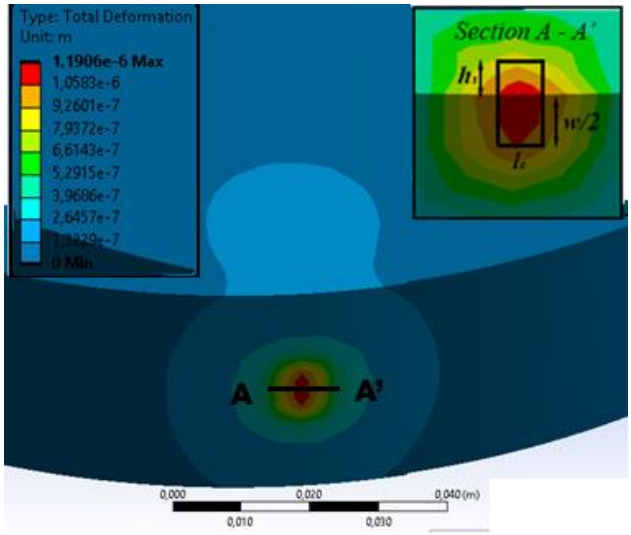

Figure 56. FEM model of wheel deformation under the effect of grinding and centrifugal forces.

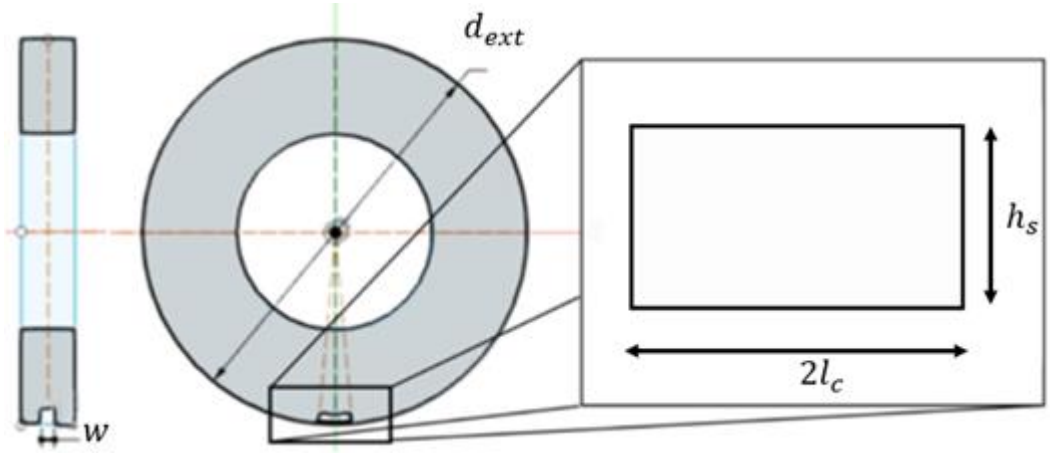

Figure 57. Size of the grinding wheel section

Determination of l_c can be accomplished by using the classical formulation that considers the geometric contact length and the Hertz deformations of the two bodies in contact (wheel and workpiece). Eq. (20) [153] expresses that relationship:

$$l_c^2 = l_g^2 + l_f^2 = a_e d_e + \frac{8R_r^2 F_n' d_e}{\pi E^*} \tag{20}$$

Here a_e is real depth of cut, d_e is effective wheel diameter, R_r is roughness factor, F_n' is the normal grinding force per unit width obtained from experiments and E^* is the combined Young modulus of the grinding wheel and workpiece.

The specific normal force $F_n´$ and Young's modulus of the wheel E_s is obtained from the experimental test and grindometer respectively. Finally, with these data, the N_{DE} has been reduced to 10482 elements as shown Table 3.

Number of discrete elements	10482
Width of model section w (mm)	10
Length of model section $2l_c$ (mm)	9.64
Height of model section h_s (mm)	6

Table 3. Dimensional data of μSM

Finally, after completing the creation of μSM, a structural comparison is performed between the μSM and the actual grinding wheel. The results of this comparison demonstrate a strong agreement, as evident in Table 4. The final discretization is shown in Figure 58.

	μSM	Actual grinding wheel
Grain density (grains/mm^3)	16.36	16.84
Density (g/mm^3)	1.776e^{-03}	1.776e^{-03}
Mean radius (mm)	0.18	0.18
Max radius (mm)	0.24	0.259
Min radius (mm)	0.122	0.124

Table 4. Structural comparison of μSM and the actual grinding wheel

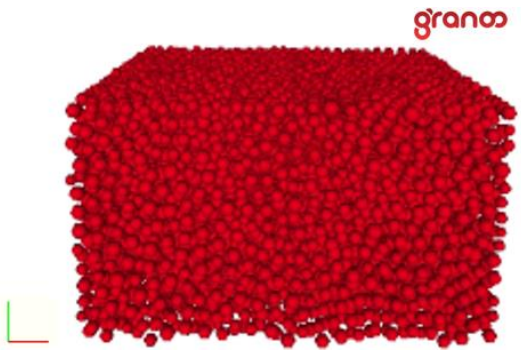

Figure 58. Discretization of μSM.

4.3.3 Boundary conditions (μSM)

After sintering the numerical model of the grinding wheel, the boundary conditions are established as follows: the grinding wheel is assumed to be infinitely rigid in the axial, lateral, and radial directions beyond the deformation region. This is achieved by restricting the degrees of freedom of the DEs on the XY plane, lateral walls, and inner ring as depicted in Figure 59. Moreover, in reality, the restricted area of the model also prevents free movement of the discrete elements when micro tangential forces are generated at the contact. The μSM is subjected to a rotational speed of 240 rad/s, resulting in the application of centrifugal force on each differential element. Additionally, the coefficient of friction is applied to the contact between the wheel and workpiece. Finally, for simplicity, the workpiece is represented as a non-degradable body, with the limits set at the actual contact length, half of the grinding width, and an arbitrary height. The role of the workpiece in the μSM is to establish contact.

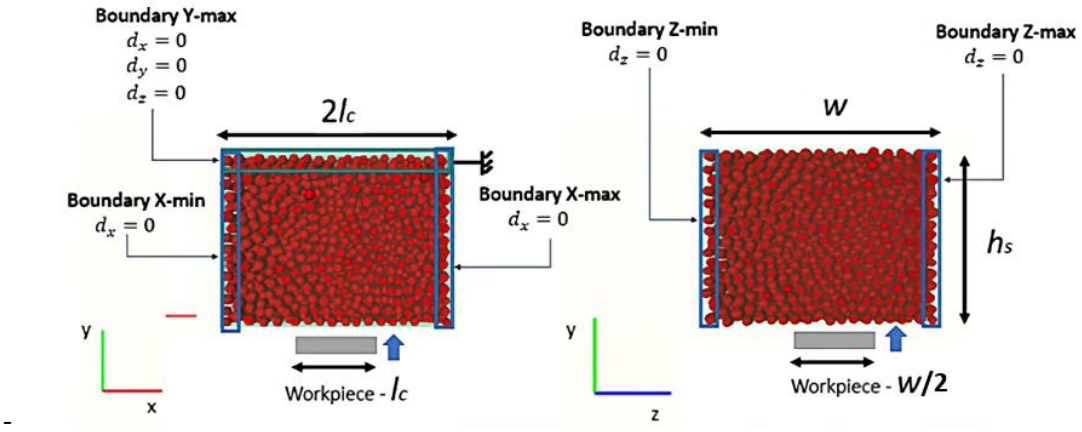

Figure 59. Boundary conditions of the μSM.

4.3.4 Model set-up

The μSM is developed by using the mechanical properties of the grinding wheel, as well as the data and results obtained from experimental grinding tests, as described in section 3. The experimental grinding test data is collected and employed to validate and calibrate the model. To effectively manage the contact between DEs, the model implements a contact detection method and contact laws. These components play a crucial role in determining the forces involved during the contact process. The contact detection method, based on geometric algorithms, allows for the identification of interpenetration between pairs of DEs. Simultaneously, the contact laws define the reaction forces that occur between two DEs when interpenetration is present. In order to accurately represent the actual bond fracture phenomenon, the model calculates and adjusts its inputs. These inputs cover various parameters, including the centrifugal force, contact stiffness, friction coefficient and failure stress. Each of these parameters contributes to capturing the intricate dynamics of the system.

4.3.4.1 Centrifugal force

The centrifugal force is a physical parameter that significantly affects the mechanical behavior of the grinding wheel. Despite the static nature of the μSM, the centrifugal force is effectively generated by simulating the rotation of the model. Specifically, the centrifugal force, denoted as f_{ci}, experiences variations based on the mass m_i, the distance from the wheel center r_i, and the rotation speed of the grinding wheel w for each DE. Consequently, this centrifugal force, f_{ci}, is applied to each DE individually, considering their respective characteristics. The calculation of f_{ci} is determined by employing Equation (21):

$$f_{ci} = m_i \cdot w^2 \cdot r_i \tag{21}$$

By using this equation, the value of f_{ci} can be accurately determined. The inclusion of the centrifugal force enables the model to account for the rotational effects and their impact on the mechanical behavior of the grinding wheel in a comprehensive manner.

4.3.4.2 Contact stiffness

When the μSM comes into contact with the workpiece, the contact stiffness is considered. The contact stiffness is denoted as *k*. To obtain the contact stiffness for the μSM, experimental values of grinding forces and a theoretical value of grain penetration (δ_{max}) are used. Following classical models [41], δ_{max} can be calculated using the expression:

$$\delta_{max} = \frac{{l_c}^2 - a_e d_e}{4 d_e} \tag{22}$$

Here, l_c represents the current contact length between the wheel and the workpiece, a_e signifies the actual depth of cut, and d_e denotes the equivalent diameter of the wheel. As illustrated in Figure 60, the parameter δ_{max} denotes the maximum penetration that occurs between the wheel and the workpiece.

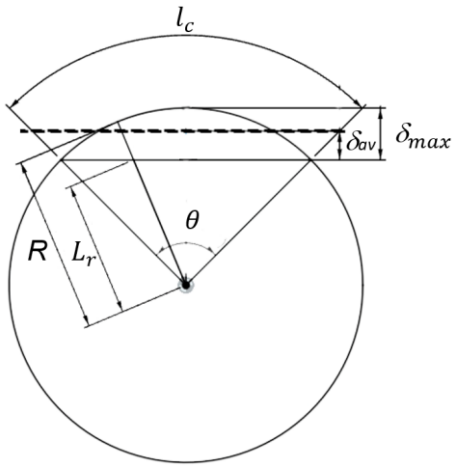

Figure 60. Schematic diagram for calculation of δ_{av}.

The variability of penetration along the actual contact length is evident in Figure 60. To obtain an average value of grit penetration (δ_{av}), Eq. (23) can be utilized:

$$\delta_{av} = \frac{1}{\theta} \int_0^{\theta} [R - L_r]\, d\theta \tag{23}$$

Furthermore, *K* can be determined by employing the normal grinding force (F_n) obtained from experimental data:

$$K = \frac{F_n}{\delta_{av}} \tag{24}$$

When the workpiece interacts with the μSM, the individual forces acting on each DE combine to replicate the typical grinding force experienced by the wheel (as depicted in Figure 61).

$$F_n = K \cdot \sum \delta_j \tag{25}$$

4.3.4.3 Friction coefficient

The friction coefficient is a crucial factor in determining the resistance to sliding between the μSM and workpiece. This value is obtained through experimental results, yielding a coefficient of μ = 0.37. Once the contact between the DEs and workpiece is established, reaction forces are applied by the discrete elements. As depicted in Figure 61, the DEs are required to penetrate the workpiece, with δ_j representing the depth of penetration of individual DEs and δ_{av} indicating the maximum depth of penetration. The penetration leads to the establishment of a contact area, which enables the calculation of normal and tangential forces when the grinding wheel reaches its maximum grit penetration.

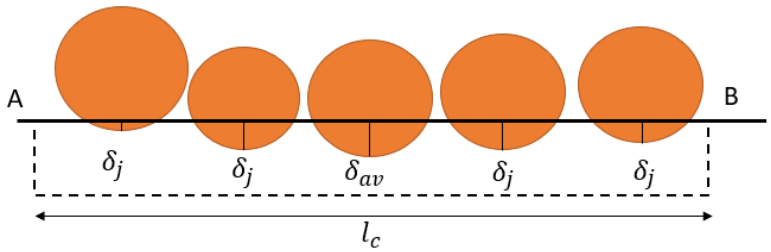

Figure 61. Contact detection on contact length segment A - B between DEs and workpiece

4.3.4.4 Failure stress

According to ASTM C 1161 standard [154], the failure stress σ_f can be determined by conducting tests on three samples. These tests involve a span length of 120 mm and a loading rate of 2 mm/s. The calculation for determining σ is given by Eq. (26), where F represents the load sustained by the specimen, b denotes the width of the specimen, h

represents its thickness of the specimen and L is the distance between two supports span. During the test, the Force vs. displacement curve is recorded. Consequently, the stress vs strain is obtained as shown in Figure 62.

$$\sigma = \frac{3FL}{2bh^2} \tag{26}$$

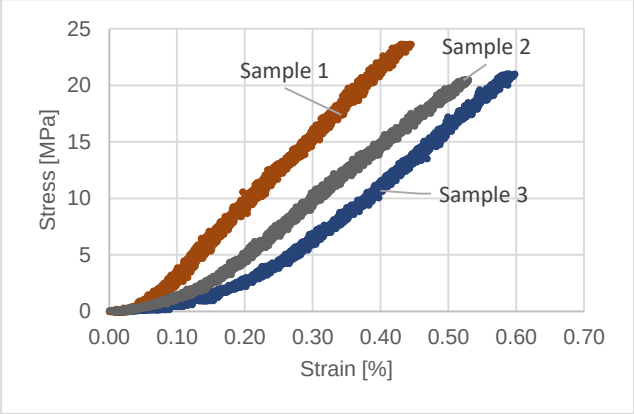

Figure 62. Stress vs strain of three samples from 3 bending test.

4.3.5 Failure criteria and calibration of the µSM

4.3.5.1 Failure criteria

The hypothesis proposed in this study suggests that the wear of the grinding wheel occurs when DEs are detached from the µSM. The failure criteria adopted for the beams is the maximum micro failure stress. Thus, the behavior of the µSM is based on the failure stress observed in the beams.

According to Zhou et al. [26], the vitrified bond materials in the grinding wheel are susceptible to brittle fracture during wear. In order to incorporate this hypothesis into the model, a brittle material criterion using Rankine theory is implemented in the Granoo workbench. The Rankine criterion is concerning to the maximum principal stress, and its application to the beam is defined by Eq. (27), where σ represents the normal stress and τ denotes the torsion stress of the beam. As a result, the failure criteria for the grinding wheel wear model is established, as shown in Eq. (28).

$$\sigma_{max} = \sigma + \sqrt{\sigma^2 + 4\tau^2} \tag{27}$$

The beam fractures if the following condition is met:

$$\boldsymbol{\sigma_{max} \geq \sigma_{fu}} \tag{28}$$

Finally, the DE is detached when all the beams connected to this DE are broken, as illustrated in Figure 63.

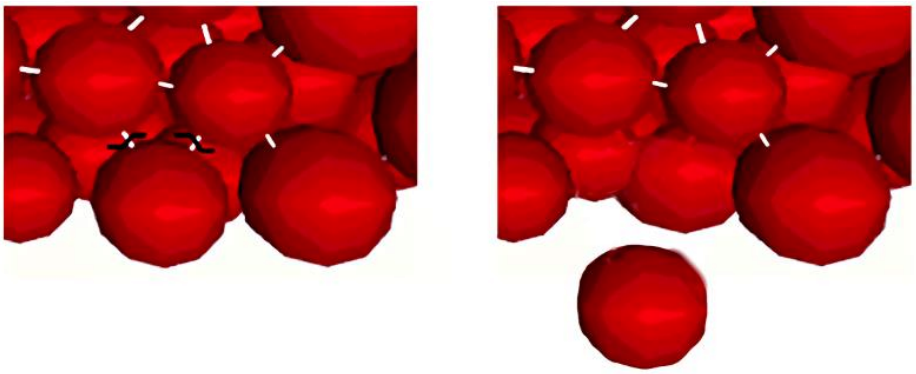

Figure 63. DE removal from the μSM following Rankine criterium.

4.3.5.2 Calibration of the micro properties

The micro failure stress (σ_{fu}) and macro failure stress (σ_f) are key mechanical properties considered in the grinding wheel model. The σ_{fu} represents the micro-mechanical property of the model, while the σ_f represents the actual macroscopic mechanical property of the grinding wheel. To determine the micro-mechanical properties that define the cohesive beams of the grinding wheel model, namely E_u (Young's modulus), v_u (Poisson's ratio), and σ_{fu}, a calibration process using a virtual tensile test is conducted. This calibration process, outlined by Andre et al. [144], relies on the knowledge of the macroscopic mechanical properties of the grinding wheel.

The macroscopic mechanical properties, E_s (Young's modulus) and v_s (Poisson's ratio), corresponding to different hardness grades, are provided by the grindometer, as well as the σ_f values are obtained through three-points bending test, as detailed in section 4.3.4.4. The

calibration steps involved establishing the correlation between the macroscopic mechanical properties and the micro-mechanical properties of the grinding wheel model.

The calibration process is based on the use of a numerical uniaxial tensile test on a cylinder composed of 10,000 discrete elements (DEs). This number of DEs or higher is considered appropriate to obtain reliable and reasonably accurate results, as recommended by André. The calibration process consists of two steps. Firstly, to determine the ratio between the cohesive beam radius and the average DE radius (r_μ), an arbitrary value is initially chosen, in this case, v_μ =0.2, as vμ has minimal influence on the macro properties. Once the virtual test is completed, the value of r_μ is adjusted to achieve the desired v_μ as shown in Figure 64. Therefore, the value of r_μ is fixed. Secondly, to determine the E_μ and $\sigma_{f\mu}$, a second tension test is performed, where the micro values are adjusted until a stable curve is obtained for the macro values Es and σ_f, as shown in Figure 65. Finally, the values of E_μ and $\sigma_{f\mu}$ are fixed.

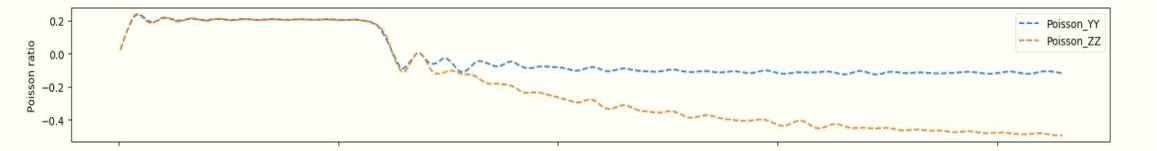

Figure 64. Results of the initial tensile test showing the calibration process for obtaining a stable value of macro Poisson ratio (v_s).

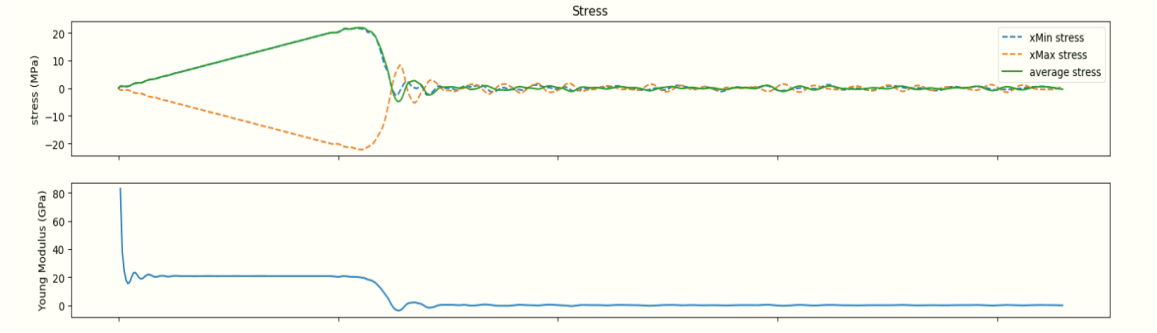

Figure 65. Results of the second tensile test showing the calibration process for obtaining a stable value of macro Young modulus (E_s) and reach the macro failure stress (σ_f).

The results of the calibration process, including the values for E_μ, ν_μ, and σ_{fu}, are presented in Table 5.

Young´s modulus E_s (GPa)	20
Beam Young´s modulus E_μ (GPa)	120
Poisson ratio ν_s, ν_μ	0.2
Beam diameter ratio (m)	0.538
Beam failure stress $\sigma_{f\mu}$ (MPa)	167
Failure stress σ_f (MPa)	21.75

Table 5. Macro and micro properties of the grinding wheel model

4.3.6 Active grain density in µSM.

It is essential to achieve an equal grain density throughout the body, without any excessive or defective protruding grains. However, during the creation of the µSM, the DEs often tend to accumulate at the boundaries during numerical sintering (already described by Osa et al. [143]), resulting in an uneven distribution of grain density between the surface and the body. Therefore, this section is dedicated to addressing this issue and ensuring a homogeneous grain density distribution across the entire model.

To achieve a consistent grain density, The grain density is measured throughout the µSM. The obtained grain density values are then presented and visualized in Figure 66.

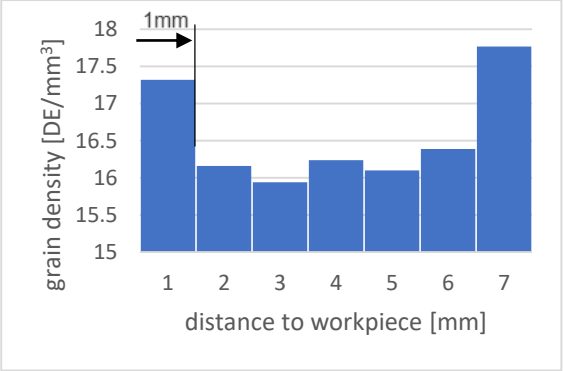

Figure 66. Surface grain density in *µSM*. Effect of element pile-up from numerical sintering.

To achieve a balanced distribution of grain density, a technique employed is the removal of the first layer of grains on the surface. As depicted in Figure 66, within 1 mm of the boundaries of the µSM, higher densities exceeding 17 DE/mm^3 can be observed. However, towards the center, the density becomes more homogeneous with a slight variation, averaging at 16.36 grains/mm^3.

For this study, only the first layer of grains, which comes into contact with the workpiece, is removed. This approach results in a more homogeneous grain density across the entire body, allowing for a more accurate representation of the real-world grinding process. After removing those layers, a comparison of the resulting structures is presented in Table 6.

	µSM	Actual grinding wheel
Grain density (grains/mm^3)	16.36	16.84
Density (g/mm^3)	1.776e^{-03}	1.776e^{-03}
Mean radius (mm)	0.18	0.18
Max radius (mm)	0.24	0.259
Min radius (mm)	0.122	0.124

Table 6. Structural comparison of µSM and the actual grinding wheel

4.3.7 Simulation of the µSM

The flowchart in Figure 67 illustrates the µSM process of simulation. The simulation starts with a non-contact between the µSM and the workpiece. At this stage, the lowest grain/DE is identified, and the reference point is established at y = 0. Then, the movement of the workpiece is applied through the µSM where it is moved continuously from the lowest grain to the maximum radial wear (determined through experimental test). The position of DEs is monitored in each iteration. During the contact, the µSM considers the centrifugal forces and determines the actual normal and tangential forces.

Next, the stress and deformation fields are obtained. As the workpiece continues to advance, N_r and δ_c are calculated. Moreover, the normal and tangential grinding forces per unit width (F'_n and F'_t) and the number of discrete elements in contact are confirmed. With the available data, the next step involves performing the simulation using the RµSM.

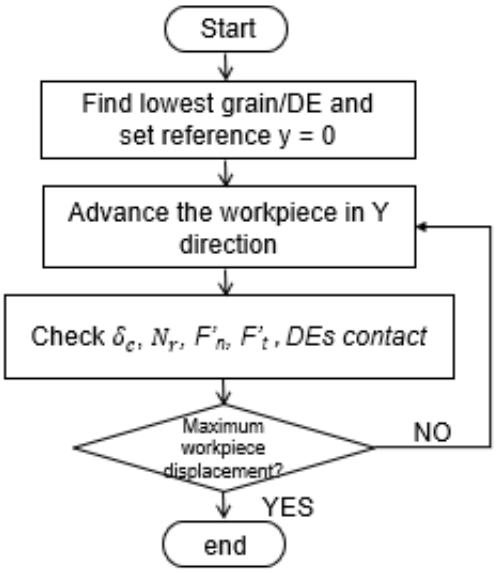

Figure 67. Flow chart showing the algorithm of the µSM.

4.4 Randomization of the µSM (RµSM)

4.4.1 Develop of the RµSM

As mentioned previously, in order to estimate the wear of the grinding wheel throughout the grinding process, the RµSM needs to be created. The µSM alone, developed in the previous section, is insufficient to fully explain the wear behavior of the grinding wheel. The stochastic nature of grain location and bonding bridges, along with the mechanical properties, plays a critical role in the phenomenon of bond fracture. Therefore, any explanation of volumetric wear must consider the interaction between these factors.

The motivation for developing the RµSM arises from the need to simulate the sintering process across the entire grinding wheel domain, while also considering the real-life distribution of alumina grits in terms of their random locations and sizes. The goal is to achieve this while keeping the computational costs as low as possible. The RµSM is generated in python using the same assumptions regarding wheel density and grain size distribution explained in Section 4.3.2. The numerical sintering method, previously used for the µSM, is then applied to the entire grinding wheel domain. The outcome is a normal distribution with characteristics similar to the µSM, with an average grain diameter of 0.360 mm. Consequently, the RµSM provides the actual location and radius of each DE.

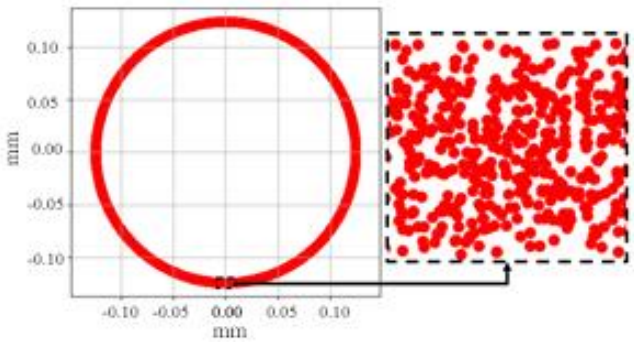

Figure 68. Macroscale geometry (RµSM) sintered in the complete domain of the grinding wheel.

Furthermore, the RµSM enables the representation of a rotation counter for the grinding wheel, which is essential for measuring the grinding ratio G. In the simulation, the outermost grain, referred to as the DE, is positioned in the RµSM. The distance between the DE and the center of the wheel is denoted as R_i, where i represents the rotation counter

of the wheel. The outermost grain signifies the initial contact between the grinding wheel and the workpiece, marking the beginning of the grinding process.

In the specific case of this study, a radial width of 2 mm is considered, as it aligns with the maximum wear observed in the experimental part, which is 1.4 mm. This approach enables the creation of a portion of the grinding wheel rather than the entire wheel. This not only simplifies the RµSM but also reduces the computational cost associated with it.

4.4.2 Active grain density

As it mentioned before, it is essential to achieve an equal grain density throughout the body, without any excessive or defective protruding grains. However, during the creation of the RµSM, there is a lower grain density observed on the surface compared to the body. Such non-uniformity can significantly impact the accuracy and reliability of simulations. Therefore, this section is dedicated to addressing this issue and ensuring a homogeneous grain density distribution across the entire model.

To achieve a consistent grain density, the grain density is measured throughout the RµSM. The obtained grain density values are then presented and visualized in Figure 69.

Figure 69. Surface grain density in *µSM* and *RµSM*. Boundary-induced lower density in the *RµSM*

To achieve a balanced distribution of grain density, a technique employed is the removal of the first layer of grains on the surface. As depicted in Figure 69, within 0.5 mm of the boundaries, the grain density differs significantly from the density observed towards the center, remaining relatively constant at 16.78 grains/mm^3.

For this study, only the first layer of grains, which comes into contact with the workpiece, is removed. This approach results in a more homogeneous grain density across the entire body, allowing for a more accurate representation of the real-world grinding process. By employing this technique, the grain distribution becomes more balanced and reflective of the actual behavior of the system, thereby improving the reliability of the simulations conducted. After removing those layers, a comparison of the resulting structures is presented in Table 7.

	RμSM	Actual grinding wheel
Grain density (grains/mm^3)	16.78	16.84
Density (g/mm^3)	-	1.776e^{-03}
Mean radius (mm)	0.18	0.18
Max radius (mm)	0.259	0.259
Min radius (mm)	0.124	0.124

Table 7. Structural comparison between RμSM and the actual grinding wheel

4.4.3 Algorithm for estimating of the volumetric wear.

The volumetric wear of the vitrified alumina grinding wheel at a macrogeometric level, beyond the individual mechanical behavior of binder in each grain, encompasses multiple simultaneous phenomena. Considering all of these phenomena when establishing the behavior of the RμSM is complex. Therefore, two possible hypotheses are proposed to quantify the volumetric wear based on the calculated δ_c and N_r in the μSM:

- Updating the mechanical behavior of the binder as the grinding wheel wears.
- Considering the possible cumulative damage to the binder as the grinding wheel wears.

Hypothesis 1:

The flowchart in Figure 70 illustrates the algorithm of the RμSM. From the outermost grain in all periphery of the wheel, δ_c is applied. δ_c is the first critical penetration that is obtained from μSM in 1 preprocessing. The grains in contact and whose δ are equal to or greater than the specified δ_c are removed. Furthermore, the adjacent grains that must be removed (N_r) are located relative to this reference. δ_c and N_r of one preprocessing are determined in section 4.5.2. Then, a rotation is obtained (j = j+1), and the new outermost grain is then used as a new reference point. The radial wear (Δ) is measured as the distance between the current outermost grain and the previous rotation's outermost grain. The radial wear accumulates. Based on this value, it is determined that if the accumulated radial wear is equal or greater than the position of the workpiece *WP*, a change is made to $\delta_{c\,new}$, $N_{r\,new}$ and WP_{new}. The $\delta_{c\,new}$ is applied, and the process is repeated.

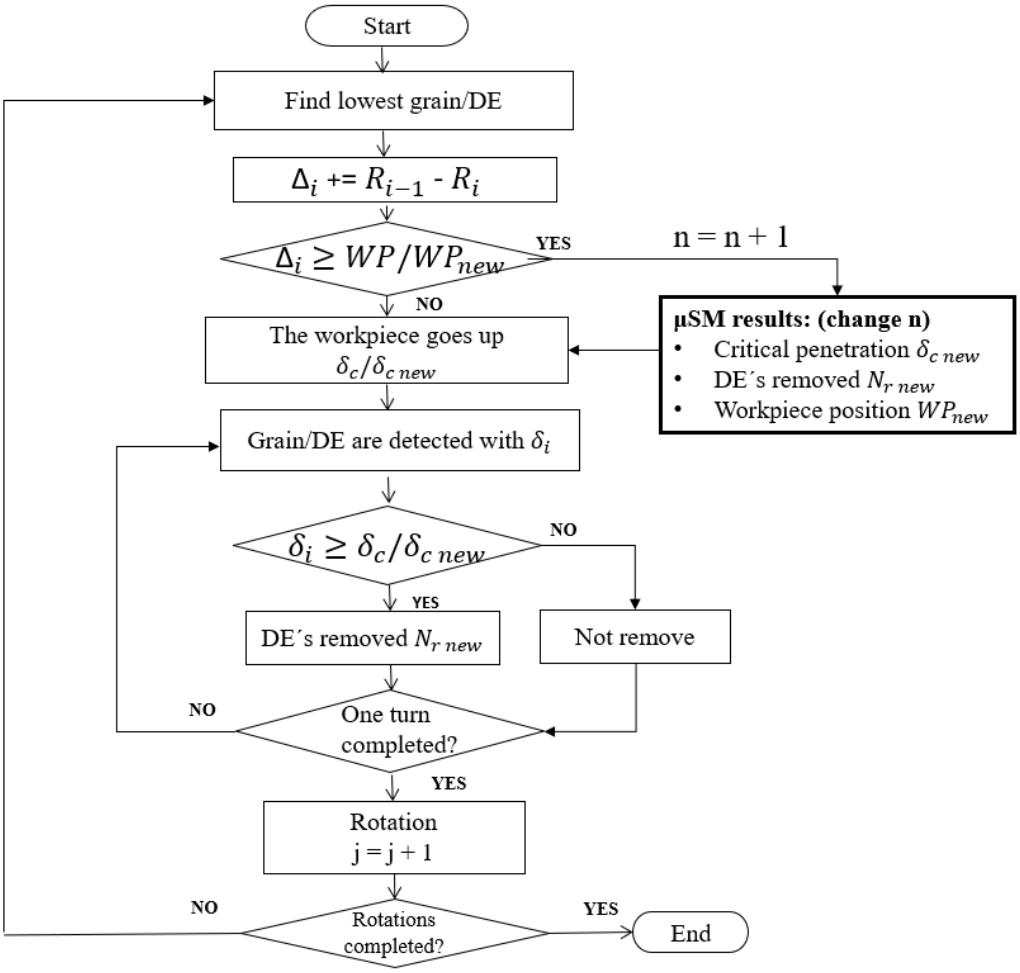

Figure 70. Flow chart showing the algorithm of the RμSM in Hypothesis 1.

Hypothesis 2:

The flowchart in Figure 71 illustrates the RμSM process of simulation. From the outermost grain in all periphery of the wheel, δ_{max} is applied. The grains in contact and whose δ are equal to or greater than the specified δ_c (corresponding to each grain) are removed. Furthermore, the adjacent grains that must be removed (N_r) are located relative to this reference. δ_c and N_r corresponding to each grain are determined in section 4.5.3. Then, a rotation is obtained (j = j+1), and the new outermost grain is then used as a new reference point. The radial wear (Δ) is measured as the distance between the current outermost grain and the previous rotation's outermost grain. The radial wear accumulates. The δ_{max} is applied again, and the process is repeated.

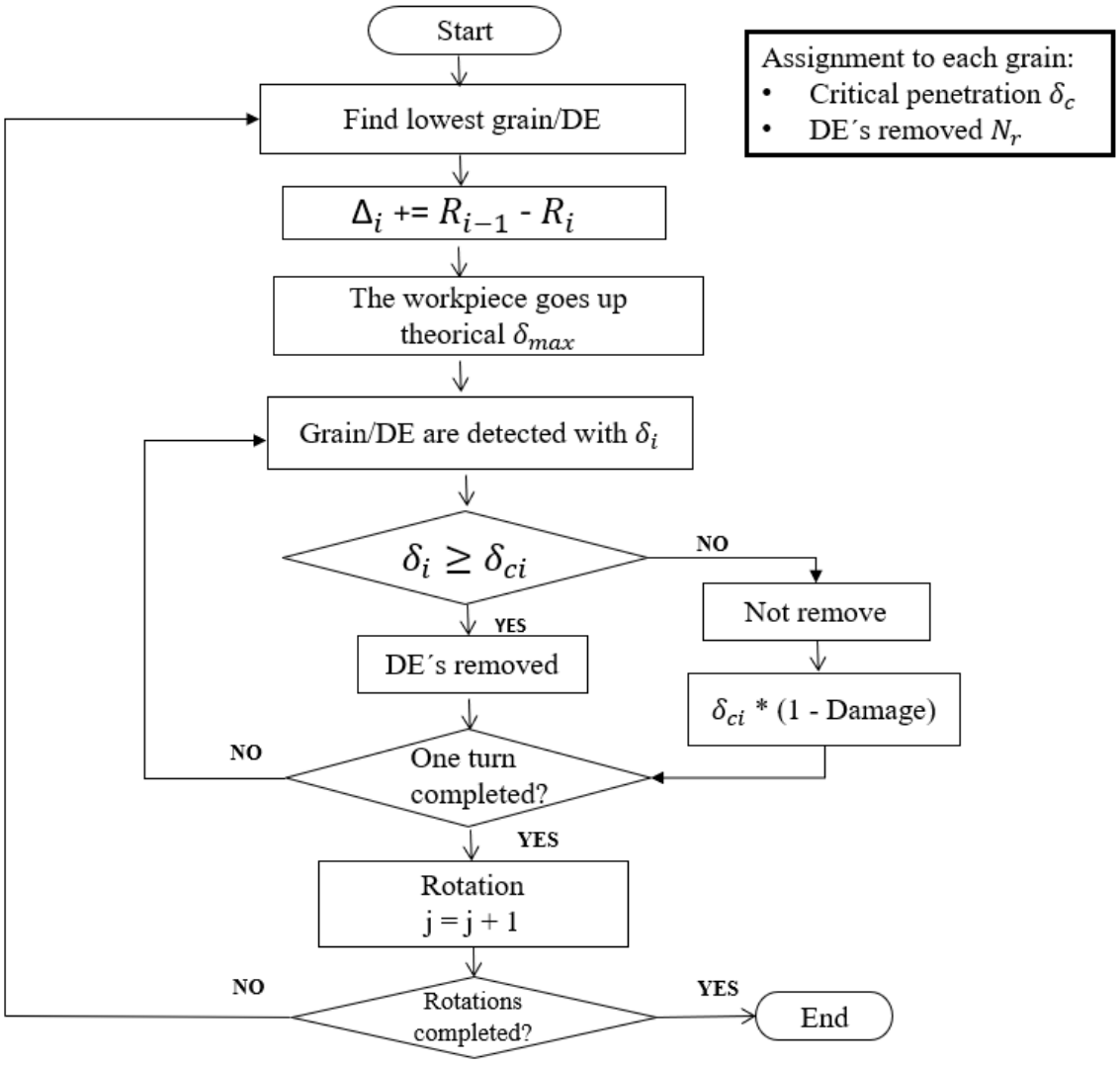

Figure 71. Flow chart showing the algorithm of the RμSM in Hypothesis 2.

4.5 Multiscale simulations and discussion of results

This section compiles the simulation results and compares them with the experimental tests. The first step involves obtaining the actual values that will be inputted into the model, which is essential to generate a real contact between the μSM and the workpiece with the same conditions as in reality. Once the μSM and RμSM simulation are completed, the variability of δ_c and N_r are analyzed in the three preprocessing stages and the volumetric wear is estimated. This analysis helps to determine the mechanical behavior of the binder in the three preprocessing stages. In addition, the force system in the μSM is generated during the contact phase, and validation against experimental results allows us to assess whether the mechanical behavior is consistent with the entire grinding wheel.

Regarding the simulation, the simulation time heavily depends on the technical specifications of the computer used. Two different computers running different software are used. On one hand, the μSM simulation lasted between 20 and 24 hours using a Linux Mint 19.1 operating system, an Intel Core i5 processor running at 3.6 GHz. On the other hand, the RμSM simulation took between 10 to 15 minutes using an Intel 11th generation Core i5-1135G7 processor clocked at 2.40 GHz. In each iteration, the sensor recorded the position of the DEs, δ, N_r from the model, and the normal and tangential forces applied to the workpiece.

4.5.1 Actual contact length, contact stiffness, and friction coefficient.

The theoretical values of l_c, k, and μ are obtained using equations (20), (22), and (29), respectively. In order to determine the actual l_c, the parameter R_r is taken into consideration. The roughness factor is a parameter that quantifies the surface roughness generated on a workpiece during grinding operations. According to the literature on grinding, this parameter typically falls within the range of 5 to 15. However, in a static contact model developed by Osa [143] for the dressing conditions applied in this study, a specific value of 5.1 is obtained and utilized in the model. Additionally, as the forces used in the model are derived from experimental tests, the coefficient of friction could be determined by employing Equation (29). All these data are shown in Table 8.

$$\mu = \frac{F_t{}'}{F_n{}'} \tag{29}$$

Real depth of cut a_e (mm)	0.036
Grinding wheel diameter d_e (mm)	250
Roughness parameter R_r	5.1
Normal force per unit width, F_n' (N/mm)	16.39
Tangential force per unit width, F_t' (N/mm)	6.12
Combined Young Modulus E^* (GPa)	19.08
Average value of grit penetration δ_{av} (mm)	0.00774
Actual contact length l_c (mm)	4.82
Contact stiffness K (N/m)	10632785.27
Friction coefficient μ	0.37

Table 8. Actual contact length, contact stiffness and friction coefficient

.

4.5.2 Variability of critical penetration and number of DE´s removed in different µSM.

The analysis of the variability of δ_c and N_r is of significant importance as it provides valuable information about the mechanical strength of bonding bridges within grinding wheels. As previously mentioned, δ_c represents the depth of penetration that leads to the initial separation of at least one discrete element from the wheel. In order to gain a better understanding of the range of critical penetration and its underlying factors, a study is conducted to examine the variability of δ_c and N_r.

To carry out this study, three different µSMs (preprocessing 1, 2, and 3) are created using procedure 4.3. This approach allowed for the generation of models with discrete elements positioned in a manner that closely resembled the actual arrangement of grains on the grinding wheel. Once the models are created, simulations are conducted. Since the focus of this analysis is solely on the µSMs, the procedure is applied following section 4.4.3 on the µSMs. Upon completion of the simulation, the results are analyzed. The contact between the wheel and the workpiece generated stresses in the beams, causing the grains to separate at a certain penetration depth, based on the configuration of grain positions. The unified results from these simulations are presented in Figure 72, illustrating how different grain positions in contact with the workpiece led to variations in δ_c and N_r.

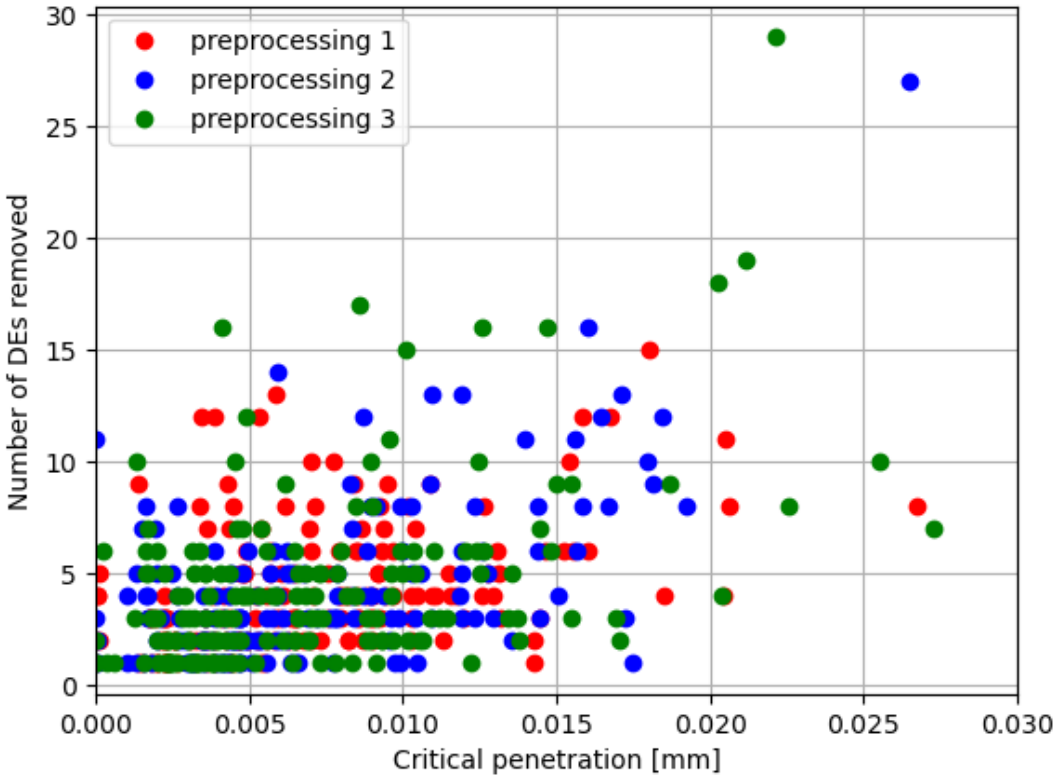

Figure 72. Critical penetration vs DE´s removed

Figure 72 depicts the relationship between δ_c and N_r. In each µSM, the value of N_r for a given δ_c is determined by measuring the advancement of the workpiece from the moment it made contact with the grain until at least one grain is separated from the µSM. As shown in Figure 72, a similar trend is observed for the three µSMs. Calculations reveals that the

mean value of δ_c is 0.00685 ± 0.0262 mm (mean ± variance), while the mean value of N_r is 4.28 ± 16.1. It should be noted that negative values do not hold physical significance in this context. Furthermore, a correlation analysis is conducted to explore the association between δ_c and N_r. The covariance between the two variables is determined to be 0.0101. This indicates a positive linear relationship between the variables, suggesting that they increase together.

Figure 72 provides concise and relevant information regarding the influence of grinding parameters on the actual hardness performance of the grinding wheel.

4.5.3 Statistical treatment of the mechanical strength of bonding bridges in each grain

Since the variability presented by the geometry and arrangement of abrasive grains are inherently stochastic, the model presented will be a statistical approach and will be applied in the hypothesis 2. In this work, the mechanical strength of bonding bridges to bond fracture in each grain of the grinding wheel is analyzed using probability statistics. To better understand the mechanical behavior of these bonding bridges, the variability of the δ_c and $N_{r.}$ across the three preprocessings is examined. It is well-known that preprocessings consist of a section of the grinding wheel, and to represent each grain of the entire wheel, multiple values of δ_c and N_r must be created. As shown in Figure 72, the values of δ_c and N_r are based on a statistical normal distribution. To generate random properties on each grain based on these two parameters, the Multivariate Random Normal Function or Multinormal is used. As it is shown in the Figure 73, this type of distribution is defined by its mean and covariance matrix of both parameters, which are analogous to the average and standard deviation of a one-dimensional normal distribution.

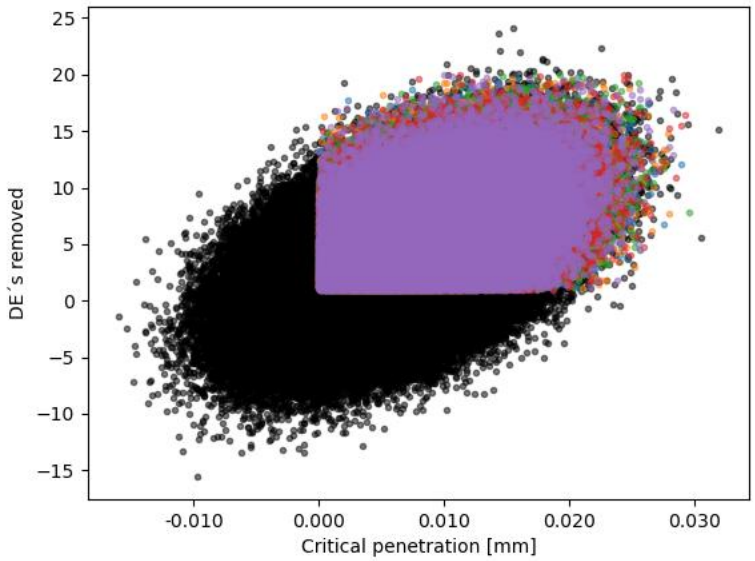

Figure 73. Multivariate Random Normal Function from critical penetration and DE´s removed

This plot represents the mechanical behavior of the bonding bridges of the grinding wheel. As can be seen in the plot, there are points in the negative section represented by black dots. However, it is important to note that negative values are not physically meaningful in this context. Therefore, these values are truncated using an approximate MCMC sampling method [155]. After removing the black dots, each remaining point in the plot is assigned to a specific abrasive grain in the RµSM, resulting in a total of 129732 assigned points. It provides a δ_c and N_r to each abrasive grain in the RµSM.

4.5.4 Validation of the system of forces acting on the µSM.

For the simulations, the grinding forces are calculated by analyzing the contact between the *µSM* and the workpiece. To ensure accurate results and minimize random errors, three *µSM* models are created using procedure 4.3. Once the models are established, the simulation is conducted. Since the focus of this analysis is solely on the *µSMs*, the procedure is applied following section 4.4.3 on the µSMs. To measure the forces exerted by each active grain, contact between DEs and the workpiece is considered. The DEs in contact are treated as active grains, and their total forces are separated into normal and tangential components. The sum of the normal and tangential forces of all active grains represented the overall normal and tangential grinding forces. After completing the

simulation with the post-processing 2, the results are analyzed, and the specific forces (i.e., specific normal and tangential forces) and the loss of grains versus the position of the workpiece are plotted in Figure 74.

The data clearly demonstrates that when the workpiece initially compressed the μSM, it generated significant normal forces of up to 34 N/mm. This substantial force is a direct result of the presence of all the grains on the *μSM's* surface. However, as the workpiece advanced and underwent further compression, numerous grains became dislodged from the surface. Starting from a workpiece position of 0.15 mm, the rate of grain loss exhibited a linear trend, suggesting a consistent level of surface wear that persisted until the end of the simulation. Consequently, the forces experienced varied throughout the entire simulation. Additionally, the curve depicts several abrupt drops, indicating instances when the workpiece is no longer in contact with the *μSM*. Overall, the findings indicate that nearly 600 grains are lost from the *μSM* within a workpiece displacement of 1.4 mm.

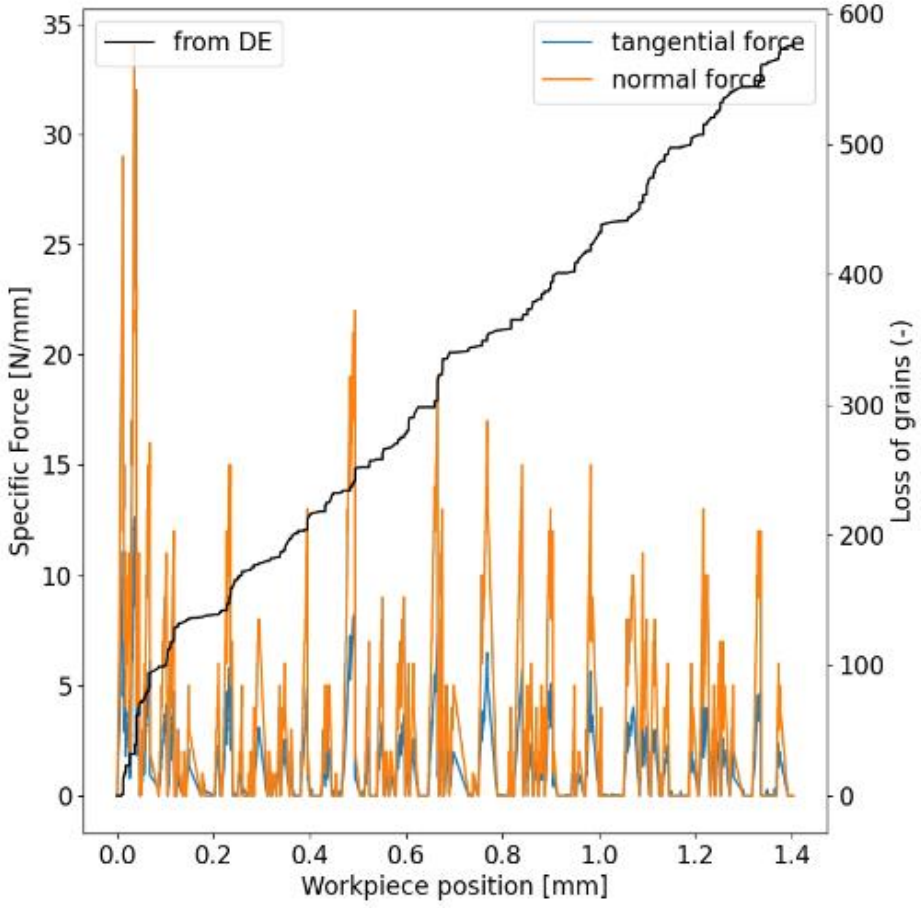

Figure 74. Measurement of specific forces and grain losses according to workpiece position in μSM.

(a) (b)

Figure 75. Voids left on the surface by the volumetric wear seen in the cut plane B-B' of µSM. (a) Workpiece position 0.2 mm (b) Workpiece position 0.25 mm

Figure 76 presents a comprehensive comparison between the results obtained from validation experiments and corresponding simulations in terms of grinding forces. To facilitate further analysis, the force peaks are extracted and plotted at specific workpiece positions. It is important to note that, in this initial approach, the influence of dressing is not taken into account. In the graph, the experimental results of the specific normal force (ranging between 13 – 20 N/mm) are depicted in the gray zone, while the results from the *µSM* simulations (post-processing 1, 2, 3) in the steady state are shown. The validation analysis indicated that approximately 16.96% of the specific normal force values from the model fell within the experimental range. However, it is also observed that a considerable portion of forces exceeded the experimental range, accounting for 13% of the total. Conversely, a larger percentage of forces fell below the experimental range. These observations can be attributed to the generation of low forces in certain sections of the wheel in contact. On the other hand, sections where the wheel in contact generated high forces exhibited overlapping during the measurement process. These factors contribute to the concordance observed between the experimental and simulated force values.

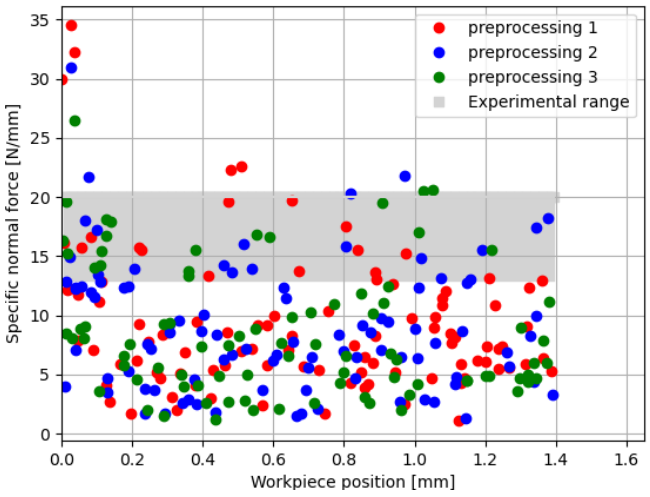

Figure 76. Comparison between extracted peaks of the specific normal force from the simulation

The loads on the binder are analyzed using μSM to examine volumetric wear. The binder plays a crucial role in transmitting grinding forces within the grinding wheel. However, measuring this experimentally is complex, necessitating the use of numerical models to understand its evolution throughout the grinding process. Figure 77 illustrates the observation of beam stress at different positions of the workpiece and with varying wear levels in the cut plane B-B' of μSM.

In terms of the maximum failure stress, σ_{fu} = 167 MPa corresponds to beam failure based on the applied failure criteria. On one hand, as shown in Figure 81a, when the workpiece position is at 0.36 mm, it is evident that due to contact, the grinding force propagates through the DE-beam and its neighboring beams, displaying different colors such as red, orange, and green. These colors correspond to stress levels of 50 MPa, 80 MPa, and 167 MPa, respectively, as indicated by the color legend. It can be observed that four grains above the farthest grain are affected by stresses of 50 MPa, while three grains above experience the maximum stress. These stress distributions serve as evidence of the voids that occur in some cases when the grains are removed from the model as evidenced in Section 4.5.2.

On the other hand, in Figure 77, when the workpiece position is at 1.05 mm, it can be observed that the contact generates stress in the beams with less transmission compared to the previous figure. This difference arises due to the specific configuration of the grain positions at that moment. However, it is noteworthy that the maximum failure occurs at a distance of one DE above the DE in contact. [Pa]

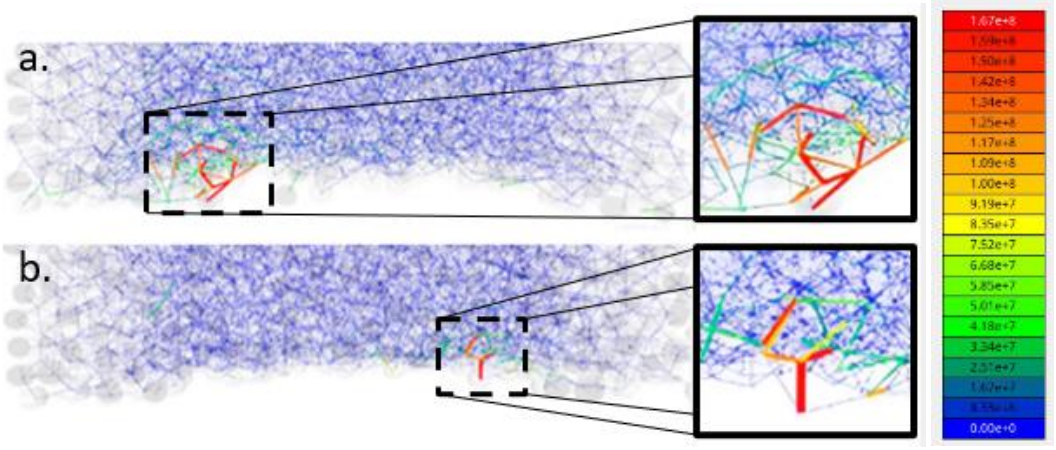

Figure 77. Beam Stress Analysis in the Cut Plane B-B' of μSM at different workpiece positions. (a) Workpiece position 0.36 mm. (b) Workpiece position 1.05 mm.

In summary, the μSM (multiscale simulation model) proves its capability to accurately describe the realistic mechanical behavior and grinding performance at a single contact length in grinding.

4.5.5 Estimation of radial wear and G ratio

This section focuses on the validation of the radial wear and G ratio predictions obtained from multiscale simulations. The purpose is to compare the results obtained from the simulations with the experimental data presented in section 3, considering the two hypotheses proposed. To calculate the G ratio, two parameters are necessary: the specific volumetric wear of the grinding wheel (V_s') and the specific volumetric material removal of the workpiece (V_w'). In the simulations, V_s' is determined based on the measured radial wear in the RμSM, while V_w' is calculated by considering the number of rotations in the RμSM.

Hypothesis 1:

The assumption of perfectly spherical abrasive grains in the RμSM introduces uncertainty regarding the actual δ_c, explained in section 924.3.2.1. To address this, a shape factor S_f is introduced, representing the percentage deviation of the δ_c from the value obtained in μSM. A sensitivity analysis varied S_f from 0% to 10%. Figure 78 compares experiments and simulations, focusing on the steady-state region (region 2) and excluding the dressed region that it will be investigated in future research. The experimental curve shows a different behavior in the dressing-affected region. The comparison is limited to regions with similar grain density (Table 7).

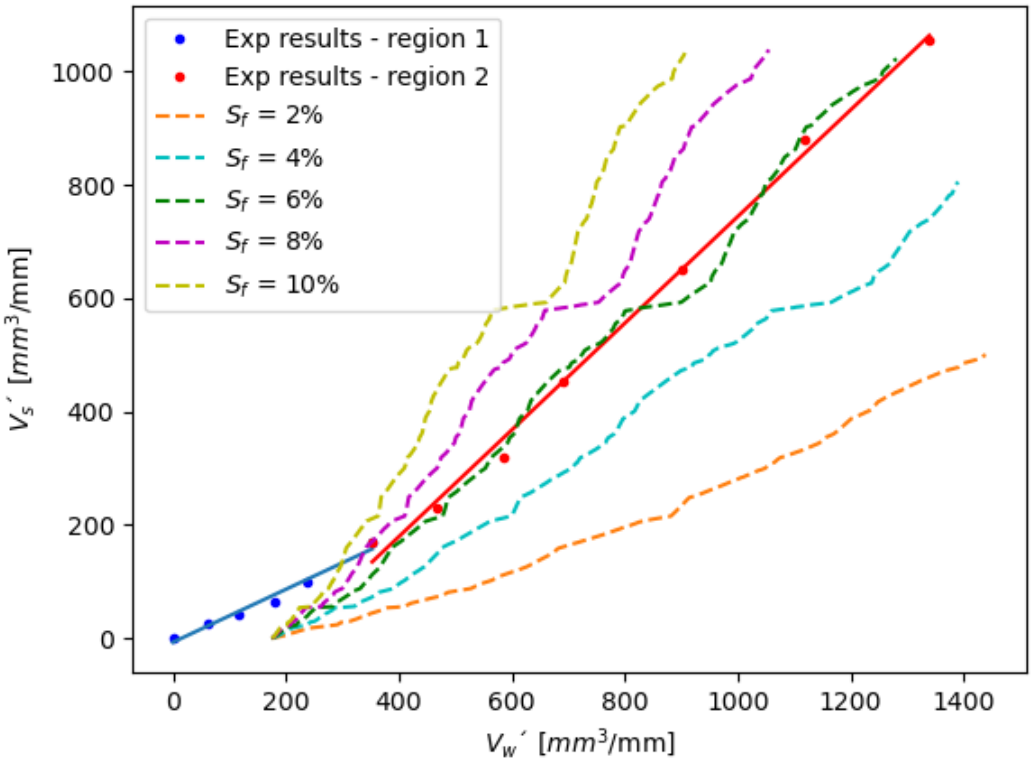

Figure 78. Comparison of wear between multiscale simulations and experiments.

These results demonstrate an excellent agreement between the experimental findings in region 2 and the results obtained from the multiscale simulation with an S_f of 6%. Both exhibit a G ratio of 1.09. The 6% deviation from δ_c corresponds to 0.8574 μm, which can be attributed to the micro-cutting of the abrasive grains. Regarding Figure 79, the multiscale simulation with an S_f of 6% yields similar results in terms of radial wear.

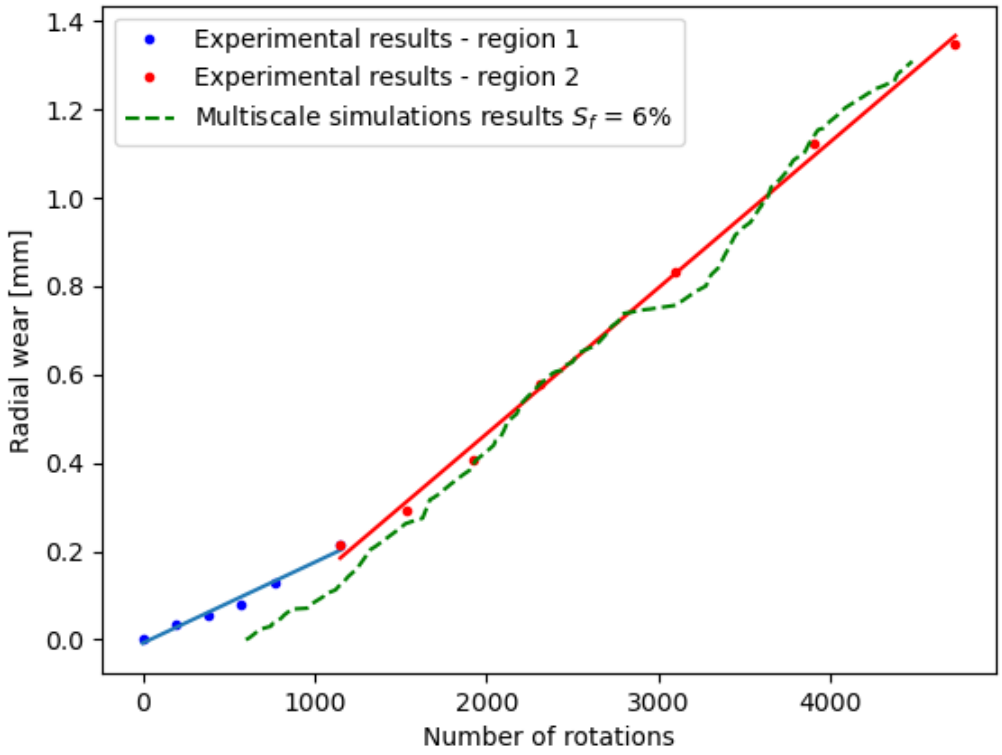

Figure 79. Experimentally measured and simulated radial wear for a shape factor value of S_f=6%.

To perform a comparative analysis of the profile of the wheel wear evolution, it is necessary to consider both the experimental and the multiscale simulation results. As it mentioned before, the actual morphologies of the grinding wheel wear are obtained from the graphite cube shape. The evolution of the profile of the wheel wear in relation to the RμSM profile is presented in Figure 80. The profiles of experimental test blocks 7, 9, and 11, corresponding to V'_w values of 569.11, 890.94, and 1329.12 mm^3/mm, respectively, are taken into account, along with the profiles from the multiscale simulation when the number of wheel revolutions matched those of the experimental tests upon completing the grinding test block. As seen in Figure 80, the level of radial wear in the RμSM closely matches the experimental results. This comprehensive approach provides a robust prediction of the RμSM profile, closely resembling the actual profile of the grinding wheel. The multiscale simulation accurately represents the local effects on grain detachment, while the accumulated radial wear effectively captures the volumetric wear behavior of the grinding wheel.

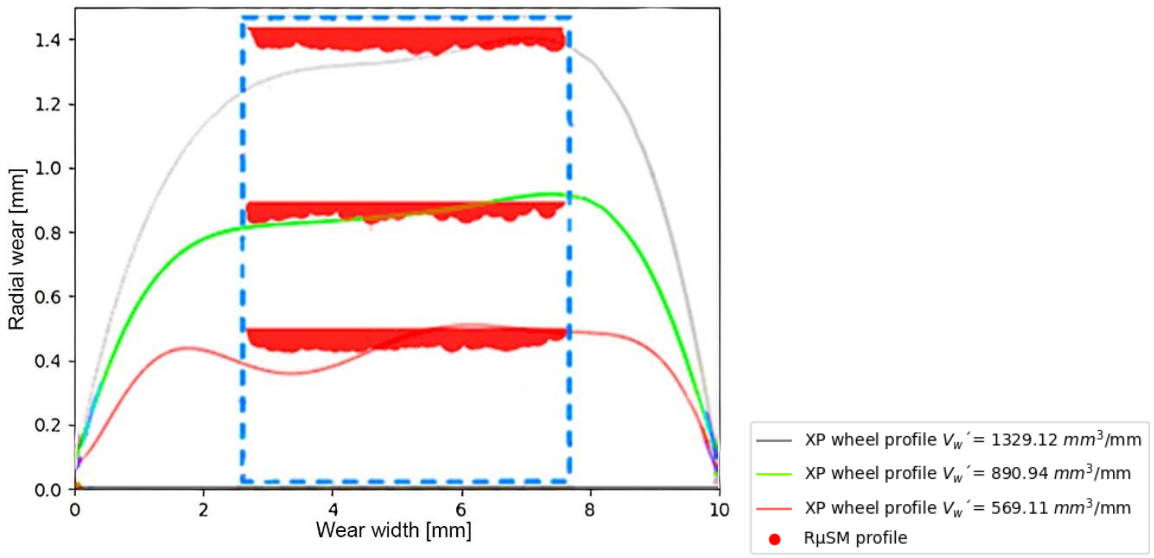

Figure 80. Evolution of the graphite replica profile (XP, experimental) and simulated RμSM profile at three different values of V'_w.

The two regions depicted in the results exhibit significant differences, as explained earlier, primarily due to variations in grain density on the surface. These disparities in turn produce distinct outcomes. Consequently, future studies will need to analyze these effects more comprehensively.

Hypothesis 2:

It's important to note that the resistance of bonding bridges to bond fracture depends on the arrangement of the grains, making δ_{max} a measure of this resistance. The maximum penetration to which a grain can be subjected is δ_{max}, with a value of 0.01429 mm. This value is determined by the combination of operating parameters and the elasticity of the grinding wheel and workpiece. While there are grain configurations that can withstand penetrations greater than δ_{max}, as many as 90.44% of the grain configurations can result in detachment of grains from the vitreous bonding. To account for this effect, an accumulative damage D has been introduced, which is expressed as the percentage deviation of the critical penetration δ_c (obtained from the μSM) when it does not break in one rotation. A

sensitivity analysis of the model is performed, varying D from 0.1% to 1% with respect to the critical penetration.

Figure 81 displays the comparison between experiments and simulations, including the sensitivity analysis of the accumulative damage D. As mentioned earlier, the model simulates the behavior of the wheel in region 2, without considering region 1 (see Figure 51). The experimental curve is affected by dressing, resulting in a significantly different behavior between both regions. Future research will address the modeling of the dressed region. Therefore, the comparison is limited to the region 2, where the dressed region is not considered.

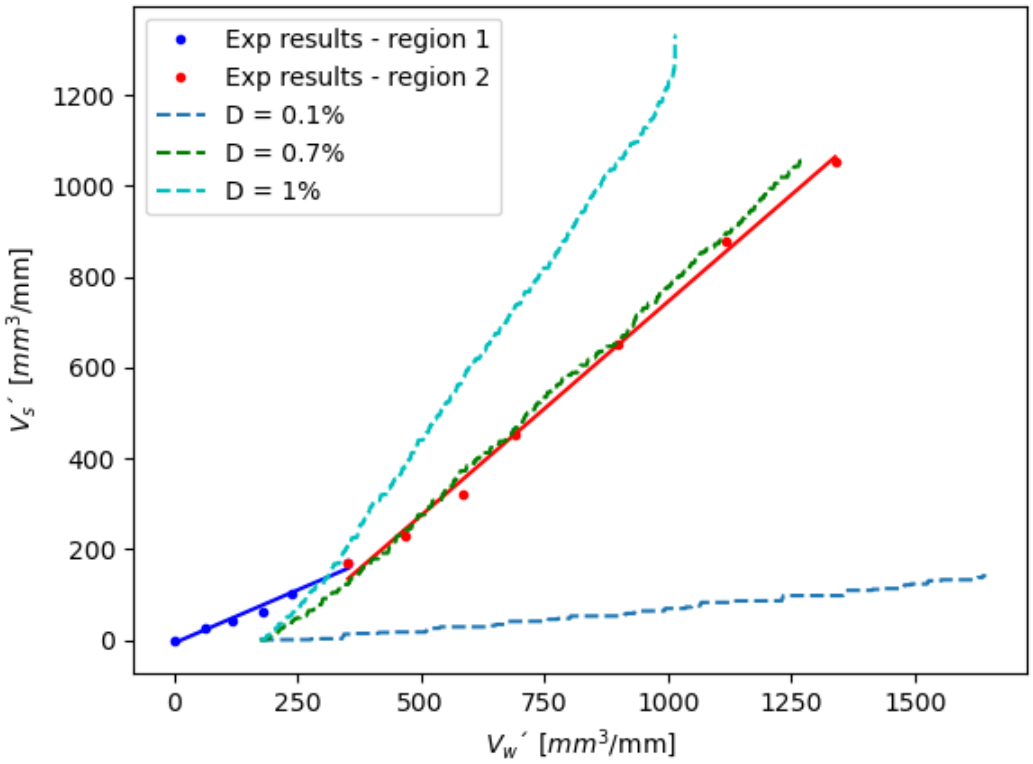

Figure 81. Comparison of wear between multiscale simulations and experiments.

The results demonstrate a high degree of agreement between the experimental and multiscale simulation data, with the best fit achieved at a damage value (D) of 0.7%. At this value, the simulation predicts a G ratio of 1.01, while the experimental data shows a G ratio of 1.09. The maximum deviation in δ_c is 0.1 μm, indicating a good representation of the local effects in grain detachment. Furthermore, the multiscale simulation accurately

captures the volumetric wear behavior of the grinding wheel, as seen in the accumulated radial wear results presented in Figure 82.

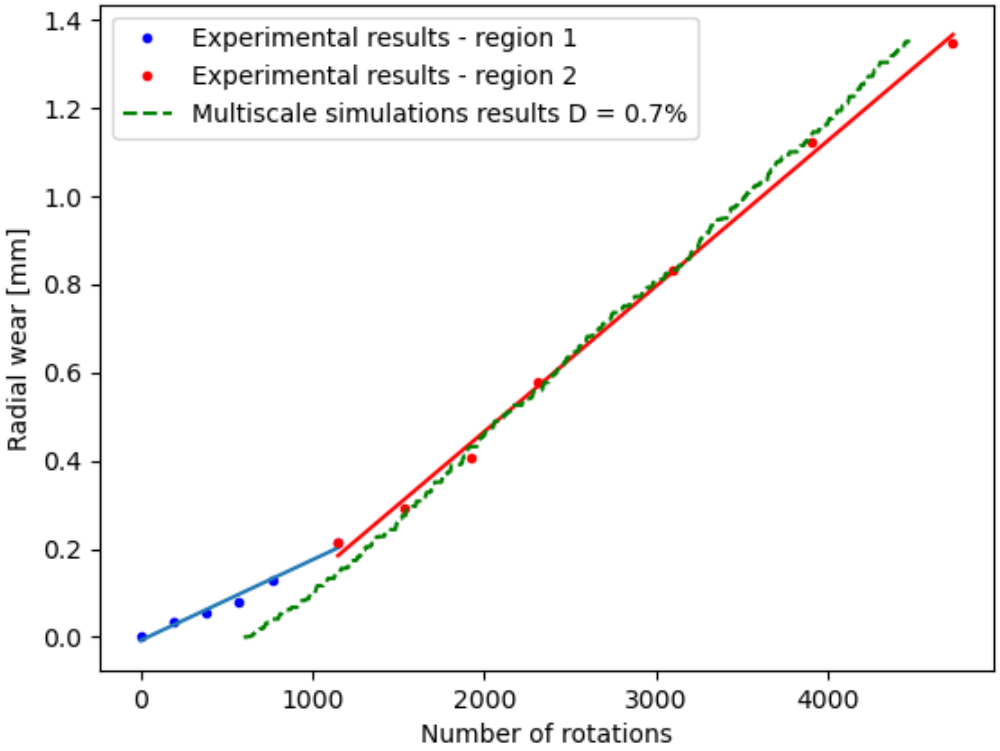

Figure 82. Experimentally measured and simulated radial wear for a value of damage D=0.7%.

Based on the validation outcomes, it can be concluded that the proposed multiscale simulation approach represents an important and novel tool for comprehending the mechanisms of volumetric wear of grinding wheels, incorporating factors such as process parameters, mechanical properties of the wheel, and the stochastic nature of the abrasive grain locations.

4.6 Preliminary conclusions

In conclusion, this study aimed to investigate the causes of volumetric wear on vitrified alumina grinding wheels through experimental and numerical analysis. Based on the obtained results, the following conclusions can be drawn:

- A wear model for vitrified alumina grinding wheels using multiscale simulations has been developed. The combination of the μSM, which employs a cohesive beam model using DEM to represent the mechanical behavior of the grinding wheel, and the RμSM,

which contains complete geometrical information about the abrasive grain locations, allows for accurate reproduction of realistic grinding wheel wear and prediction of the effect of volumetric wear. By adopting this approach, the computational cost is significantly reduced.

- To analyze the behavior of the vitrified bond, it is assumed that the grinding wheel acts as a brittle material in the vitrified bond region. The wear behavior of the μSM is modeled using a maximum micro failure stress of 167 MPa, and the Rankine failure criterion is imposed. Consequently, the 3D cohesive beam model incorporates the Rankine criterion.

- The analysis of μSM wear reveals a mean δ_c of 0.00685 ± 0.0262 mm and a mean N_r of 4.28 ± 16.1. The covariance of 0.0101 indicates a positive relationship between δ_c and N_r, suggesting that an increase in δ_c is likely to result in an increase in N_r. The study also identifies the presence of δ_c values larger than δ_{max}, with approximately 9.56% of values exceeding 0.028 mm. Additionally, up to 29 removed grains are observed.

- Comparison of experimental results of the specific normal force with the μSM results shows that 16.96% of the model's specific normal force falls within the experimental range. However, a larger proportion of forces fall outside the experimental range, with 13% exceeding the range and a higher percentage falling below it. These discrepancies may be attributed to low forces generated in some sections of the wheel in contact. Nevertheless, the μSM demonstrates the capability to simulate grinding forces in a section of the grinding wheel, indicating its reliability and usefulness for predicting and analyzing grinding forces.

- In the hypothesis 1, the assumption of perfectly spherical abrasive grains in the RμSM introduces uncertainty regarding the actual δ_c. To address this, a shape factor S_f is introduced, representing the percentage deviation of the δ_c from the value obtained in μSM. The experimental curve shows a different behavior in the dressing-affected region. The comparison is limited to regions with similar grain density. These results

demonstrate an excellent agreement between the experimental findings in region 2 and the results obtained from the multiscale simulation with an S_f of 6%. Both exhibit a G ratio of 1.09. The 6% deviation from δ_c corresponds to 0.8574 μm, which can be attributed to the micro-cutting of the abrasive grains. The multiscale approach also effectively captures the accumulated radial wear.

- In the hypothesis 2, the presence of certain grains that are resistant to the actual δ_{mac} introduces additional uncertainty. To account for this effect, a damage factor (D) has been introduced, representing the percentage deviation of δ_c. The results of radial wear and G ratio show good agreement between experiments and simulations, with the best fit corresponding to a D value of 0.7%. This value of D yields a G ratio of 1.01 and 1.09 in simulations and experiments, respectively. A damage of 0.7% represents a maximum deviation of 0.1 μm in δ_c, which aligns with the effect of the reduction of the vitrified bond resistant.

- The impact of dressing has not been taken into account. While the presented multiscale approach encompasses a significant amount of required information, further analysis is necessary to examine the influence of dressing parameters on surface grain density, as well as the potential impact of dressing operations on the mechanical strength of bonding bridges. These aspects will be investigated in future research.

- The stochastic nature of abrasive grain location plays a crucial role in volumetric wear on grinding wheels. The distribution and orientation of the abrasive grains can affect the strength of the binder in each grain and therefore influence the wear and removal of the grains during operation.

- From the point of view of the authors, the most relevant scientific advancement is the development of a theoretical framework to explain and predict volumetric wear of vitreous bond alumina grinding wheels. This is relevant achievement taking into account that to the best knowledge of the authors, this is the first attempt to theoretically predict volumetric wear.

- In the multiscale simulation approach, the thermal factor resulting from the contact between the abrasive grains and the workpiece has not been taken into consideration. However, it is important to acknowledge that temperature can potentially impact the properties of the binder. Therefore, in the subsequent chapter, an analysis will be conducted to determine whether there is any influence on volumetric wear.

Chapter 5

Simulation of thermal loading on vitreous bonding bridges of vitrified griding wheel

5.1 Introduction

The previous chapters have primarily focused on studying the volumetric wear of the grinding wheel from an experimental and numerical perspective. The analysis includes examining the occurrence of bond fracture in vitrified alumina grinding wheels during actual grinding processes, as well as conducting multiscale simulations to quantify the volumetric wear under controlled contact conditions. The simulation results provide valuable insights into the behavior of the real grinding process. However, it is important to acknowledge the limitations of the experimental work, particularly with respect to measuring the temperature reached in the vitrified bond.

Due to the short contact time and difficulties in accessing the vitrified bond, it is nearly impossible to directly measure the temperature during tests. Yet, understanding this temperature is crucial because it affects the behavior of the vitrified bond. High temperatures, thermal shock effects, and thermal cycling lead to changes in the properties of the vitrified bond, inducing damage to its structure. Furthermore, determining the extent to which the vitrified bond is affected by the temperature is challenging experimentally. Therefore, a thermal model is required to analyze the thermal field of the grinding wheel at the vitrified bond zone.

Hence, the main objective of this chapter is to gain insight into the thermal behavior of the vitrified bond under real contact conditions during the grinding process. For this study, the vitrified alumina grinding wheel and CBN grinding wheel are analyzed. This is achieved by conducting thermal analyses to determine the temperature in the contact area and within the abrasive grain and vitrified bond. Of particular interest is the distribution of temperature within the vitrified bond.

5.2 Basis of the thermal model

As it is known, a grinding wheel is composed of abrasive grains randomly embedded in a bond material, which also exhibits a certain level of porosity. Reproducing the behavior of an entire grinding wheel is a challenging task, this work focuses on simulating a group of 7 abrasive grains bonded with 11 bonding bridges. In this regard, the use of FEM stands out as the most appropriate method for generating thermal models. It is due to its capability to handle complex geometries, account for material property variations, boundary conditions and adapt to different scenarios. Furthermore, accurately replicating both the structure and surface of the grinding wheel presents its own set of challenges.

Consequently, a transient-state thermal model is developed using ANSYS Mechanical Workbench to simulate the contact between a section of the grinding wheel and the workpiece, where the abrasive grains slide against a hardened steel surface. To build the model's geometry, it is necessary to determine the volume percentages of the various components comprising the wheel. Table 1 presents this data, which has been provided by the manufacturer of the grinding wheel.

To construct the thermal model, the first step involves considering the contact area between each abrasive grain and the workpiece. In this regard, the approach proposed by Malkin and Guo [41] is employed, which assumes that the contact area is a circular spot with a diameter of 0.023 mm. The presence of a circular spot in the surface enables the application of model inputs. This assumption is justified by the fact that the circular spot is significantly smaller than the size of the grain, and ceramics exhibit very low thermal conductivity. Therefore, it can be reasonably assumed that the thermal behavior can be simplified as a 2D problem with minimal error. Consequently, the simplified contact area can be represented as a rectangular shape with a length of 0.023 mm and a width of 0.018 mm. This simplification significantly reduces the computational cost of the model.

To simulate the thermal behavior at the interface between the grinding wheel and the workpiece, an ideal section of the grinding wheel is specifically designed. This approach offers the advantage of reducing the computational cost of the model. In order to simplify the geometry of the grits, they are represented as spheres, as previously mentioned in section 4. Preliminary simulations indicated that the thermal loading primarily affects the local area of contact. Based on this observation, it is decided to simulate a reduced number of grains in contact with the workpiece. In this particular case, only four grains are in contact, and an additional row of grains is included towards the inner part of the wheel. By employing this arrangement, a more computationally efficient model can be obtained without compromising the overall accuracy.

Regarding the bonding bridges between the grains, the approach introduced by Rom et al. [156] is employed. This approach assumes that the geometry of the bonding bridges can be estimated using B-spline curves. By considering the dimensions of the grits and the percentage of vitreous bonding material, an ideal section of the wheel in contact with the surface of the workpiece is designed. This designed section of the wheel, as depicted in Figure 83, serves as the representative geometry for the thermal simulations.

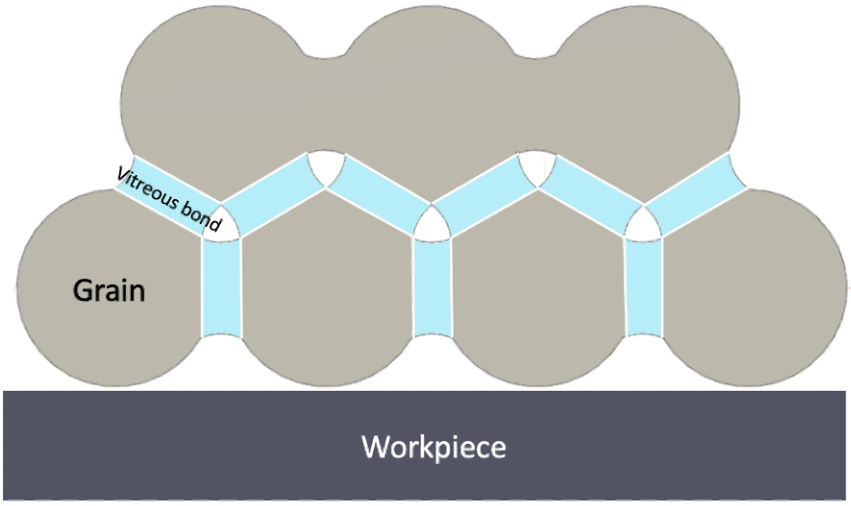

Figure 83. Ideal representation of a portion of the grinding wheel

The total contact area between the grinding wheel and the workpiece is determined by employing the classical formulation, which takes into account the geometric contact length and the Hertz deformations of the two bodies in contact. The determination of the contact length is achieved using Equation (20) as it is mentioned in the Chapter 4. All the data are gathered in Table 8. This equation provides a reliable method for calculating l_c in the context of the grinding process.

Using the theoretical grain density, the researchers calculated the total number of abrasive grains within the contact area, yielding a value of 304 grains. While it is clear that dressing modifies the active grain density [157], the decision is made in this study to simulate the steady-state grinding situation, where the effect of dressing is no longer present. Figure 49 depicts the evolution of the normal grinding force during the experiments and the transition from the transient period related to dressing to the steady-state grinding operation.

With concern to the model inputs, the heat input, the boundary conditions and the material properties are implemented. In the steady-state phase of the experiments, a constant value of specific power is observed in the passes, as illustrated in Figure 48. This value is measured to be 0.18 kW/mm, it implies that the input to the model should be 0.9 kW.

By making the assumption that the heat input is directly proportional to the theoretical chip thickness, a time-dependent function for the heat source can be derived, expressed as:

$$Q(t) = 5.727e^{13} \cdot t \quad (30)$$

Based on this equation, it becomes possible to estimate the energy density that needs to be applied to each individual grain. According to Rowe et al. [158], the percentage of total heat removal by the grinding wheel varies for different materials. For alumina, it ranges from 20% to 35%, while for CBN grains, this value is higher, ranging from 65% to 80% [153] During the grinding process, the presence of coolant facilitates heat transfer through convection when the grinding fluid comes into contact with the abrasive grains. In the case of an oil-in-water emulsion, a convection heat transfer coefficient of h_f = 10000 W/m^{2}K is commonly used for grain-free areas [2]. However, it has been established in the literature that applying this convection coefficient in the model has a negligible impact on the simulation results. Therefore, in subsequent simulations, it is decided not to include convection as a boundary condition in the model.

In addition to the heat flux to the grain and contact time, the properties of alumina and vitrified bond are crucial factors in developing a 2D thermal model. As mentioned earlier, there is limited information available on thermal properties in the scientific literature, and the observed variability must be taken into account. Various values can be found in the bibliography, depending on the temperature of alumina. For instance, at room temperature, reported values for density range from 3900 to 3990 kg/m^3, thermal conductivity from 30 to 40 W/mK, and specific heat of 775 J/kgK [159]. Detailed thermal properties at 200°C can be found in [160]. For this particular model, the properties of alumina at 200ºC are chosen, as shown in Table 9. A comprehensive review of thermal properties for CBN grits is published in the 1990s by Morgan et al. [101], describing a wide range of thermal conductivity values for CBN ranging from 87 W/mK up to 1300 W/mK in the literature, while density and specific heat remain consistent across the reviewed articles. Rowe proposed an effective thermal conductivity value of 290 W/mK. Similar values of density and specific heat for CBN can be found in [161], [162], with significant variations in the reported data for thermal conductivity.

These findings highlight the considerable uncertainty surrounding the thermal properties of grinding wheel components, and obtaining this type of data for the bonding material is even more challenging. To the best of our knowledge, the only reported value of thermal conductivity for a vitreous bond used in the manufacturing of grinding wheels can be found

in [102]. Takezawa proposed a value of 2.85 W/mK for the thermal conductivity of vitreous bonding in grinding wheels, which aligns with other data reported in the general literature for other alumino-alkalisilicate ceramic systems [163]. Some data on SiOC systems can be found in [164], including density (2200 kg/m^3), thermal conductivity (1.35 W/mK), and specific heat (750 J/kgK) at room temperature. Considering the existing uncertainty, the reference values chosen for the simulation are presented in Table 9. Finally, since the model is two-dimensional, it is meshed with two-dimensional quadrilateral elements whose dimension is 0.010 mm. The mesh size will be uniform throughout the geometry.

	Alumina at 200°C [160]	**CBN** [101]	**Vitreous bond** [102]
Density (Kg/m^3)	3900	3480	2640
Conductivity (W/mK)	20	290	2.85
Specific heat (J/KgK)	1046	506	1150

Table 9. Thermal Properties of Alumina Grits, CBN Grits, and Vitrified Bond in Simulations.

5.3 Discussion on numerical simulation of temperature fields

Based on the assumptions mentioned, the simulations are conducted using a 2D transient-state thermal model that considers the contact between the abrasive grit and the workpiece. The primary aim of this model is to gain qualitative insights into the temperature field evolution within the grits and bonding bridges, given the uncertainties surrounding thermal property values. By examining the results obtained from these simulations, this work can lay the basis for more comprehensive investigations into how temperature affects the mechanical properties of vitreous bonds. This research holds the potential to deepen our understanding of the intricate relationship between temperature and the structural behavior of vitreous bonds, leading to valuable insights for future studies.

The study starts by examining the temperature progression within the vitreous bridges, focusing on the use of alumina grains as the subject material. The model incorporated experimental values obtained from section 3. and Figure 84 depicts the temperature field obtained from the simulations. Notably, the highest temperature recorded (2447.9°C) is observed in close proximity to the tip of the grain, rapidly diminishing as it propagated

inward. It should be noted that this numerical value exceeds the melting temperature of fused alumina (2250°C), suggesting a probable overestimation attributable to the assumed spherical shape of the grains in the model.

Upon analyzing the temperature distribution, it becomes evident that the low thermal conductivity of alumina significantly impedes heat conduction towards the vitreous bridges. As a result, the bonding bridges exhibit no temperature deviations from the ambient room temperature, even when the alumina grain reaches its maximum temperature. Therefore, it can be concluded that heat conduction originating from the alumina grains has no discernible impact on the behavior of the vitreous bridges. These findings highlight the limited influence of alumina grain heat conduction on the overall thermal behavior and structural response of the vitreous bridges.

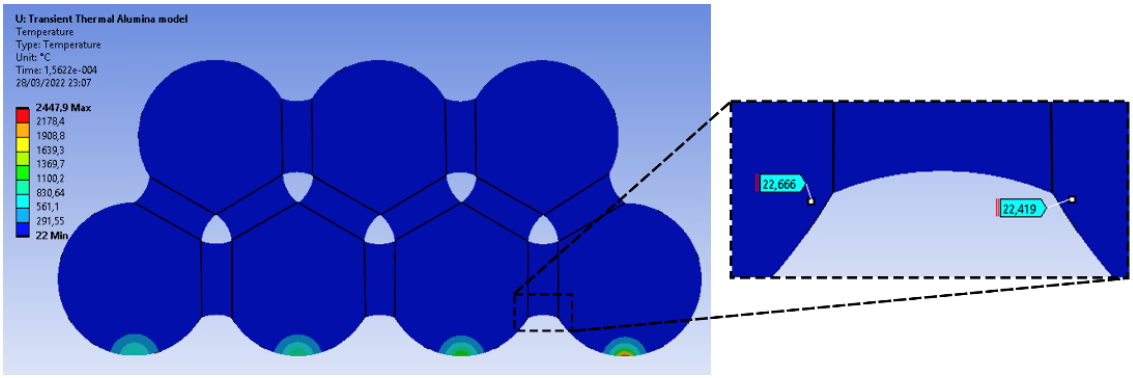

Figure 84. Instantaneous highest temperature field in the model (alumina grains).

Due to the superior thermal conductivity of CBN, the research expanded to simulate the behavior of a vitreous-bonded super-abrasive CBN wheel. In section 5.2, thermal data and heat partition values relevant to this case can be found. To facilitate a meaningful comparison of thermal characteristics, a similar power input is assumed for the model. Figure 85 shows the temperatures within the bonding bridge at the moment when the tip of the CBN grain reaches its highest temperature (789.19°C).

Notably, with the enhanced heat conduction from the grain to the vitreous bond, more effective thermal transfer takes place in the case of CBN. This leads to localized maximum temperatures of 188.28°C in a specific region of the vitrified bond adjacent to the CBN grain. However, it should be emphasized that even with the most conductive CBN grains, the temperatures observed in the vitreous bonding bridges do not reach a level that would

induce any transition in the material properties. To provide further context, it is worth considering the softening temperature of calcium-aluminosilicate glasses [165], which underscores the absence of any significant impact on the vitreous bonding bridges due to heat conduction from the abrasive grain.

Reinforcing this observation, other studies [166] have positioned the softening temperature for aluminosilicate glass at 1010°C. These findings further support the conclusion that heat conduction from abrasive grains, even in the case of highly conductive CBN grains, does not induce any substantial alterations in the behavior or properties of the vitreous bonding bridges.

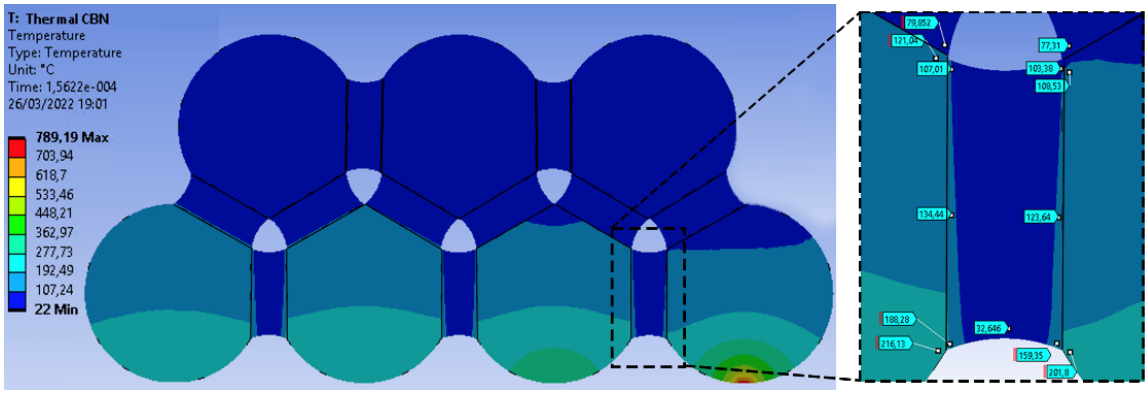

Figure 85. Instantaneous highest temperature field in the model (CBN grains).

As with other ceramic materials, vitreous aluminosilicates used for wheel bonds exhibit brittle behavior and are susceptible to the detrimental effects of thermal shock. A comprehensive evaluation of the performance of various ceramic materials to thermal shock can be found in the study by Li et al [167]. The authors conducted tests and discovered that subjecting alumina ceramic to a single quenching cycle with a temperature gradient of 300°C and a quenching speed (i.e., the time taken to transfer samples into the water tank) ranging from 5 to 15 seconds led to a significant reduction in flexural strength. In fact, the material's flexural strength decreased by approximately 50%, dropping from 300 MPa to 150 MPa. However, for temperature gradients below 300°C, the loss of strength is relatively minimal.

To further evaluate the thermal shock resistance of different ceramic materials, Li et al [167] also introduced the concept of Thermal Shock Resistance Index (TSRI) and assessed

19 ceramic materials accordingly. The TSRI is a metric where higher values indicate better resistance to thermal shock, ranging from 0 to 100. For instance, pure alumina (99% Al_2O_3) exhibited a TSRI of 19, while $3Al_2O_3 \cdot 2SiO_2$ aluminosilicate showed a slightly higher TSRI value of 25.

Considering the thermal gradients observed in the simulations, approximately 188.28°C for CBN grains, within a thermal cycle equivalent to the contact time between the grain and workpiece (1.317 x $10^{\wedge-4}$ s), it can be inferred that the likelihood of thermal shock due to heat conduction from the abrasive grain is extremely limited. These preliminary findings suggest that even in the worst-case scenario, the probability of encountering significant thermal shock resulting from heat transfer from the abrasive grain is highly improbable.

In order to further explore the dynamics at play, this work investigates the impact of a clogged chip from the workpiece in contact with the vitreous bond. Considering the parameters outlined in section 3, the theoretical maximum chip thickness is calculated to be 39 nm. It is important to note that the actual contact length between the chip and the vitreous bond is 3.95 mm. In practical scenarios, the chip may either fracture or become lodged within the porosity between the abrasive grains.

An SEM image depicted in Figure 86 highlights the presence of a clogged steel chip situated between alumina grains and in contact with the vitreous bonding. This visual evidence emphasizes the occurrence of contact occurring between the bond bridge and the machined workpiece, resulting in heat generation at the interface. It is worth noting that wheel manufacturers, such as Norton, have acknowledged the significance of this contact phenomenon. Norton's Vitrium 3® product, for instance, is specifically designed to enhance performance by reducing the interaction between the vitrified bond and the workpiece. This reduction in interaction serves to mitigate heat build-up and minimizes the potential for thermal burns.

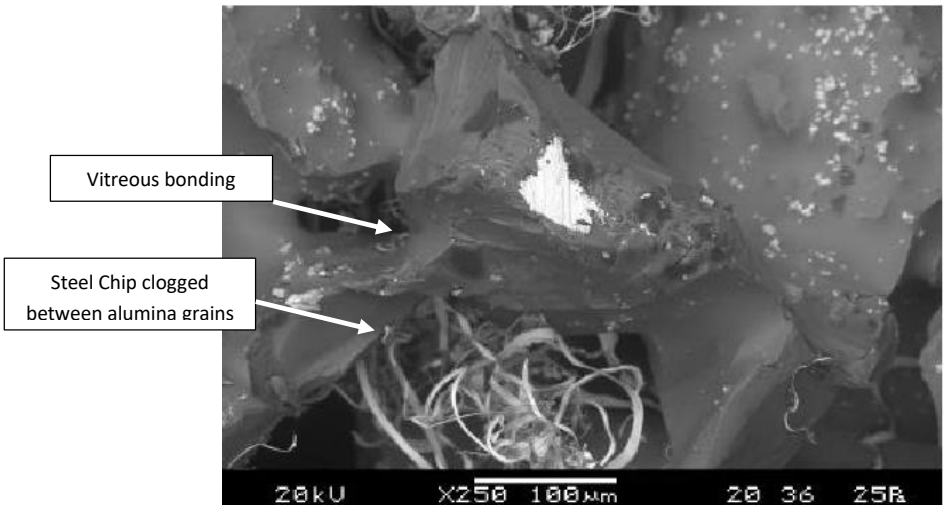

Figure 86. SEM micrograph (x250): Presence of part material (chip) in contact with abrasive grains and bonding material

Considering that chip generation is a dynamic process, the analysis focused on two limiting cases to provide a comprehensive understanding of the problem. These cases aimed to establish the upper and lower limits of the chip behavior. In the first case, it is assumed that the chip remains in contact solely with the abrasive grain and subsequently fractures. For this scenario, a theoretical chip length of 0.108 mm is defined, representing the distance from the tip of the grain to the bonding bridge. In the second case, it is assumed that the chip maintains contact with the entire length of the vitreous bonding bridge, in addition to the abrasive grain, resulting in a chip length of 0.156 mm.

According to Marinescu et al [50], the chip formation energy can be estimated based on the melting temperature of the material. Thus, it is assumed that the chip is removed at the melting temperature, which, in the case of the steel used as the workpiece, is 1410°C [168] As previously mentioned, the contact time between the chip and the abrasive wheel is 1.317 x $10^{\wedge-4}$ seconds, as established in the analysis.

Figure 87 depicts the simulation results for the cases of alumina abrasive grains (upper panels) and CBN abrasive grains (lower panels), considering the minimum chip length of 0.108 mm. In this scenario, the chip does not directly come into contact with the vitreous bond.

For the case of alumina grains, the highest temperature observed in the vitreous bonding reaches 1064°C, precisely at the interface between the abrasive and the vitrified bond. Due to the relatively low thermal conductivity of the vitreous material, most of the bonding bridge does not experience significant overheating, with temperatures remaining below 150°C. Conversely, when CBN grains are employed, the temperature field within the vitreous bridge exhibits steeper gradients, causing the majority of the vitreous material to reach temperatures above 500°C.

As explained earlier, in the case of CBN grains, the steep temperature gradients and elevated temperatures increase the likelihood of softening and thermal shock within the vitreous bond. These thermal effects can lead to damage and compromise the mechanical properties of the bond. It is evident that the choice of abrasive material significantly influences the thermal behavior and potential risks associated with the vitreous bond.

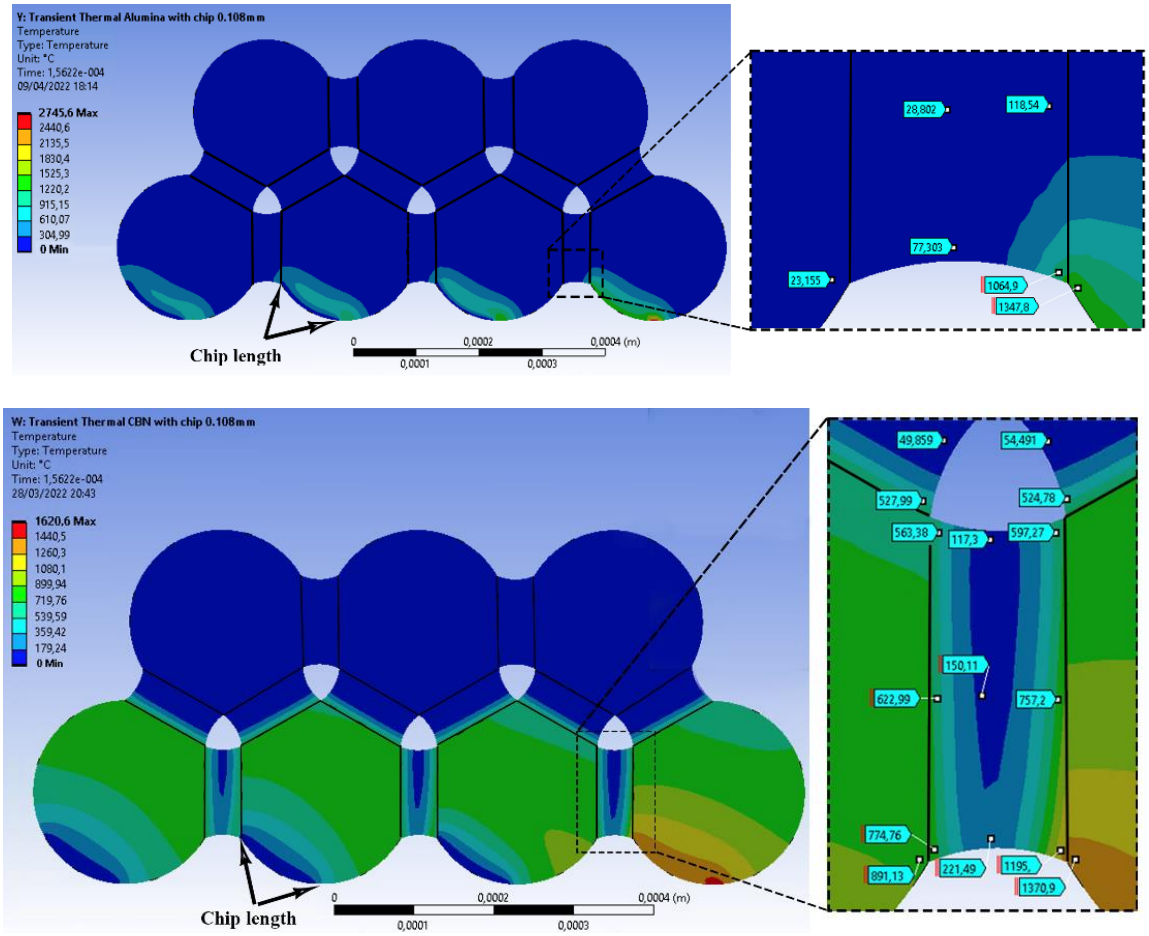

Figure 87. Temperature field in the bonding bridge during the contact time with chip length 0.108 mm. Upper panel: alumina grits; Lower panel: CBN grits.

The influence of chip contact with both the abrasive grain and the bonding bridge becomes more pronounced in the upper boundary analysis, where a chip length of 0.156 mm is assumed. In this scenario, the chip interacts with both components of the abrasive wheel. Figure 88 illustrates the simulation results for both cases, with the upper panel representing alumina grains and the lower panel representing CBN grains.

In both cases, the observed temperatures far exceed the thresholds associated with softening and thermal shock. The temperature distribution within the bonding bridge reaches levels that can significantly compromise its structural integrity and mechanical properties. This indicates that the assumption of chip contact with the bonding bridge has a substantial impact on the thermal behavior of the vitreous bond.

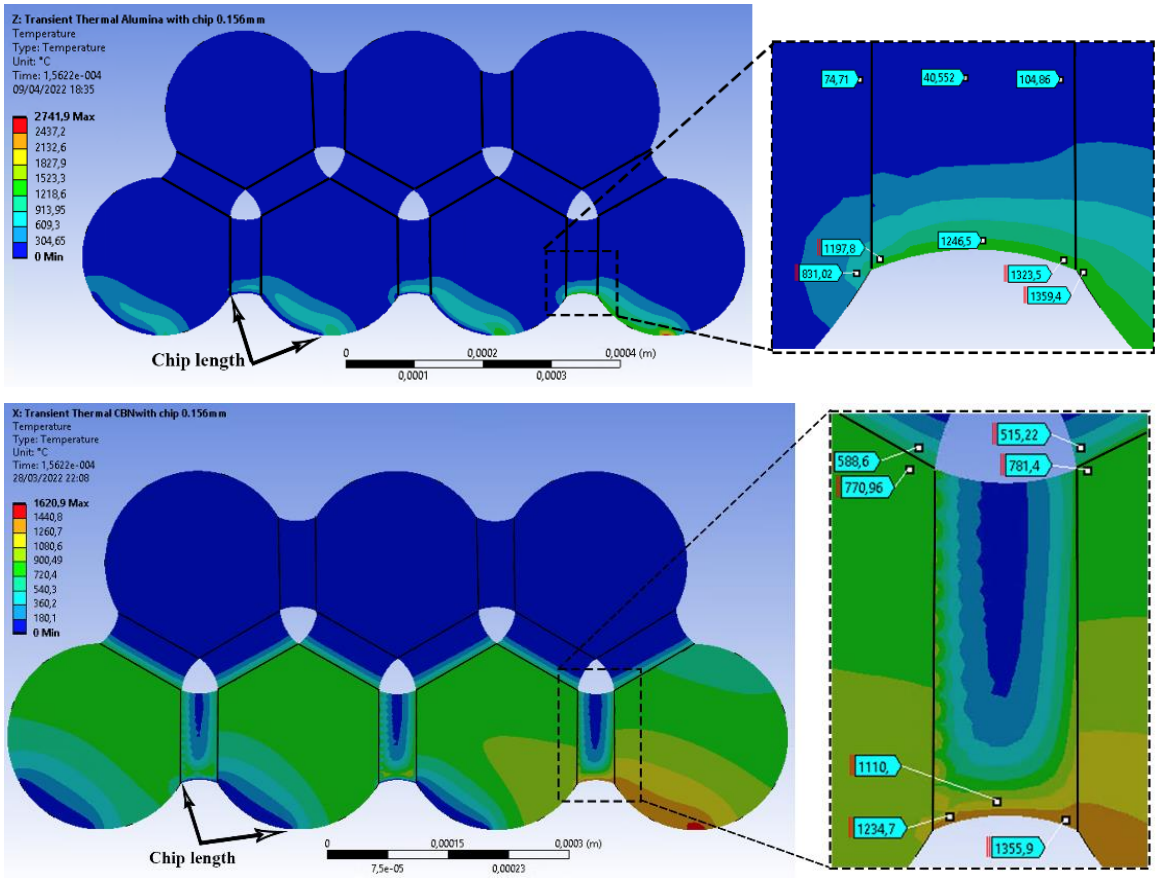

Figure 88. Temperature field in the bonding bridge during the contact time with chip length 0.108 mm. Upper panel: alumina grits; Lower panel: CBN grits.

Despite the aforementioned uncertainties associated with material properties and contact phenomenon, the numerical simulations presented in this study offer valuable qualitative

insights regarding the role of temperature in the mechanical properties of vitreous bonds. While these results should be interpreted as qualitative rather than quantitative, they provide indirect evidence supporting the consideration of temperature effects in the study of vitreous bonds.

It is worth noting that, as far as is known, no experimental studies have yet investigated the influence of temperature on vitreous bond behavior. Consequently, further research in this area is warranted to gain a more comprehensive understanding of the thermal impact on the mechanical properties of vitreous bonds.

By acknowledging the importance of temperature in the performance and reliability of vitreous-bonded systems, future studies can delve deeper into this aspect and design experimental investigations to validate and complement the findings obtained through numerical simulations. Such research endeavors will contribute to advancing the understanding of vitreous bonds and guide the development of improved bonding materials and manufacturing processes.

5.4 Preliminary conclusions

The current chapter introduces a comprehensive 2D finite element thermal model designed specifically for analyzing the behavior of a vitrified alumina grinding wheel. The model takes into account the arrangement of 7 abrasive grains connected by 11 bonding bridges. Through the application of this thermal model, several significant conclusions regarding the vitrified alumina grinding wheel can be drawn:

- The current understanding of the thermal-mechanical behavior and fracture mechanisms of vitrified bonds in abrasive grinding wheels is still limited. While mechanical tests such as bending, compression, and sonic testing have been commonly used to assess the mechanical properties of wheel materials, there is a scarcity of information regarding their thermal properties. The existing literature has provided mixed results, leaving important questions unresolved. The influence of high temperatures, thermal shock effects, and thermal cycles on the integrity of vitreous bonds remains largely unexplored. Despite the general acceptance that these factors can lead to damage in the wheel structure, little attention has been given to estimating their specific impact on vitreous bonds.

- The simulation results highlight that heat conduction from abrasive grains plays a negligible role in the temperature distribution within vitreous bonds. This observation holds true for both alumina and CBN grains, even though CBN grains possess a higher thermal conduction coefficient. In both cases, the temperatures observed in the bonding material are significantly lower than the thresholds reported in previous studies for softening and thermal shock in aluminosilicates.

- Numerical simulations are conducted to investigate the transient heat conduction problem arising from the contact between part chip material and the wheel structure. Two boundary cases representing different contact stages are analyzed, and the resulting thermal fields are calculated. The findings demonstrate that, for both alumina and CBN grit materials, the temperatures observed exceeded the thresholds associated with softening and thermal shock. In the case of alumina, this effect is localized in the contact region, whereas for CBN, the combination of heat conduction through the grains and contact with the part material led to significantly elevated temperatures, surpassing 500°C. Consequently, softening, thermal shock, and consequent damage to the bond's mechanical properties are likely to occur. These results highlight the need for further research in the development of characterization tests that take into account the thermal-mechanical behavior of vitreous bonds.

- To advance the knowledge in this field, further research is needed to investigate the thermal-mechanical behavior of vitrified bonds and the causes of bond fracture. It is crucial to develop experimental methods and testing protocols that specifically address the thermal properties of vitreous bonds.

- While the simulation results provide valuable insights into the thermal characteristics of vitreous bonding, it is important to acknowledge the inherent limitations and uncertainties of the modeling approach. Future experimental studies are needed to validate these findings and explore the thermal behavior of vitreous bonds under real-world grinding conditions.

Chapter 6

Conclusions and future works

6.1 Conclusions

The research work conducted in this study involved both experimental and numerical analyses. The experimental analysis focused on real grinding tests, and the following key conclusions are drawn:

- Extensive examination of bond fracture evolution in vitrified alumina grinding wheels involves isolating and studying this effect during real grinding tests. This isolation enables investigating the influence of grinding wheel hardness, structure and grinding parameters on bond fracture evolution.

  - In the experimental analysis conducted, two distinct zones are clearly identified in the test results, namely the dressing zone and the non-dressing zone. It is observed that the volumetric wear exhibited a linear increase in both of these zones, although with different slopes.

- The higher values of certain grinding parameters, such as a depth of cut of 0.036 mm and a cutting speed of 30 m/s, exhibited a clear tendency towards volumetric wear. However, it should be noted that this tendency is observed when using a low hardness grinding wheel, specifically a grade of hardness EF. For a more comprehensive understanding of power and grinding forces, a moderate value of 0.25 m/s for the workpiece speed in grinding operations is chosen.

- The maximum specific volumetric wear measured is 1054.22 mm^3/mm for a grinding wheel after removing 1338.92 mm^3/mm of material. Finally, grinding ratio of 1.09 is obtained.

- The surface of the grinding wheel is intentionally designed to facilitate volumetric wear. This is achieved by using a fine dressing process with a high overlap ratio of 7.33. It is important to note that finer dressing with a multi-point dresser, combined with a lower hardness of the wheel with higher grade of monocrystalline structure grain can result in increased bond fracture.

- Analyzing the wheel surface is crucial to assess the occurrence of wear flats, which exhibit a low rate of only 0.27% during experimental testing. This indicates that the grinding process, combined with the chosen grinding parameters, grinding wheel hardness and structure, grade of monocrystalline structure and dressing techniques, effectively minimizes the formation of wear flats on the wheel surface.

- The established methodology for quantifying radial wear on grinding wheels has provided valuable insights. The maximum radial wear measured during the experimental testing reached 1.34 mm. This quantification is essential for determining the grinding ratio, a critical parameter in evaluating the volumetric wear of the grinding wheel.

- Given the limitations of the experimental work, two numerical approaches are developed to enhance the understanding of the underlying phenomenon. The first model is a multiscale simulation approach that investigates the impact of volumetric wear in vitrified alumina grinding wheel during the grinding process. The second model focuses on the temperature distribution at the contact between the abrasive

grain and the workpiece in vitrified alumina and CBN grinding wheel, as well as its influence on the vitrified bond. The key findings derived from these numerical approaches are outlined below:

- Experimental tests of grinding wheel surfaces can only analyze the initial and final states. Furthermore, the influence of the strength of the binder on volumetric wear is shown. To overcome these handicaps, a multiscale simulation approach of the vitrified alumina grinding wheel is developed using DEM. A methodology based on DEM has been shown. The multiscale simulation approach provides the following main findings:

    - DEM has been widely recognized as an exceptional tool for modeling grinding wheels. It enables the accurate representation of randomly located grains, closely resembling real-world scenarios, while also providing an understanding of their stiffness characteristics. This unique capability of DEM allows for a more realistic simulation of the grinding process, capturing the complex interactions between the grains and the workpiece. By incorporating random grain location and accurately modeling stiffness, DEM enhances our ability to study and analyze grinding wheels, facilitating improved insights into their performance and behavior.

    - DEM is employed to create a comprehensive multiscale simulation approach of a vitrified alumina grinding wheel. In this approach, the cohesive beam model is used to accurately represent the continuous material within the DEM framework. The discrete elements represent the abrasive grains and the elastic beam represents the vitreous bond. Given the brittle nature of the grinding wheel, the Rankine´s theory is imposed as the beam failure criteria. This ensures that the simulation effectively captures the wheel's response to stress and potential fracture. Additionally, the DEM approach demonstrates its capability to replicate the wear of the vitrified alumina grinding wheel by accurately simulating the bond fracture phenomenon.

- To incorporate the real cutting speed of 30 m/s into the wear model, a tangential force is applied to the DEs that come into contact with the workpiece. This force is determined based on the desired cutting speed, which in this case is represented by the coefficient of friction $\mu_\mu = 0.37$. By imposing this value, the model effectively represents the cutting speed of 30 m/s, ensuring accurate simulation of the wear process.

- The hypothesis of simulating uSM and RuSM interactions to analyze volumetric wear and the behavior of the vitrified bond in the contact region has been verified. By adopting this approach, a significant reduction in computational cost is achieved compared to simulating the complete grinding wheel.

- In order to ensure consistent grain density in both DEM and Python, it is important to maintain uniformity throughout the section in DEM and the entire grinding wheel in Python. By default, when creating the μSM and RμSM, there is a tendency for the boundaries to have excessive protruding grains or defective grains respectively, especially at the surface where a cut is made. These irregularities can affect the accuracy and reliability of the approaches. Therefore, it is necessary to address this issue and strive for a better and clearer representation of the grain density in both DEM and Python.

- The primary advantage of simulating the volumetric wear of the vitrified alumina grinding wheel is the ability to understand the progressive generation of bond fractures in the contact area between the abrasive grain and the workpiece. In experimental tests, only the final state (experimental test block) of the grinding wheel can be analyzed. However, through the application of multiscale simulation approach, it becomes possible to study the entire evolution of volumetric wear, from the initial contact to its conclusion.

- Two hypotheses were formulated, demonstrating a strong correlation between the experimental findings in region 2 and the obtained results. Firstly, the mechanical behavior of the binder was updated as the grinding wheel wears with a shape factor of the grains of 6%. This update aimed to

accurately capture the changes in the critical penetration in the grains due to wear, ensuring a more realistic representation of the grinding process. Secondly, the possibility of cumulative damage to the binder was taken into consideration, assuming a damage rate of 0.7% per rotation as the grinding wheel wears. This hypothesis accounted for the potential degradation of the binder over time, leading to a more comprehensive understanding of its long-term performance. By considering both hypotheses, a better and clearer understanding of the grinding wheel's behavior and performance was achieved, aligning closely with the experimental observations in region 2.

- A 2D FEM thermal model is developed, incorporating the heat flux data obtained from theoretical calculations and experimental measurements during the contact between the grinding wheel and the workpiece. Moreover, the boundary conditions are appropriately imposed to accurately represent the thermal behavior of the system. The main conclusions derived from the thermal model are summarized as follows:

    - The distribution of temperatures within the vitrified bond was found to be approximately 22ºC for alumina and around 188ºC for CBN. This observation suggests that heat conduction from the abrasive grains has a negligible impact on the temperature fields within the vitreous bonding. This holds true for both alumina and CBN grains, despite their higher thermal conduction coefficients. Importantly, the temperatures recorded in the bond are considerably lower than the values reported in literature for softening and thermal shock in aluminosilicates. Hence, the results indicate that the vitrified bond effectively maintains lower temperatures, ensuring the stability and integrity of the material.

    - Furthermore, the numerical simulation was performed to address the issue of transient heat conduction resulting from the contact between the chip material and the wheel structure. The simulation results reveal that the observed temperatures for both grit materials were significantly higher compared to the temperatures associated with softening and thermal shock. In the case of

alumina, this effect is localized in the contact region. However, for CBN, the primary factor contributing to the vitreous bonding is the combination of heat conduction through the grains and contact with the chip material, resulting in temperatures surpassing 500°C. Consequently, in this scenario, the occurrence of softening and thermal shock is probable, and the mechanical properties of the bond may also be adversely affected due to the thermal impact.

6.2 Future works

Based on the conclusions drawn from the presented research work, the following future research directions have been identified:

- The multiscale simulation approach developed in this study is tailored to the characteristics of vitrified alumina grinding wheels. However, due to versatility of the approach, future research aims to extend its application to other types of abrasives, encompassing diverse abrasive grain sizes, bond grades, and structures. This adaptability allows the multiscale simulation approach to be used in various grinding scenarios and with different materials as long as the bond fracture phenomenon predominates. As a result, valuable insights into the grinding process can be gained across a wide range of applications, enabling a deeper understanding of the behavior of grinding wheels in different contexts.

- One important aspect to consider in future research is the characterization of the shape factor of abrasive grains with different shapes. In the present study, spherical shapes are considered for the abrasive grains. However, in actual grinding wheels, abrasive grains can have varying shapes throughout the wheel. Therefore, it is crucial to analyze the volumetric wear behavior of the grinding wheel based on the shape of the abrasive grains. From a numerical point of view, GranOO offers the capability to detect contact between DEs with different shapes. This feature enables wear modeling of grinding wheels, incorporating the realistic shapes of the abrasive grains in both the actual grinding process and the numerical simulation. By aligning the shapes in the simulation with those observed in real-world scenarios, a more accurate

representation of wear behavior can be achieved, leading to improved understanding and predictive capabilities in grinding wheel analysis.

- A crucial future research goal is to develop a realistic multiscale simulation approach for vitrified alumina grinding wheels. The current work focuses solely on simulating volumetric wear at the initial stage and does not take other types of wear into account. Therefore, it is essential to expand the uSM and RuSM to include grain fracture and wear flats, aiming for a more comprehensive representation of grinding wheel wear. To achieve this, groups of DEs could be defined within the abrasive grains. The behavior of the beams within these defined groups would be distinct from the behavior between groups, simulating the three wear mechanisms in the grinding wheel. By incorporating these additional wear mechanisms, the multiscale simulation approach becomes more realistic, reflecting the complex nature of abrasive grain degradation during grinding operations. This enhanced multiscale simulation approach would provide a more accurate simulation of the wear behavior of vitrified alumina grinding wheels, improving the understanding of wear mechanisms and aiding in the development of more effective grinding processes.

- The idea is to improve the clarity and precision of this work by refining the multiscale approach. Currently, the focus lies on simulating the behavior of the wheel in region 2, without considering region 1 (see Figure 51). It is evident from the experimental curve that the behavior of the dressed region differs significantly. As a result, the plan is to investigate the modeling of the dressed region in future studies, aiming to develop a more comprehensive and accurate representation.

- Development of software for automated quantification of volumetric wear in vitrified alumina grinding wheels. A software tool should be developed to accurately measure the radial wear and quantify the volumetric wear in grinding wheels automatically. This software would expedite the analysis process and provide precise data on the volumetric wear characteristics. Additionally, implementing this software in an industrial setting would enhance productivity in post-grinding operation analysis.

- In future works, it is suggested to conduct a comprehensive comparison of the topography between a specific section of the grinding wheel and μSM area using

SEM analysis. This analysis will provide a detailed assessment of the degree of concordance or agreement between the two surface topographies at the conclusion of the test.

- Incorporating the workpiece as a degradable body is an essential consideration when using the DEM for modeling grinding wheels. By accounting for the degradability of the workpiece, a more accurate estimation of surface roughness can be obtained as a result of the grinding process.

Nomenclature

a_e	real depth of cut (mm)
a_{ed}	dressing depth of cut (mm)
b_s	width of contact (mm)
d_e	grinding wheel diameter (mm)
d_g	average grain diameter (mm)
d_{gmax}	maximum grain diameter (mm)
d_{gmin}	minimum grain diameter (mm)
DEs	spherical discrete elements
DEM	discrete element method
e_c	specific grinding energy (J/mm^3)
E^*	combined elastic properties of the grinding wheel and workpiece (GPa)
E_s, E_μ	grinding wheel and beam Young modulus (GPa)
f_{cj}	centrifugal force in each DE (N)
F_n, F_t	normal and tangential grinding force (N)
	tangential grinding force (N)
F_n', F_t'	normal and tangential grinding force per unit width (N/mm)
$F_{n\,new}'$	new normal grinding force per unit width (N/mm)
F_p	fluid pressure (bar)
$F_{t\,new}'$	new tangential grinding force per unit width (N/mm)
G	grinding ratio

h_f	convection heat transfer coefficient of grinding fluid (W/m^{2}K)
h_s	height of microscale model (mm)
K	contact stiffness (N/m)
l_c	contact length (mm)
l_f	dynamic contact length (mm)
l_g	geometrical contact length (mm)
L_μ	beam length in DEM (mm)
m	grinding wheel mass (Kg)
m_j	mass of each DE (Kg)
M	sieve number
$N_{r\,new}, N_r$	new number and number of discrete elements removed
P'	specific power (KW/mm)
Q_w'	specific metal removal rate (mm^3/mm·s)
q_s	velocity ratio
r_j	distance from the center of each DE to the center of the wheel (mm)
r_μ	ratio between cohesive beam radius and average DE radius
R_j	distance from the outermost grain to the center of the $R\mu SM$ (mm)
R_r	roughness factor
R_w	partition ratio of heat to the workpiece
$R\mu SM$	randomization of the μSM
S_f	grain shape factor
U_d	dressing overlap
v_d	dressing axial feed (mm/min)
V_b	vitreous bond volumetric fraction (%)
V_g	abrasive volume fraction (%)
V_p	porosity volume (%)

v_s	cutting speed (m/s)
V'_s	specific volumetric wear (mm^3/mm)
v_w	work speed (m/s)
V'_w	specific volume of metal removed (mm^3/mm)
w	grinding width (mm)
WP_{new}, WP	new and workpiece position (mm)
δ_{av}	average grit penetration (mm)
δ_{cnew}, δ_c	new and critical grit penetration (mm)
δ_{max}	maximum grit penetration (mm)
υ_s, υ_μ	grinding wheel and beam poisson ratio
Δ	radial wear (mm)
σ	normal tension of beams in DEM (MPa)
τ	tangential tension of beams in DEM (MPa)
ρ	grinding wheel density (Kg/m^3)
$\sigma_f, \sigma_{f\mu}$	grinding wheel and DEM beam failure stress (MPa)
μ	friction coefficient
μSM	microscale model
ω	rotational speed of the grinding wheel (rad/s)

References

[1] F. Hashimoto *et al.*, "Abrasive fine-finishing technology," *CIRP Ann Manuf Technol*, vol. 65, no. 2, pp. 597–620, 2016, doi: 10.1016/j.cirp.2016.06.003.

[2] S. Malkin and C. Guo, *Grinding Technology: Theory and application of machinning*, Second Edi. New York: Industrial Press Inc., 2008.

[3] I. Marinescu, M. Hitchiner, E. Uhlmann, W. Rowe, and I. Inasaki, *Handbook of machining with grinding wheels*, vol. 66. Palm Beach, Florida: Taylor & Francis Group, LLC, 2006. doi: 10.1201/9781420017649.

[4] M. Shaw, *Principles of abrasive processing*. Oxford: Oxford University Press, 1996.

[5] Q. Miao, W. Ding, W. Kuang, and J. Xu, "Tool wear behavior of vitrified microcrystalline alumina wheels in creep feed profile grinding of turbine blade root of single crystal nickel-based superalloy," *Tribol Int*, vol. 145, no. December 2019, p. 106144, 2020, doi: 10.1016/j.triboint.2019.106144.

[6] G. Guerrini, F. Lerra, and A. Fortunato, "The effect of radial infeed on surface integrity in dry generating gear grinding for industrial production of automotive transmission gears," *J Manuf Process*, vol. 45, no. March, pp. 234–241, 2019, doi: 10.1016/j.jmapro.2019.07.006.

[7] W. Zhou, J. Tang, and W. Shao, "Study on surface generation mechanism and roughness distribution in gear profile grinding," *Int J Mech Sci*, vol. 187, no. March, p. 105921, 2020, doi: 10.1016/j.ijmecsci.2020.105921.

[8] Nuclear Power, "Turbine Blades," https://www.nuclear-power.com/nuclear-power-plant/turbine-generator-power-conversion-system/what-is-steam-turbine-description-and-characteristics/turbine-blades/.

[9] shutterstock, "Gear shaft with splines on a white background, 3D illustration.," https://www.shutterstock.com/es/image-illustration/gear-shaft-splines-on-white-background-1569033430.

[10] Renishaw, "nozzle guide vane ," https://www.renishaw.com/en/50-faster-turbine-blade-inspection--43200.

[11] E. Carlos Bianchi, P. Roberto de Aguiar, R. Daun Monici, L. Daré Neto, and L. Roberto da Silva, "Analysis of the Performance of Superabrasive and Alumina grinding wheels with Different Bonds and Machining Conditions," 2003.

[12] A. K. Singh, A. Kumar, V. Sharma, and P. Kala, “Sustainable techniques in grinding: State of the art review,” *J Clean Prod*, vol. 269, p. 121876, 2020, doi: 10.1016/j.jclepro.2020.121876.

[13] N. S. Qu, Q. L. Zhang, X. L. Fang, E. K. Ye, and D. Zhu, “Experimental Investigation on Electrochemical Grinding of Inconel 718,” *Procedia CIRP*, vol. 35, pp. 16–19, 2015, doi: 10.1016/j.procir.2015.08.055.

[14] EMAG Ltda, “Customised grinding of transmission shafts with modular components,” *Grinding and Surface finishing*, vol. 155, no. 2, UK, p. 22, 2019. doi: 10.1016/j.ajodo.2018.11.007.

[15] A. K. Singh, A. Kumar, V. Sharma, and P. Kala, “Sustainable techniques in grinding: State of the art review,” *J Clean Prod*, vol. 269, p. 121876, 2020, doi: 10.1016/j.jclepro.2020.121876.

[16] S. Ravi and P. Gurusamy, “Role of cryogenic machining: A sustainable manufacturing process,” *Mater Today Proc*, no. xxxx, 2020, doi: 10.1016/j.matpr.2020.05.276.

[17] Z. W. Zhong and V. C. Venkatesh, “Recent developments in grinding of advanced materials,” *International Journal of Advanced Manufacturing Technology*, vol. 41, no. 5–6, pp. 468–480, 2009, doi: 10.1007/s00170-008-1496-3.

[18] E. Weingärtner, S. Jaumann, F. Kuster, and K. Wegener, “On-machine wire electrical discharge dressing (WEDD) of metal-bonded grinding wheels,” *International Journal of Advanced Manufacturing Technology*, vol. 49, no. 9–12, pp. 1001–1007, 2010, doi: 10.1007/s00170-009-2458-0.

[19] B. B. Miller and S. Ungewiss, “Grinding Large Module Gears,” *An ever-increasing range of grinding applications from Kapp/Niles are geared toward achieving lower noise, longer service life, and improved performance.*, pp. 34–45, 2010.

[20] R. Lizarralde, D. Barrenetxea, I. Gallego, J. I. Marquinez, and R. Bueno, “Practical application of new simulation methods for the elimination of geometric instabilities in centerless grinding,” *CIRP Ann Manuf Technol*, vol. 54, no. 1, pp. 273–276, 2005, doi: 10.1016/S0007-8506(07)60101-2.

[21] R. Cai, W. B. Rowe, J. L. Moruzzi, and M. N. Morgan, “Intelligent grinding assistant (IGA(©)) - System development part i intelligent grinding database,” *International Journal of Advanced Manufacturing Technology*, vol. 35, no. 1–2, pp. 75–85, 2007, doi: 10.1007/s00170-006-0702-4.

[22] A. Zahedi and B. Azarhoushang, “FEM Based Modeling of Cylindrical Grinding Process Incorporating Wheel Topography Measurement,” *Procedia CIRP*, vol. 46, pp. 201–204, 2016, doi: 10.1016/j.procir.2016.03.179.

[23] K. Wegener, F. Bleicher, P. Krajnik, H. Hoffmeister, and C. Brecher, “Recent developments in grinding machines,” *CIRP Ann Manuf Technol*, vol. 66, no. 2, pp. 779–802, 2017, doi: 10.1016/j.cirp.2017.05.006.

[24] C. Forbrigger, A. Warkentin, and R. Bauer, “Improving the performance of profile grinding wheels with helical grooves,” *International Journal of Advanced Manufacturing Technology*, vol. 97, no. 5–8, pp. 2331–2340, Jul. 2018, doi: 10.1007/s00170-018-2098-3.

[25] Z. Zhao, N. Qian, W. Ding, Y. Wang, and Y. Fu, "Profile grinding of DZ125 nickel-based superalloy: Grinding heat, temperature field, and surface quality," *J Manuf Process*, vol. 57, pp. 10–22, Sep. 2020, doi: 10.1016/j.jmapro.2020.06.022.

[26] W. B. Rowe, "Modern Grinding Technology and Systems." [Online]. Available: www.mdpi.com/journal/inventions

[27] B. Denkena, L. de Leon, and B. Wang, "Grinding of microstructured functional surfaces: A novel strategy for dressing of microprofiles," *Production Engineering*, vol. 3, no. 1, pp. 41–48, 2009, doi: 10.1007/s11740-008-0134-0.

[28] Wikipedia, "Turbine_blade," https://en.wikipedia.org/wiki/Turbine_blade.

[29] G. T. Smith, "Cutting Tool Technology," in *CNC Machining Technology*, London: Springer London, 1993, pp. 1–65. doi: 10.1007/978-1-4471-2053-7_1.

[30] ANSI B74.2, "Specifications for shapes and sizes of grinding wheels and for shapes, sizes and identification of mounted wheels," 2003. [Online]. Available: www.pipefittingweb.com

[31] globalspec, "Grinding Wheels Specifications," https://www.globalspec.com/specsearch/searchform/materials_chemicals_adhesives/abrasives_abrasive_products/grinding_wheels.

[32] B. Yastikci, "INVESTIGATION OF TOOL WEAR IN GRINDING PROCESSES," 2016.

[33] Lyn Borchert, "What to know about Diamond Dressers," https://irontite.com/a/36-what-to-know-about-diamond-dressers.

[34] J. Yang, H. Zhang, T. Li, Z. Gao, S. Nie, and B. Wei, "A profile dressing method for grinding worm used for helical gear with higher order modification profile," *International Journal of Advanced Manufacturing Technology*, vol. 99, no. 1–4, pp. 161–168, Oct. 2018, doi: 10.1007/s00170-018-2459-y.

[35] Walter Graf, "DRESSING OF GRINDING WHEELS," https://www.linkedin.com/pulse/dressing-grinding-wheels-walter-graf.

[36] Walter Graf, "Profile Grinding Large Diameter Gears," https://www.linkedin.com/pulse/profile-grinding-large-diameter-gears-walter-graf.

[37] Z. Zhao, N. Qian, W. Ding, Y. Wang, and Y. Fu, "Profile grinding of DZ125 nickel-based superalloy: Grinding heat, temperature field, and surface quality," *J Manuf Process*, vol. 57, no. January, pp. 10–22, 2020, doi: 10.1016/j.jmapro.2020.06.022.

[38] E. Saljé, H.-H. Damlos, and H. Teiwes, "Problems in Profile Grinding — Angular Plunge Grinding and Surface Grinding," *CIRP Annals*, vol. 30, no. 1, pp. 219–222, 1981, doi: 10.1016/S0007-8506(07)60929-9.

[39] E. Rouly, A. Warkentin, and R. Bauer, "Design and testing of low-divergence elliptical-jet nozzles," *Journal of Mechanical Science and Technology*, vol. 29, no. 5, pp. 1993–2003, May 2015, doi: 10.1007/s12206-015-0420-7.

[40] C. Forbrigger, R. Bauer, and A. Warkentin, “A review of state-of-the-art vitrified bond grinding wheel grooving processes,” *International Journal of Advanced Manufacturing Technology*, vol. 90, no. 5–8, pp. 2207–2216, May 2017, doi: 10.1007/s00170-016-9546-8.

[41] S. Malkin and C. Guo, “Grinding technology-theory and applications of machining with abrasives,” *Tribol Int*, vol. 23, no. 6, p. 443, Dec. 1990, doi: 10.1063/01.2717084.

[42] P. Gómez González and S. José Antonio, “CARACTERIZACIÓN Y SIMULACIÓN DEL COMPORTAMIENTO MECÁNICO DE AGLOMERANTES VÍTREOS PARA MUELAS DE RECTIFICADO DE ALÚMINA,” 2022.

[43] X. Sun, T. Yu, Y. Chen, C. Zhang, and Z. Ma, “Effect of cobalt on properties of vitrified bond and vitrified cubic boron nitride composites,” *Ceram Int*, vol. 46, no. 4, pp. 5337–5343, 2020, doi: 10.1016/j.ceramint.2019.10.286.

[44] X. Sun, T. Yu, X. Wang, M. Xu, and W. Wang, “Effect of TiO2 addition and high magnetic field sintering on properties of vitrified bond CBN composites,” *Ceram Int*, vol. 44, no. 14, pp. 16307–16313, 2018, doi: 10.1016/j.ceramint.2018.06.030.

[45] S. peng Chen, X. pan Liu, L. Wan, P. zhao Gao, W. Zhang, and Z. qiang Hou, “Effect of V2O5 addition on the wettability of vitrified bond to diamond abrasive and grinding performance of diamond wheels,” *Diam Relat Mater*, vol. 102, no. August 2019, p. 107672, 2020, doi: 10.1016/j.diamond.2019.107672.

[46] T. Pazmino, I. Pombo, J. A. Sanchez, and L. Godino, “Caracterización experimental del desgaste radial de muelas de rectificado con aglomerante vítreo,” in *Revista Iberoamericana de Ingenieria Mecanica*, 2021, pp. 1–11.

[47] D. Herman and J. Krzos, “Influence of vitrified bond structure on radial wear of cBN grinding wheels,” *J Mater Process Technol*, vol. 209, no. 14, pp. 5377–5386, 2009, doi: 10.1016/j.jmatprotec.2009.03.013.

[48] K. Wegener, H.-W. Hoffmeister, B. Karpuschewski, F. Kuster, W.-C. Hahmann, and M. Rabiey, “Conditioning and monitoring of grinding wheels,” *CIRP Annals*, vol. 60, no. 2, pp. 757–777, 2011, doi: 10.1016/j.cirp.2011.05.003.

[49] A. A. Khangar, E. A. Kenik, and N. B. Dahotre, “Microstructure and microtexture in laser-dressed alumina grinding wheel material,” *Ceram Int*, vol. 31, no. 4, pp. 621–629, Jan. 2005, doi: 10.1016/j.ceramint.2004.08.013.

[50] I. Marinescu, W. B. Rowe, B. Dimitrov, and I. Inasaki, “Tribology Abrasives Machining Processes,” Andrew Wil., W. Andrew, Ed., New York: Elsevier, 2013, p. 699. doi: https://doi.org/10.1016/C2010-0-67070-2.

[51] H. S. Qi, W. B. Rowe, and B. Mills, “Experimental investigation of contact behaviour in grinding,” 1997.

[52] H. Hertz, “Über die Berührung fester elastischer Körper,” *Journal für die reine und angewandte Mathematik* , pp. 156–171, 1881.

[53] L. Liu, C. J. Zhou, and Z. H. Wang, “Smooth and non-smooth contact analysis of micro-surfaces of gear teeth,” in *International Gear Conference 2014: 26th–28th August 2014, Lyon*, Elsevier, 2014, pp. 360–367. doi: 10.1533/9781782421955.360.

[54] “Elastic Indentation Stress Fields,” 2007, pp. 77–100. doi: 10.1007/978-0-387-68188-7_5.

[55] N. Yoshioka and C. H. Scholz, “Elastic properties of contracting surfaces under normal and shear loads 1. Theory,” *J Geophys Res*, vol. 94, no. B12, 1989, doi: 10.1029/jb094ib12p17681.

[56] L. C. Zhang, T. Suto, H. Noguchi, and T. Waida, “Applied mechanics in grinding part II: Modelling of elastic modulus of wheels and interface forces,” *Int J Mach Tools Manuf*, vol. 33, no. 2, pp. 245–255, Apr. 1993, doi: 10.1016/0890-6955(93)90077-8.

[57] N. Macerol, L. F. P. Franca, R. Drazumeric, and P. Krajnik, “The effects of grit properties and dressing on grinding mechanics and wheel performance: Analytical assessment framework,” *Int J Mach Tools Manuf*, vol. 180, Sep. 2022, doi: 10.1016/j.ijmachtools.2022.103919.

[58] J. Palmer, D. Curtis, D. Novovic, and H. Ghadbeigi, “The Influence of Abrasive Grit Morphology on Wheel Topography and Grinding Performance,” in *Procedia CIRP*, Elsevier B.V., 2018, pp. 239–242. doi: 10.1016/j.procir.2018.09.005.

[59] X. Chen, W. B. Rowe, B. Mills, and D. R. Allanson, “Analysis and simulation of the grinding process. Part IV: Effects of wheel wear,” *Int J Mach Tools Manuf*, vol. 38, no. 1–2, pp. 41–49, 1998, doi: 10.1016/S0890-6955(97)00041-2.

[60] A. Miyahara and Y. Fujii-E, “1. Introduction - Principles of modern grinding technology,” *Nuclear Engineering and Design. Fusion*, vol. 4, no. 3, pp. 1–14, 1987, doi: 10.1016/0167-899X(87)90018-8.

[61] E. J. Duwell and W. J. McDonald, “Some factors that affect the resistance of abrasive grits to wear,” *Wear*, vol. 4, no. 5, pp. 372–383, 1961, doi: https://doi.org/10.1016/0043-1648(61)90004-7.

[62] T. Yu, A. F. Bastawros, and A. Chandra, “Experimental characterization of electroplated CBN grinding wheel wear: Topology evolution and interfacial toughness,” in *ASME 2014 International Manufacturing Science and Engineering Conference, MSEC 2014 Collocated with the JSME 2014 International Conference on Materials and Processing and the 42nd North American Manufacturing Research Conference*, Web Portal ASME (American Society of Mechanical Engineers), 2014. doi: 10.1115/MSEC2014-3961.

[63] M. J. Jackson and B. Mills, “Materials selection applied to vitrified alumina & CBN grinding wheels,” *J Mater Process Technol*, vol. 108, no. 1, pp. 114–124, Dec. 2000, doi: 10.1016/S0924-0136(00)00829-3.

[64] Shivashankara, R. Naik, and M. G. Patil, “Evaluation of vitrified bonding strength using aluminum oxide with boron nitride grinding wheel,” *Mater Today Proc*, May 2023, doi: 10.1016/j.matpr.2023.04.593.

[65] R. Cai, N. Wan, R. Mo, and Z. Chang, “Prediction of un-uniform grinding wheel wear based on instantaneous engagement of multi-axis grinding,” *International Journal of Advanced*

Manufacturing Technology, vol. 119, no. 5–6, pp. 3407–3425, Mar. 2022, doi: 10.1007/s00170-021-08133-9.

[66] H. K. Tönshoff and T. Graber, "Cylindrical and Profile Grinding with Boron Nitride Wheels," in *Proceedings of the 5th International Conference on Production Engineering, JSPE*, Tokyo: JSPE, 1984, p. 326.

[67] Y. dong Gong, X. Huang, X. long Wen, and Zhou jun, "Experimental Research on Wear Mechanism of Micro-grinding Tool in Grinding Soda-Lime Glass," 2017.

[68] X. Chen, W. B. Rowe, and R. Cai, "Precision grinding using CBN wheels," *Int J Mach Tools Manuf*, vol. 42, no. 5, pp. 585–593, Apr. 2002, doi: 10.1016/S0890-6955(01)00152-3.

[69] R. Komanduri, W. R. Reed, and B. F. von Turkovich, "A New Technique of Dressing and Conditioning Resin Bonded Superabrasive Grinding Wheels," *CIRP Annals*, vol. 29, no. 1, pp. 239–243, 1980, doi: 10.1016/S0007-8506(07)61329-8.

[70] H. Huang, "Effects of truing/dressing intensity on truing/dressing efficiency and grinding performance of vitrified diamond wheels," *J Mater Process Technol*, vol. 117, no. 1–2, pp. 9–14, Nov. 2001, doi: 10.1016/S0924-0136(01)01004-4.

[71] S. Malkin and N. H. Cook, "The Wear of Grinding Wheels: Part 2—Fracture Wear," *Journal of Engineering for Industry*, vol. 93, no. 4, pp. 1129–1133, 1971, doi: 10.1115/1.3428052.

[72] D. Herman and J. Markul, "Influence of microstructures of binder and abrasive grain on selected operational properties of ceramic grinding wheels made of alumina," *Int J Mach Tools Manuf*, vol. 44, no. 5, pp. 511–522, 2004, doi: 10.1016/j.ijmachtools.2003.10.026.

[73] M. Jackson, "A Study of Vitreous-Bonded Abrasive Materials," Liverpool John Moores University, United Kingdom, 1995.

[74] M. J. Jackson and B. Mills, "Materials selection applied to vitrified alumina & CBN grinding wheels," *J Mater Process Technol*, vol. 108, no. 1, pp. 114–124, 2000, doi: 10.1016/S0924-0136(00)00829-3.

[75] Jackson MJ, "Interfacial fracture of vitrified corundum," *Trans North Am Manuf Res Inst Soc Manuf Eng 30*, pp. 287–294, 2002.

[76] J. Sieniawski and K. Nadolny, "Experimental study on grinding wheel radial wear in surface grinding of steel CrV12 using a zonal centrifugal coolant provision system," *Proceedings of the Institution of Mechanical Engineers, Part J: Journal of Engineering Tribology*, vol. 230, no. 12, pp. 1452–1461, Dec. 2016, doi: 10.1177/1350650116637582.

[77] F. You, W. Zhou, X. Wang, and Q. Dai, "Systematic Monitoring and Evaluating the Wear of Alumina Wheel When Grinding the Workpiece of Cr12," *Complexity*, vol. 2021, 2021, doi: 10.1155/2021/6665043.

[78] M. Sazedur Rahman, T. Saleh, H. S. Lim, S. M. Son, and M. Rahman, "Development of an on-machine profile measurement system in ELID grinding for machining aspheric surface with software compensation," *Int J Mach Tools Manuf*, vol. 48, no. 7–8, pp. 887–895, Jun. 2008, doi: 10.1016/j.ijmachtools.2007.11.005.

[79] A. Arriandiaga, E. Portillo, J. Sánchez, I. Cabanes, and I. Pombo, "Virtual Sensors for On-line Wheel Wear and Part Roughness Measurement in the Grinding Process," *Sensors*, vol. 14, no. 5, pp. 8756–8778, May 2014, doi: 10.3390/s140508756.

[80] G. Yin, Y. Guan, J. Wang, Y. Zhou, and Y. Chen, "Multi-information fusion recognition model and experimental study of grinding wheel wear status," *The International Journal of Advanced Manufacturing Technology*, vol. 121, no. 5–6, pp. 3477–3498, Jul. 2022, doi: 10.1007/s00170-022-09499-0.

[81] L. M. Xu, F. Fan, Z. Zhang, X. J. Chao, and M. Niu, "Fast on-machine profile characterization for grinding wheels and error compensation of wheel dressing," *Precis Eng*, vol. 55, pp. 417–425, Jan. 2019, doi: 10.1016/j.precisioneng.2018.10.010.

[82] V. T. Thang, N. A. Tuan, and N. V. Tiep, "Evaluation of grinding wheel wear in wet profile grinding for the groove of the ball bearing's inner ring by pneumatic probes," *Journal of Mechanical Science and Technology*, vol. 32, no. 3, pp. 1297–1305, Mar. 2018, doi: 10.1007/s12206-018-0234-5.

[83] X. Liu *et al.*, "Numerical Calculation of Grinding Wheel Wear for Spiral Groove Grinding," 2021, doi: 10.21203/rs.3.rs-704822/v1.

[84] S. Yu *et al.*, "On-machine precision truing of ultrathin arc-shaped diamond wheels for grinding aspherical microstructure arrays," *Precis Eng*, vol. 73, pp. 40–50, Jan. 2022, doi: 10.1016/j.precisioneng.2021.08.014.

[85] Z. Shi and H. Attia, "High performance grinding of titanium alloys with electroplated diamond wheels," in *Procedia CIRP*, Elsevier B.V., 2020, pp. 178–181. doi: 10.1016/j.procir.2020.11.008.

[86] T. A. Saleh, "Materials: types and general classifications," in *Polymer Hybrid Materials and Nanocomposites*, Elsevier, 2021, pp. 27–58. doi: 10.1016/B978-0-12-813294-4.00008-X.

[87] D. R. Askeland and W.J. Wright., *Ciencia e ingeniería de los materiales.* , 7th ed. 2017.

[88] J. Luis. Arana, J. J. González, and Universidad del País Vasco., *Mecánica de fractura*. Universidad del País Vasco, Servicio Editorial, 2002.

[89] Serope Kalpakjian y Steven R. Schmid, *Manufactura, ingeniería y tecnología,* 5th ed. 2008.

[90] X. Sun, T. Yu, Y. Chen, C. Zhang, and Z. Ma, "Effect of cobalt on properties of vitrified bond and vitrified cubic boron nitride composites," *Ceram Int*, vol. 46, no. 4, pp. 5337–5343, 2020, doi: 10.1016/j.ceramint.2019.10.286.

[91] P. BALL, "Manufacturing Processes," in *Handbook of Polymer Composites for Engineers*, RWTH editi., Aachen Germany: Elsevier, 1994, pp. 73–98. doi: 10.1533/9781845698607.73.

[92] L. M. Camarinha-Matos, R. Rabelo, and L. Osório, *Balanced Automation*. 1997. doi: 10.1007/978-1-4471-0959-4_14.

[93] H. Talab and M. Marza, "Study Some Properties for Manufactured Grinding Wheels by Use Different Abrasive Materials," 2017. [Online]. Available: https://www.researchgate.net/publication/339570494

[94] T. Tanaka, S. Esaki, K. Nishida, T. Nakajima, and K. Ueno, "Development and Application of Porous Vitrified-Bonded Wheel with Ultra-Fine Diamond Abrasives," *Key Eng Mater*, vol. 257–258, pp. 251–256, 2004.

[95] F. Klocke, *Manufacturing Processes 2*. Berlin, Heidelberg: Springer Berlin Heidelberg, 2009. doi: 10.1007/978-3-540-92259-9.

[96] H. Li, T. Yu, L. Zhu, and W. Wang, "Analysis of loads on grinding wheel binder in grinding process: insights from discontinuum-hypothesis-based grinding simulation," *International Journal of Advanced Manufacturing Technology*, vol. 78, no. 9–12, pp. 1943–1960, 2015, doi: 10.1007/s00170-014-6767-6.

[97] C. dos Santos, I. F. Coutinho, J. E. V. Amarante, M. F. R. P. Alves, M. M. Coutinho, and C. R. Moreira da Silva, "Mechanical properties of ceramic composites based on ZrO2 co-stabilized by Y2O3–CeO2 reinforced with Al2O3 platelets for dental implants," *J Mech Behav Biomed Mater*, vol. 116, no. November 2020, 2021, doi: 10.1016/j.jmbbm.2021.104372.

[98] C. Zhang, S. Qu, W. Xi, Y. Liang, J. Zhao, and T. Yu, "Preparation of a novel vitrified bond CBN grinding wheel and study on the grinding performance," *Ceram Int*, no. January, 2022, doi: 10.1016/j.ceramint.2022.02.090.

[99] Z. Cui, Y. Huang, and H. Liu, "Predicting the mechanical properties of brittle porous materials with various porosity and pore sizes," *J Mech Behav Biomed Mater*, vol. 71, no. February, pp. 10–22, 2017, doi: 10.1016/j.jmbbm.2017.02.014.

[100] A. Karakoç and Ö. Keleş, "A predictive failure framework for brittle porous materials via machine learning and geometric matching methods," *J Mater Sci*, vol. 55, no. 11, pp. 4734–4747, 2020, doi: 10.1007/s10853-019-04339-1.

[101] M. N. Morgan, W. B. Rowe, S. C. E. Black, and D. R. Allanson, "Effective thermal properties of grinding wheels and grains," *Proc Inst Mech Eng B J Eng Manuf*, vol. 212, no. 8, pp. 661–669, 1998, doi: 10.1243/0954405981515923.

[102] Takazawa K, "Thermal aspects of the grinding operation," *Ind. Diamond Rev*, vol. 0, pp. 143–149, 1972, doi: http://ci.nii.ac.jp/naid/10003491695/ja/.

[103] Y. Kang and K. Morita, "Thermal conductivity of the CaO-Al2O3-SiO2 system," *ISIJ International*, vol. 46, no. 3, pp. 420–426, 2006, doi: 10.2355/isijinternational.46.420.

[104] N. M. Quang, P. Van Trinh, L. Thi, and P. Thanh, "Study the microstructure and mechanical properties of vitrified bond Ti-coated CBN composites for grinding process," *IOSR Journal of Mechanical and Civil Engineering (IOSR-JMCE*, vol. 17, no. 2, pp. 24–29, doi: 10.9790/1684-1702022429.

[105] P. Xia *et al.*, "Effect of Y2O3 on the properties of vitrified bond and vitrified diamond composites," *Compos B Eng*, vol. 67, pp. 515–520, 2014, doi: 10.1016/j.compositesb.2014.08.003.

[106] D. Feng, W. Wu, P. Wang, Y. Zhu, C. Zhai, and Z. Li, "Effects of Cu on properties of vitrified bond and vitrified CBN composites," *Int J Refract Metals Hard Mater*, vol. 50, pp. 269–273, May 2015, doi: 10.1016/j.ijrmhm.2015.01.002.

[107] K.-H. Lin, S.-F. Peng, and S.-T. Lin, “Sintering parameters and wear performances of vitrified bond diamond grinding wheels,” *Int J Refract Metals Hard Mater*, vol. 25, no. 1, pp. 25–31, Jan. 2007, doi: 10.1016/j.ijrmhm.2005.11.002.

[108] Z. GUO, F. HE, Z. LI, D. YAN, B. ZHANG, and J. XIE, “Effect of li2o on structure and properties of glass-ceramic bonds,” *Ceramics - Silikaty*, vol. 65, no. 2, pp. 198–205, 2021, doi: 10.13168/cs.2021.0019.

[109] M. Bahaaddini, M. Serati, H. Masoumi, and E. Rahimi, “Numerical assessment of rupture mechanisms in Brazilian test of brittle materials,” *Int J Solids Struct*, vol. 180–181, pp. 1–12, 2019, doi: 10.1016/j.ijsolstr.2019.07.004.

[110] C. Zhang *et al.*, “Determination of Tensile Strength by Modified Brazilian Disc Method for Nuclear Graphite,” *Exp Tech*, vol. 44, no. 4, pp. 475–484, 2020, doi: 10.1007/s40799-020-00363-y.

[111] M. R. Ayatollahi and A. R. Torabi, “Failure assessment of notched polycrystalline graphite under tensile-shear loading,” *Materials Science and Engineering A*, vol. 528, no. 18, pp. 5685–5695, 2011, doi: 10.1016/j.msea.2011.04.066.

[112] R. D. Sarno and M. Tomozawa, “Toughening mechanisms for a zirconia-lithium aluminosilicate glass-ceramic,” 1995.

[113] L. Ćurković *et al.*, “Flexural strength of alumina ceramics: Weibull analysis Recent Advances in Nanomaterials for Removal of New Emerging Pollutants from Water/Wastewater View project Determination of low cycle fatigue properties of sintered materials for gears View project FLEXURAL STRENGTH OF ALUMINA CERAMICS: WEIBULL ANALYSIS”, [Online]. Available: https://www.researchgate.net/publication/264713313

[114] D. Li, B. Li, Z. Han, and Q. Zhu, “Evaluation on rock tensile failure of the Brazilian discs under different loading configurations by digital image correlation,” *Applied Sciences (Switzerland)*, vol. 10, no. 16, 2020, doi: 10.3390/app10165513.

[115] Y. Belrhiti *et al.*, “Combination of Brazilian test and digital image correlation for mechanical characterization of refractory materials,” *J Eur Ceram Soc*, vol. 37, no. 5, pp. 2285–2293, 2017, doi: 10.1016/j.jeurceramsoc.2016.12.032.

[116] L. C. Zhang, T. Suto, H. Noguchi, and T. Waida, “APPLIED MECHANICS IN GRINDING PART II: MODELLING OF ELASTIC MODULUS OF WHEELS AND INTERFACE FORCES,” 1993.

[117] D. P. Saini, J. G. Wager, and R. H. Brown, “Practical Significance of Contact Deflections in Grinding,” *CIRP Annals*, vol. 31, no. 1, pp. 215–219, 1982, doi: 10.1016/S0007-8506(07)63300-9.

[118] R. L. Hecker, S. Y. Liang, X. J. Wu, P. Xia, and D. G. W. Jin, “Grinding force and power modeling based on chip thickness analysis,” *International Journal of Advanced Manufacturing Technology*, vol. 33, no. 5–6, pp. 449–459, Jun. 2007, doi: 10.1007/s00170-006-0473-y.

[119] U. S. Patnaik Durgumahanti, V. Singh, and P. Venkateswara Rao, “A New Model for Grinding Force Prediction and Analysis,” *Int J Mach Tools Manuf*, vol. 50, no. 3, pp. 231–240, Mar. 2010, doi: 10.1016/j.ijmachtools.2009.12.004.

[120] D. Wang, P. Ge, W. Bi, and J. Jiang, “Grain trajectory and grain workpiece contact analyses for modeling of grinding force and energy partition,” *International Journal of Advanced Manufacturing Technology*, vol. 70, no. 9–12, pp. 2111–2123, Feb. 2014, doi: 10.1007/s00170-013-5428-5.

[121] E. Brinksmeier *et al.*, “Advances in modeling and simulation of grinding processes,” *CIRP Ann Manuf Technol*, vol. 55, no. 2, pp. 667–696, 2006, doi: 10.1016/j.cirp.2006.10.003.

[122] D. A. Doman, A. Warkentin, and R. Bauer, “A survey of recent grinding wheel topography models,” *Int J Mach Tools Manuf*, vol. 46, no. 3–4, pp. 343–352, Mar. 2006, doi: 10.1016/j.ijmachtools.2005.05.013.

[123] X. Chen and W. B. Rowe, “ANALYSIS AND SIMULATION OF THE GRINDING PROCESS. PART I: GENERATION OF THE GRINDING WHEEL SURFACE,” Elsevier $ciene~ l.td, 1996.

[124] P. Sridhar, D. Mannherz, and K. M. de Payrebrune, “Modelling and analysis of topographic surface properties of grinding wheels,” *Journal of Manufacturing and Materials Processing*, vol. 5, no. 4, Dec. 2021, doi: 10.3390/jmmp5040121.

[125] W. Kacalak, F. Szafraniec, and D. Lipiński, “Methods for modeling the active surface of grinding wheels,” *Mechanik*, vol. 91, no. 10, pp. 907–914, Oct. 2018, doi: 10.17814/mechanik.2018.10.160.

[126] K.-H. Brakhage, M. Makowski, F. Klocke, and M. Weiss, “Grinding Wheel Modeling: Development of a mathematical Model.”

[127] X. lei Zhang, B. Yao, W. Feng, Z. huang Shen, and M. meng Wang, “Modeling of a virtual grinding wheel based on random distribution of multi-grains and simulation of machine-process interaction,” *Journal of Zhejiang University: Science A*, vol. 16, no. 11, pp. 874–884, Nov. 2015, doi: 10.1631/jzus.A1400316.

[128] D. V De Pellegrin and G. W. Stachowiak, “Assessing the role of particle shape and scale in abrasion using ‘sharpness analysis,’” *Wear*, vol. 253, no. 9–10, pp. 1016–1025, Nov. 2002, doi: 10.1016/S0043-1648(02)00232-6.

[129] J. Q. Zhang, P. Guan, C. Su, T. B. Yu, and W. S. Wang, “Simulation of Grinding Wheel with Random Three-Dimensional Abrasive and Microporous Bond,” *Key Eng Mater*, vol. 487, pp. 209–214, Jul. 2011, doi: 10.4028/www.scientific.net/KEM.487.209.

[130] Z. B. Hou and R. Komanduri, “On the mechanics of the grinding process - Part I. Stochastic nature of the grinding process,” *Int J Mach Tools Manuf*, vol. 43, no. 15, pp. 1579–1593, 2003, doi: 10.1016/S0890-6955(03)00186-X.

[131] P. Koshy, V. K. Jain~, and G. K. Lalt, “STOCHASTIC SIMULATION APPROACH TO MODELLING DIAMOND WHEEL TOPOGRAPHY,” 1997.

[132] S. Agarwal and P. V. Rao, “A probabilistic approach to predict surface roughness in ceramic grinding.”

[133] G. Warnecke and U. Zitt, “Kinematic Simulation for Analyzing and Predicting High-Performance Grinding Processes.”

[134] S. Chakrabarti and S. Paul, “Numerical modelling of surface topography in superabrasive grinding,” *International Journal of Advanced Manufacturing Technology*, vol. 39, no. 1–2, pp. 29–38, Oct. 2008, doi: 10.1007/s00170-007-1201-y.

[135] Y. Cao, J. Guan, B. Li, X. Chen, J. Yang, and C. Gan, “Modeling and simulation of grinding surface topography considering wheel vibration,” *International Journal of Advanced Manufacturing Technology*, vol. 66, no. 5–8, pp. 937–945, May 2013, doi: 10.1007/s00170-012-4378-7.

[136] Q. MENG *et al.*, “Modelling of grinding mechanics: A review,” *Chinese Journal of Aeronautics*, Oct. 2022, doi: 10.1016/j.cja.2022.10.006.

[137] J. A. Badger and A. A. Torrance, “A comparison of two models to predict grinding forces from wheel surface topography,” *Int J Mach Tools Manuf*, vol. 40, no. 8, pp. 1099–1120, Jun. 2000, doi: 10.1016/S0890-6955(99)00116-9.

[138] A. A. Torrance and J. A. Badger, “The relation between the traverse dressing of vitrified grinding wheels and their performance,” *Int J Mach Tools Manuf*, vol. 40, no. 12, pp. 1787–1811, Sep. 2000, doi: 10.1016/S0890-6955(00)00015-8.

[139] R. L. Hecker, I. M. Ramoneda, and S. Y. Liang, “Analysis of Wheel Topography and Grit Force for Grinding Process Modeling,” *J Manuf Process*, vol. 5, no. 1, pp. 13–23, Jan. 2003, doi: 10.1016/S1526-6125(03)70036-X.

[140] I. lnasaki, “Grinding Process Simulation Based on the Wheel Topography Measurement,” 1996.

[141] E. Oñate *et al.*, “A local constitutive model for the discrete element method. Application to geomaterials and concrete,” *Comput Part Mech*, vol. 2, no. 2, pp. 139–160, 2015, doi: 10.1007/s40571-015-0044-9.

[142] H. Li, T. Yu, L. Zhu, and W. Wang, “Modeling and simulation of grinding wheel by discrete element method and experimental validation,” *International Journal of Advanced Manufacturing Technology*, vol. 81, no. 9–12, pp. 1921–1938, 2015, doi: 10.1007/s00170-015-7205-0.

[143] J. L. Osa, J. A. Sánchez, N. Ortega, I. Iordanoff, and J. L. Charles, “Discrete-element modelling of the grinding contact length combining the wheel-body structure and the surface-topography models,” *Int J Mach Tools Manuf*, vol. 110, pp. 43–54, 2016, doi: 10.1016/j.ijmachtools.2016.07.004.

[144] D. André, I. Iordanoff, J. L. Charles, and J. Néauport, “Discrete element method to simulate continuous material by using the cohesive beam model,” *Comput Methods Appl Mech Eng*, vol. 213–216, pp. 113–125, 2012, doi: 10.1016/j.cma.2011.12.002.

[145] Y. Novoselov, S. Bratan, and V. Bogutsky, “Analysis of Relation between Grinding Wheel Wear and Abrasive Grains Wear,” in *Procedia Engineering*, Elsevier Ltd, 2016, pp. 809–814. doi: 10.1016/j.proeng.2016.07.116.

[146] T. W. Hwang, C. J. Evans, and S. Malkin, “High Speed Grinding of Silicon Nitride With Electroplated Diamond Wheels, Part 2: Wheel Topography and Grinding Mechanisms,” *J Manuf Sci Eng*, vol. 122, no. 1, pp. 42–50, Feb. 2000, doi: 10.1115/1.538909.

[147] L. Godino, I. Pombo, J. Girardot, J. A. Sanchez, and I. Iordanoff, “Modelling the wear evolution of a single alumina abrasive grain: Analyzing the influence of crystalline structure,” *J Mater Process Technol*, vol. 277, no. August 2019, p. 116464, 2020, doi: 10.1016/j.jmatprotec.2019.116464.

[148] D. André, J. L. Charles, I. Iordanoff, and J. Néauport, “The GranOO workbench, a new tool for developing discrete element simulations, and its application to tribological problems,” *Advances in Engineering Software*, vol. 74, pp. 40–48, 2014, doi: 10.1016/j.advengsoft.2014.04.003.

[149] I. Iordanoff, A. Battentier, J. Néauport, and J. L. Charles, “A discrete element model to investigate sub-surface damage due to surface polishing,” *Tribol Int*, vol. 41, no. 11, pp. 957–964, 2008, doi: 10.1016/j.triboint.2008.02.018.

[150] P. Koshy, V. K. Jain, and G. K. Lal, “Stochastic simulation approach to modelling diamond wheel topography,” *International Journal Machining tools Manufacturing*, vol. 37, no. 6, pp. 751–761, 1997.

[151] W. L. Cooper and A. S. Lavine, “Grinding process size effect and kinematics numerical analysis,” *ASME*, vol. 122, pp. 59–69, 2000.

[152] M. Rasim, P. Mattfeld, and F. Klocke, “Analysis of the grain shape influence on the chip formation in grinding,” *J Mater Process Technol*, vol. 226, pp. 60–68, 2015.

[153] W. B. Rowe, “Wheel Contact and Wear Effects,” *Principles of Modern Grinding Technology*, pp. 83–99, 2014, doi: 10.1016/b978-0-323-24271-4.00005-1.

[154] ASTM C 1161, “Standard Test Method for Flexural Strength of Advanced Ceramics at Ambient Temperature 1,” 2013. [Online]. Available: www.dodssp.daps.mil.

[155] Z. I. Botev, “The Normal Law Under Linear Restrictions: Simulation and Estimation via Minimax Tilting,” Mar. 2016, doi: 10.1111/rssb.12162.

[156] M. Rom, K. H. Brakhage, S. Barth, C. Wrobel, P. Mattfeld, and F. Klocke, “Mathematical modeling of ceramic bond bridges in grinding wheels,” *Math Comput Simul*, vol. 147, pp. 220–236, 2018, doi: 10.1016/j.matcom.2017.02.002.

[157] S. Malkin and N. H. Cook, “The wear of grinding wheels: Part 2-fracture wear,” *Journal of Manufacturing Science and Engineering, Transactions of the ASME*, vol. 93, no. 4, pp. 1129–1133, 1971, doi: 10.1115/1.3428052.

[158] W. B. Rowe, S. C. E. Black, B. Mills, M. N. Morgan, and H. S. Qi, "Grinding temperatures and energy partitioning," *Proceedings of the Royal Society A: Mathematical, Physical and Engineering Sciences*, vol. 453, no. 1960, pp. 1083–1104, 1997, doi: 10.1098/rspa.1997.0061.

[159] J. Webster and M. Tricard, "Innovations in abrasive products for precision grinding," *CIRP Ann Manuf Technol*, vol. 53, no. 2, pp. 597–617, 2004, doi: 10.1016/S0007-8506(07)60031-6.

[160] D. Incropera, Bergman, and Lavine, "Fundamentals of heat and mass transfer," in *Fluid Mechanics and its Applications*, 6th editio., vol. 112, Notre Dame, Indiana., 2007, pp. 355–347. doi: 10.1007/978-3-319-15793-1_19.

[161] W. B. Rowe, M. N. Morgan, and D. A. Allanson, "An Advance in the Modelling of Thermal Effects in the Grinding Process," *CIRP Ann Manuf Technol*, vol. 40, no. 1, pp. 339–342, 1991, doi: 10.1016/S0007-8506(07)62001-0.

[162] X. Zhang and J. Meng, "Recent progress of boron nitrides," in *Ultra-Wide Bandgap Semiconductor Materials*, Elsevier, 2019, pp. 347–419. doi: 10.1016/b978-0-12-815468-7.00004-4.

[163] Y. Kang and K. Morita, "Thermal conductivity of the CaO-Al2O3-SiO2 system," *ISIJ International*, vol. 46, no. 3, pp. 420–426, 2006, doi: 10.2355/isijinternational.46.420.

[164] C. Stabler, A. Reitz, P. Stein, B. Albert, R. Riedel, and E. Ionescu, "Thermal properties of SiOC glasses and glass ceramics at elevated temperatures," *Materials*, vol. 11, no. 2, pp. 1–18, 2018, doi: 10.3390/ma11020279.

[165] V. L. Wiesner and N. P. Bansal, "Mechanical and thermal properties of calcium-magnesium aluminosilicate (CMAS) glass," *J Eur Ceram Soc*, vol. 35, no. 10, pp. 2907–2914, 2015, doi: 10.1016/j.jeurceramsoc.2015.03.032.

[166] T. Rouxel, "Elastic properties and short-to medium-range order in glasses," *Journal of the American Ceramic Society*, vol. 90, no. 10, pp. 3019–3039, 2007, doi: 10.1111/j.1551-2916.2007.01945.x.

[167] K. Li, D. Wang, H. Chen, and L. Guo, "Normalized evaluation of thermal shock resistance for ceramic materials," *Journal of Advanced Ceramics*, vol. 3, no. 3, pp. 250–258, 2014, doi: 10.1007/s40145-014-0118-9.

[168] E. 23 Thecnical committees ISO/TC 17, "Bs En Iso 4957:2000 Tool Steels," in *International Standard Organization*, 2000.